

Narrowing the Gap between Theoretical and Practical Capacities in Li-Ion Layered Oxide Cathode Materials

Maxwell D. Radin, Sunny Hy, Mahsa Sina, Chengcheng Fang, Haodong Liu, Julija Vinckeviciute, Minghao Zhang, M. Stanley Whittingham, Y. Shirley Meng,* and Anton Van der Ven*

Although layered lithium oxides have become the cathode of choice for state-of-the-art Li-ion batteries, substantial gaps remain between the practical and theoretical energy densities. With the aim of supporting efforts to close this gap, this work reviews the fundamental operating mechanisms and challenges of Li intercalation in layered oxides, contrasts how these challenges play out differently for different materials (with emphasis on Ni–Co–Al (NCA) and Ni–Mn–Co (NMC) alloys), and summarizes the extensive corpus of modifications and extensions to the layered lithium oxides. Particular emphasis is given to the fundamental mechanisms behind the operation and degradation of layered intercalation electrode materials as well as novel modifications and extensions, including Na-ion and cation-disordered materials.

1. Introduction

The transition to a sustainable energy economy is contingent upon the capability to not only generate energy cleanly and efficiently, but also to store energy effectively.^[1,2] Li-ion batteries have emerged as the chief energy storage technology for applications that demand a high energy density, especially electric (and hybrid-electric) vehicles and consumer electronics.^[1,2] However, the adoption of electric and hybrid-electric vehicles is limited by the capabilities of energy storage technology: to achieve a high level of electric vehicle penetration, reductions in battery cost, weight, and volume are needed.^[1,2]

Although the development of novel materials and chemistries (such as Li/O₂,^[3,4] Li/S,^[5,6] Na-ion,^[7,8] Mg-ion,^[9] and

multi-electron Li-ion)^[10] may lead to advances in battery performance, there is significant room for improvement in state-of-the-art Li-ion batteries. The system-level usable specific energy density of Li-ion batteries used in current electric vehicles represents less than a quarter of the theoretical capacity of the electrochemically active cathode material.^[11] While part of this system-level performance gap is due to the weight of the anode and dead weight of electrochemically inactive battery components (e.g., binder, electrolyte, packaging), a significant fraction of the gap represents unused capacity in the active material. For example, the canonical

cathode material LiCoO₂ can cycle reversibly with only ≈50% of its theoretical capacity, and LiNi_{0.8}Co_{0.15}Al_{0.05}O₂ (NCA) electrodes with only ≈70%.^[12,13] This active-material performance gap is due to two factors. First, Li is unable to fully intercalate during discharge. Second, battery operation is constrained so as to avoid extracting all of the lithium from the cathode during charge. This chastity is typically implemented as a ≈4.3 V cutoff voltage during charging.^[14]

The purpose of this review is to summarize the challenges and progress in bridging the gap in theoretical and practical capacities of layered lithium oxides, especially the tradeoff between cycle life and extent of Li extraction during charge. This review starts with a discussion of the fundamental mechanisms and challenges for intercalation in layered materials, and then discusses how these play out differently for specific cathode compositions. The baseline Li_xMO₂ (M = Co, Ni, or Mn) materials here set the stage for the advanced NCA^[15,16] (Li_xNi_yCo_zAl_{1-y-z}O₂) and NMC^[17–20] (Li_xNi_yMn_zCo_{1-y-z}O₂) alloys. The last section reviews proposed strategies to address these challenges, including extensions to layered lithium oxides, such as Na-ion intercalation and cation-disordered materials.

There are many additional aspects to Li-ion battery materials not addressed in this review, but more details can be found in prior literature. Recent articles provide a birds-eye view of research on Li-ion battery materials,^[13,21–26] as well as experimental^[27,28] and computational^[29–31] methods for studying them. Both liquid^[32–34] and solid^[35–39] Li-ion electrolytes have been reviewed extensively. A number of reviews focus on specific classes of Li-ion materials, such as layered oxides,^[12,27,40] Li-excess layered oxides,^[41–43] phosphates,^[10,44] high-voltage spinel oxides,^[45,46] and Li metal anodes.^[47] For details about the

Dr. M. D. Radin, J. Vinckeviciute, Prof. A. Van der Ven
Materials Department
University of California Santa Barbara
Santa Barbara, CA 93106, USA
E-mail: avdv@engineering.ucsb.edu

Dr. S. Hy, Dr. M. Sina, C. Fang, Dr. H. D. Liu,
M. Zhang, Prof. Y. S. Meng
Department of NanoEngineering
University of California San Diego
La Jolla, CA 92093, USA
E-mail: shirleymeng@ucsd.edu

Prof. M. Stanley Whittingham
Chemistry and Materials Science and Engineering
State University of New York
Binghamton, NY 13902, USA

 The ORCID identification number(s) for the author(s) of this article can be found under <https://doi.org/10.1002/aenm.201602888>.

DOI: 10.1002/aenm.201602888

history of the development of Li-ion technology, the reader is referred to earlier works by Whittingham,^[12] Goodenough,^[48] and Thackeray et al.^[25]

2. Fundamentals

2.1. Crystallography

Many of the key mechanisms involved in the operation and degradation of layered lithium oxide battery materials involve transformations between several related layered phases (O1, O3, H1-3, etc.) and cubic phases (rocksalt and spinel). These structures all possess close-packed oxygen sublattices, but differ in the arrangement of lithium and transition-metal ions. This section discusses the relationships between various layered and cubic crystal structures to set the stage for the discussion of kinetics and degradation.

The crystal structures of layered oxides having the general formula A_xMO_2 have a close packed oxygen framework with the alkali A and the transition metal M cations filling alternating layers of interstitial sites.^[49] The layers filled by M cations form MO_2 sheets consisting of edge-sharing MO_6 octahedra. The A cations, which can be intercalated into and out of the layers between the MO_2 sheets, can occupy octahedral (O), prismatic (P), or tetrahedral (T) sites. The nature of the interstitial sites available for A cations is determined by the relative stacking of the MO_2 sheets. Prismatic sites emerge when the oxygen layers of adjacent MO_2 sheets stack directly on top of each other around the A layer. A shift in this relative stacking yields an array of octahedral and tetrahedral sites within the A layer. The octahedral sites form a 2D triangular lattice with face-sharing tetrahedral sites connecting neighboring octahedral sites.

Delmas et al. introduced a naming scheme to distinguish different layered crystal structures:^[49] a letter is used to indicate intercalant coordination (either O, P, or T) followed by a number that signifies the number of layers in the repeat unit. Here, the repeat unit refers to translational symmetries along an axis perpendicular to the MO_2 sheets. For example, in the O1 structure (Figure 1a), the oxygen layers are stacked in an AB AB pattern, forming an hcp framework with a repeat unit of a single MO_2 sheet. In "O1", the "O" indicates that the intercalants are octahedrally coordinated by anions, and the "1" indicates that the repeat unit is one MO_2 sheet. In the O3 structure (Figure 1b), the oxygen has an AB CA BC stacking, forming a rhombohedrally distorted fcc oxygen framework with three MO_2 sheets in the repeat unit. O1 and O3 are also commonly referred to by their prototype structures: CdI_2 and $\alpha\text{-NaFeO}_2$.^[50] The O3 structure has the same anion and cation framework as rocksalt and for this reason is sometimes referred to as layered rocksalt.

Many other stacking sequences besides O1 and O3 have been observed. However, there are only five "primitive" stacking sequences (i.e., stacking sequences for which each layer is symmetrically equivalent): O1, O3, P3, O2, and P2. All other stacking sequences can be decomposed into hybrids of the five primitive stacking sequences. The primitive structures can be divided into two families: the O3/O1/P3 family and the O2/P2 family. Transformations between O3, O1, and P3 are



Maxwell D. Radin received his B.S. in physics from the University of California, Irvine, and Ph.D. in physics from the University of Michigan. He is currently a postdoctoral scholar at the University of California, Santa Barbara. His research focuses on modeling from first-principles the coupling between chemistry and mechanics in Li-ion battery materials.



Y. Shirley Meng received her Ph.D. in advanced materials for micro and nanosystems from the Singapore-MIT Alliance in 2005. Shirley is currently a professor of nano-engineering at the University of California, San Diego. She is the principal investigator of a research group—Laboratory for Energy Storage and Conversion—which focuses

on functional nano and microscale materials for energy storage and conversion. She is the founding director of the Sustainable Power and Energy Center, consisting of faculty members from interdisciplinary fields, who all focus on making breakthroughs in distributed energy generation, storage and the accompanying power-management systems.



Anton Van der Ven is a professor of materials at the University of California, Santa Barbara. He obtained a Ph.D. in materials science at the Massachusetts Institute of Technology. With his research, he seeks to unravel the links between the electronic structure of solids and their macroscopic properties using first-principles statistical mechanics. He studies a wide variety of materials classes for electrochemical energy storage and high temperature aerospace applications.

easily accomplished via gliding of the MO_2 layers. This is also true between O2 and P2. However, transformations from the O3 group to the O2 group and vice versa require the breaking of metal–oxygen bonds, which is energetically more costly than gliding transformations. Therefore, cathodes typically stay within the same family during cycling.^[51]

The most important layered lithium intercalation compounds (i.e., A = Li and M = Mn, Ni, Co, Al) have crystal

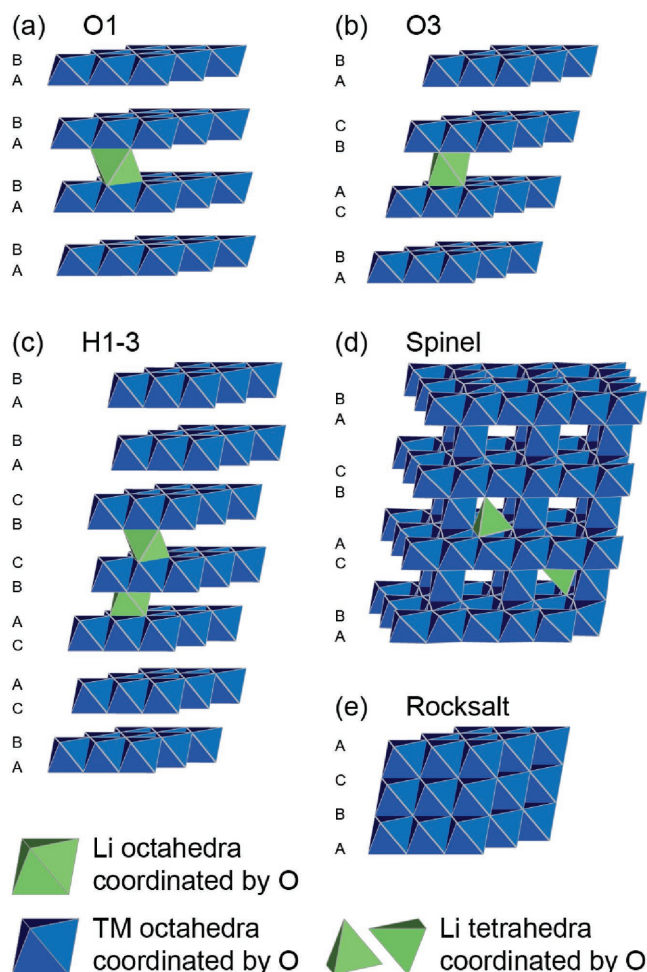


Figure 1. Crystal structures relevant for layered Li intercalation electrodes. Blue octahedra represent MO_6 units and green octahedra/tetrahedra represent Li sites.

structures that are largely limited to O3 and O1. A hybrid H1-3 phase (Figure 1c) consisting of alternating blocks of O1 and O3 environments has also been observed upon partial delithiation.^[52–54] In H1-3, Li ions preferentially occupy octahedral sites that retain O3 stacking, leaving alternating layers having O1 stacking empty. P2 and O2 structures can also be synthesized for these chemistries but are metastable.^[55,56]

Monoclinic distortions, typically denoted by the addition of a prime symbol to the structure name,^[57] occur in many layered oxides either due to collective Jahn–Teller distortions (see Section 2.2) or lithium-vacancy ordering. In chemistries that adopt the O3 structure, such distortions will often reduce the space group from $R\bar{3}m$ to $C2/m$. The lower symmetry variants are usually designated as O'3. For example, LiMnO_2 exhibits the O'3 structure because of Jahn–Teller distortions,^[58] while $\text{Li}_{0.5}\text{CoO}_2$ exhibits the O'3 structure because of a row-ordering of lithium atoms.^[52,59]

The spinel (Figure 1d) and disordered rocksalt (Figure 1e) structures are crystallographically related to the O3 structure in that they all have an fcc oxygen framework, differing only in their arrangement of A and M cations over the octahedral

and tetrahedral interstitial sites. Transformations among these phases can therefore occur readily with minimal structural changes. To transform from O3 to spinel, one quarter of the metal ions must migrate from the transition-metal layer to particular octahedral sites in the Li layer, resulting in a metal ordering within the fcc oxygen framework that has cubic symmetry. The relationship between the M ordering in O3 and that in spinel is shown in Figure 2. The Li ions must also rearrange as O3 transforms to spinel and will either occupy the remaining octahedral sites in spinel if the Li concentration is close to $x = 1$ or a subset of tetrahedral sites that do not share faces with MO_6 octahedra if the Li concentration x is less than 0.5.^[60–62] Spinel Li_xMO_2 exhibits a large two-phase coexistence region between $x = 1$ and $x = 0.5$ in which the Li-rich spinel has exclusively octahedral Li occupancy and the $x = 0.5$ spinel has exclusively tetrahedral Li occupancy. The two-phase coexistence occurs because there are only 0.5 tetrahedral sites per formula unit that are not face sharing with M ions, and adjacent octahedral and tetrahedral sites cannot be simultaneously filled by Li because they also share faces. While lithium transition metal oxides that adopt a spinel crystal structure are often referred to as $\text{Li}_y\text{M}_2\text{O}_4$, with y varying between 0 to 2, we will denote the stoichiometry of spinel compounds as Li_xMO_2 with $x = y/2$ to emphasize the similarity to layered transition metal oxides.

The rocksalt structure represents a disordering of the cations in O3 such that the Li and transition-metal layers no longer exhibit long-range periodic order, as shown in the bottom panel of Figure 2. Rocksalt phases arising from the degradation of layered oxides often are transition-metal rich, with compositions near MO. The transformation from a layered MO_2 to a rocksalt MO occurs via densification, in which oxygen is released and the transition-metal ions diffuse back into the material.

Partially deintercalated layered oxides are in general thermodynamically unstable with respect to rocksalt and spinel phases. Phase separation to the spinel $\text{Li}_{0.5}\text{MO}_2$ becomes thermodynamically favorable as soon as a small amount of Li is removed,^[63,64] as illustrated by the schematic free energy curves in Figure 3 and the pseudoternary composition space in Figure 4. Similarly, oxygen loss yielding rocksalt MO or spinel M_3O_4 generally becomes thermodynamically favorable upon deintercalation.^[65] The fact that cathode materials can maintain the layered structure during (de)intercalation owes to the kinetic limitations in the interlayer migration of transition-metal ions^[66,67] and the self-limiting nature of oxygen-evolution reactions at the surface.

When the irreversible phase changes to rocksalt and spinel are suppressed, the O3 structure often undergoes a number of reversible phase transformations that preserve the crystal structure to some degree. These reversible phase transformations can be categorized according to their influence on crystallographic symmetry and the host structure, as well as whether they are first-order or continuous transitions. Although some transformations are relatively facile, transformations involving dramatic crystallographic changes not only affect (dis)charge kinetics but also can lead to degradation of the electrode particles over the course of several charge and discharge cycles, as discussed in Sections 2.4.3 and 2.5.3.

The simplest and typically least destructive type of phase transformation leaves the host crystal structure unchanged. Layered Li_xCoO_2 , for example, exhibits a phase transformation

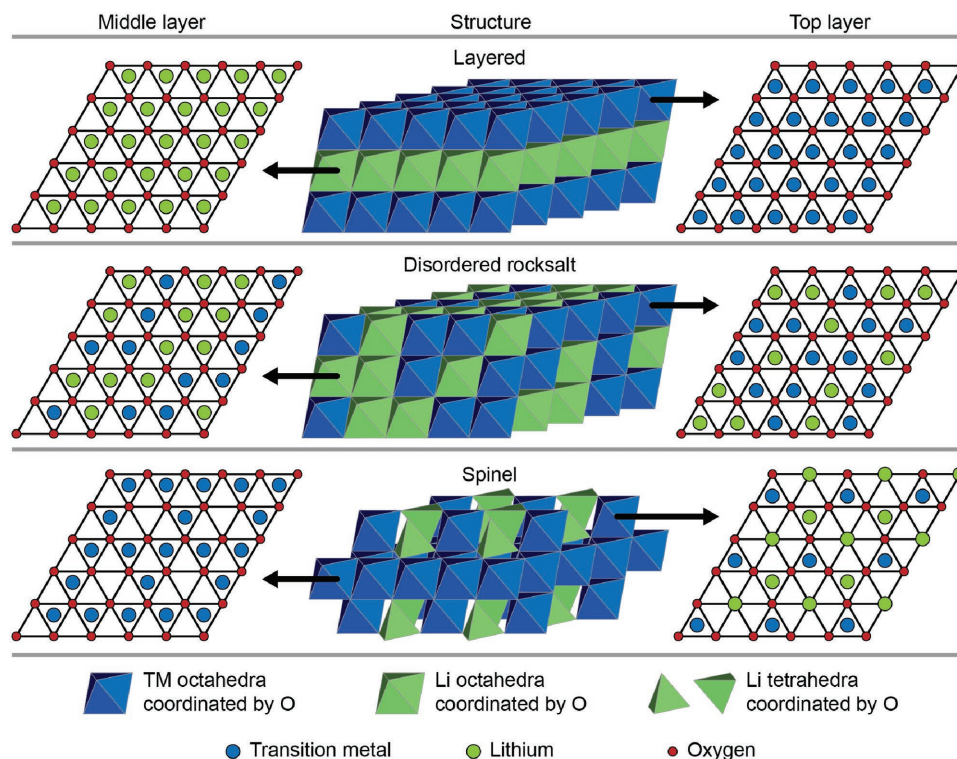


Figure 2. Relationship between the cation orderings of O3, spinel, and disordered rocksalt. Green circles and polyhedral represent Li occupancy, while blue circles and polyhedral represent transition-metal occupancy. Small red circles represent oxygen sites.

at Li-rich compositions between phases having identical symmetry, transforming from an O3 phase having composition $x = 0.95$ to another O3 phase having a composition $x = 0.75$ and slightly different lattice parameters.^[68–70] This unusual phase transition between crystallographically identical phases

is driven by the insulator-to-metal electronic transition that is triggered by the removal of Li from LiCoO_2 . Other well-known intercalation compounds that undergo phase transformations that leave the host structure unchanged include Li_xFePO_4 ^[44] and spinel $\text{Li}_x\text{Ti}_2\text{O}_4$.^[71] In both compounds, Li insertion and

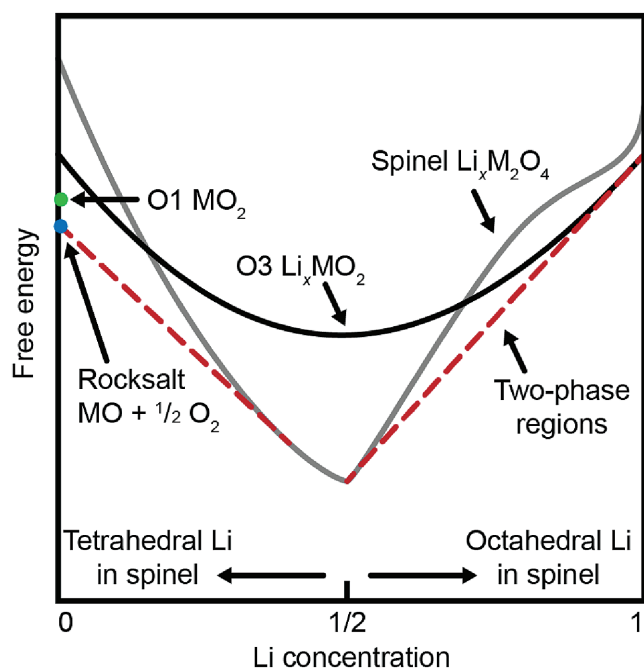


Figure 3. Schematic free energy curves for layered and spinel Li_xMO_2 .

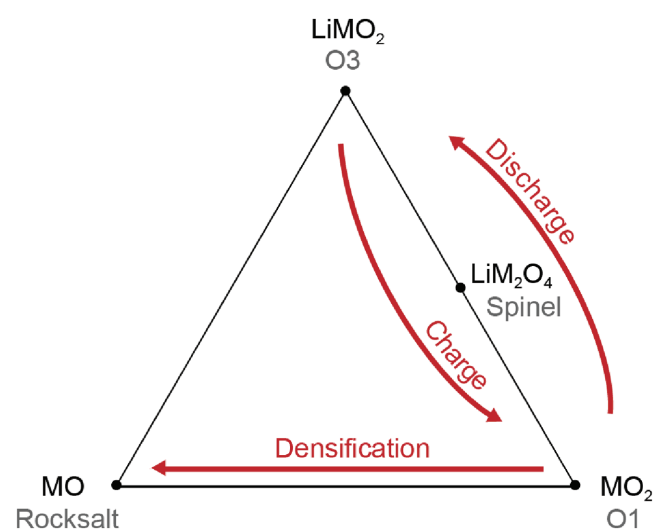


Figure 4. Beginning with fully intercalated LiMO_2 with O3 structure, the material can be fully charged to O1 MO_2 via Li deintercalation and metal cation oxidation. Ideally, the material could then be reversibly discharged back to the original LiMO_2 state. However, the process may result in atomic rearrangement to spinel LiM_2O_4 or densification to rocksalt MO.

removal causes the host to pass through a miscibility gap without altering the olivine FePO_4 and spinel Ti_2O_4 crystal structures. For Li_xFePO_4 , the miscibility gap separates FePO_4 and LiFePO_4 while for the spinel oxides, it separates LiTi_2O_4 with Li occupying tetrahedral sites and $\text{Li}_2\text{Ti}_2\text{O}_4$ with Li occupying octahedral sites.

Slightly more complex and often more destructive phase transformations occur when the host crystal structure maintains its original network, but undergoes symmetry-breaking structural distortions as the Li concentration changes. Jahn–Teller distortions and/or lithium-vacancy ordering can drive such transformations in layered Li_xMO_2 ,^[52,58,59,72,73] typically distorting the rhombohedral O3 structure to a monoclinic O'3 phase. While symmetry breaking associated with lithium-vacancy ordering usually results in a relatively minor distortion of the structure, transformations driven by collective Jahn–Teller distortions can lead to dramatic changes in lattice parameter. A notable example is the transformation of cubic LiMn_2O_4 spinel to tetragonal $\text{Li}_2\text{Mn}_2\text{O}_4$, which maintains its spinel network, but loses its cubic symmetry as a result of a cooperative Jahn–Teller distortion of the MnO_6 octahedra.^[58,74] Since the host maintains its spinel network during the transformation, it can occur coherently within the original electrode particles. However, the coexistence of tetragonally distorted $\text{Li}_2\text{Mn}_2\text{O}_4$ regions with the original cubic LiMn_2O_4 regions within the same particle will be accompanied by large coherency strains that can result in a loss of coherency along the interface and crack formation.

A more disruptive change in the host structure occurs in phase transformations between different stacking sequences (cf. Section 2.1). In layered lithium oxides, the most prevalent such stacking-sequence-change phase transformation is the transformation from the O3 to O1 host after complete Li removal. Transformations to one or more hybrid O1/O3 phases (e.g., H1-3) may also occur at intermediate compositions. The preference for O3 in lithiated phases can be rationalized by the fact that A and M sites share faces in O1, but not in O3.^[75,76] Therefore, when ions are present between the metal oxide sheets, the O1 structure is destabilized. This occurs when the compound is at least partially lithiated or when a non-negligible fraction of the transition-metal ions reside in the Li layer, as is observed in Ni-rich layered metal oxide materials.^[75] The preference for O1 upon complete delithiation has been interpreted in terms of molecular orbitals.^[77] The MO_6 octahedra contain σ bonds between the metal ion d orbitals and the oxygen p orbitals. In the O3 structure, the oxygen p orbitals from two adjacent metal oxide sheets overlap in the interlayer space, whereas the O1 structure minimizes this overlap.

Phase transformations can be further categorized as first-order or continuous. Although rigorous definitions of these terms are nuanced, in the context of batteries first-order transitions occur when (de)intercalation leads to a two-phase coexistence; this manifests as a plateau in the equilibrium voltage curve. The two phases will differ in composition, lattice parameters, and in many instances in their symmetry. The metal-insulator transition in Li_xCoO_2 between $x = 0.75$ and 0.95 is an example of a first-order phase transformation. On the other hand, continuous phase transitions represent changes in symmetry during which thermodynamic quantities vary continuously. For

example, the transition from a rhombohedral disordered state to a monoclinic row ordering in Li_xCoO_2 is thought to be a continuous phase transition. (The phase diagram of Li_xCoO_2 is discussed in more detail in Section 3.1.1.) Although the distinction between first-order and continuous transitions is of fundamental importance in condensed-matter physics, in practice continuous phase transitions in battery materials are often difficult to distinguish from first-order transitions exhibiting small two-phase regions. Nevertheless, continuous phase transitions are generally less likely to result in degradation or kinetic limitations because, unlike many first-order transitions, they do not involve large abrupt changes in the structure.

2.2. Electronic Structure

The relative energies of redox levels for different transition metals play a critical role in the thermodynamics of (de)intercalation.^[23] The positions of redox-active energy levels relative to the oxygen 2p band may also affect electron transport and oxygen evolution reactions. Although the electronic structure is in general complex, the key insight is that different transition metals have redox activity at different voltages due to a variety of effects, including crystal-field splitting and differences in electronegativity.

In all of the structures described above, including O3, O1, spinel, and rocksalt, the transition metal atoms occupy interstitial sites that are coordinated by six oxygen atoms that form a slightly distorted octahedron. The crystal field produced by octahedral oxygen anion coordination splits the five transition metal d orbitals of the transition metal (each of which can hold two electrons of opposite spin) into two sets of levels labeled e_g and t_{2g} as illustrated in Figure 5a. Orbitals in the e_g level have $d_{x^2-y^2}$ and d_{z^2} symmetries with lobes that point toward the anions, while the t_{2g} levels, which have d_{xy} , d_{xz} , and d_{yz} symmetries, have lobes that point between the oxygen atoms. The e_g levels have a higher energy than the t_{2g} levels due to the increased electrostatic repulsion from the coordinating anions. The transition-metal environment in layered compounds deviates slightly from that shown in Figure 5 because the octahedra are slightly compressed along the principal axis of the crystal. This results in a small splitting of the t_{2g} levels (not shown), which is often ignored because it does not strongly affect redox chemistry.

The commonly observed electronic configurations of d orbitals in cationic Co, Mn, and Ni species are shown in Figure 5b. (Note that while Figure 5b shows Co^{4+} as low spin, there is some evidence for high spin Co^{4+} when only a small amount of Li has been deintercalated.^[78]) When the cathode is fully charged, with composition MO_2 , the M cations have an oxidation state of +4. Upon lithiation, the transition metal ions are reduced to the +3 oxidation state as they receive electrons donated by Li. Since the Mn^{3+} and Ni^{3+} ions have a lone electron in the e_g level, they are susceptible to a Jahn–Teller distortion that lowers the overall energy of the solid by breaking the degeneracy between the two e_g orbitals. An elongation of the bonds along one of the octahedral axes splits the e_g orbitals into a lower-energy occupied orbital and a higher-energy unoccupied orbital as schematically illustrated in Figure 5c.

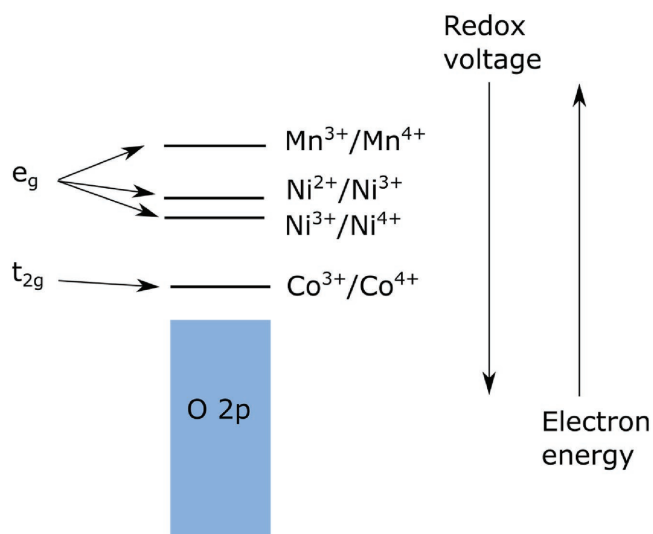
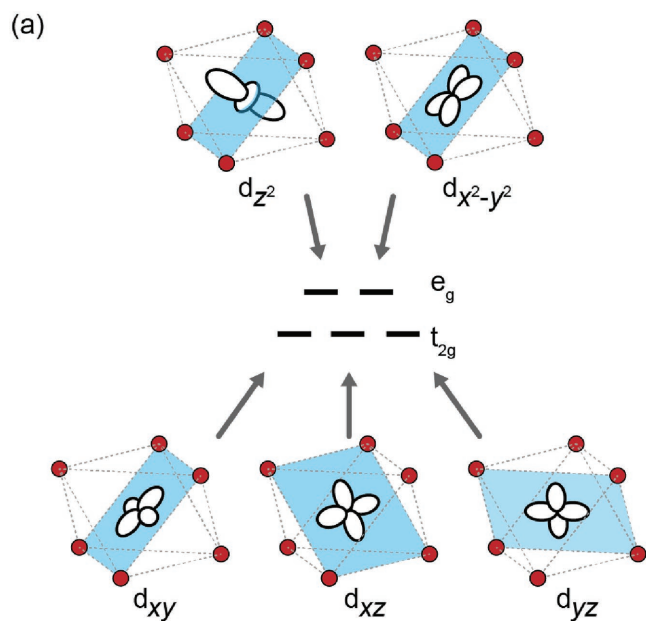


Figure 6. Qualitative positions of energy levels in layered Ni–Mn–Co oxide alloys.

(b)

	4+	3+	2+
Co			
Mn			
Ni			

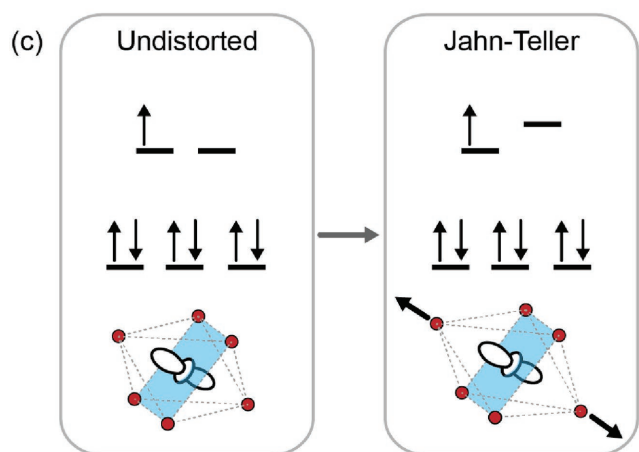


Figure 5. a) Crystal field splitting of d orbitals in an octahedral environment. b) Typical electron configurations in layered oxides. c) Splitting of e_g levels due to Jahn–Teller distortion.

Figure 6 qualitatively summarizes the positions of the redox-active energy levels for Ni, Mn, and Co, as well as the oxygen 2p band in a Ni–Mn–Co alloy.^[23,40,79] As discussed in Section 2.3,

lower energy levels correspond to higher (de)intercalation voltages. Importantly, the $\text{Co}^{3+}/\text{Co}^{4+}$ level is the lowest in energy (and therefore highest in voltage) because Co redox involves the more stable t_{2g} orbitals, while Ni and Mn redox involves the less stable e_g orbitals. The next highest energy levels above those of Co are the $\text{Ni}^{3+}/\text{Ni}^{4+}$ and $\text{Ni}^{2+}/\text{Ni}^{3+}$ couples followed by that of the $\text{Mn}^{3+}/\text{Mn}^{4+}$ redox couple.

The relative alignment of energy levels among the different transition metals has important consequences for battery thermodynamics of alloyed intercalation compounds. Typically the $\text{Co}^{3+}/\text{Co}^{4+}$ couple will oxidize at the highest voltage since it has the lowest energy.^[23,40,79] The fact that the $\text{Ni}^{2+}/\text{Ni}^{3+}$ couple is lower in energy than the $\text{Mn}^{3+}/\text{Mn}^{4+}$ indicates that Mn^{3+} will spontaneously donate electrons to Ni^{3+} , yielding Mn^{4+} and Ni^{2+} .^[23,79] Thus the deintercalation of a typical layered Ni–Mn–Co alloy having a Mn content that is lower than that of Ni initially proceeds via the oxidation of Ni^{2+} to Ni^{3+} , followed by the oxidation of Ni^{3+} to Ni^{4+} , and then finally the oxidation of Co^{3+} to Co^{4+} . The Mn^{4+} remains electrochemically inactive throughout the entire (de)intercalation process provided there is more Ni than Mn in the compound. (Although Figure 6 depicts these energy levels as discrete, in practice, the oxidation of Co begins before the oxidation of Ni ends;^[80] this results in a smooth rise in the voltage curve, rather than an abrupt step).

The energy alignment shown above is of course an oversimplification—the true electronic structure is complicated by many factors. Importantly, hybridization between the transition metal d orbitals and the oxygen p orbitals can result in the splitting of energy levels into bonding and antibonding states and the broadening of these levels into bands.^[81] For the t_{2g} levels, very little hybridization occurs because the d_{xy} , d_{xz} , and d_{yz} orbitals have little overlap with the oxygen p orbitals; the t_{2g} levels are therefore referred to as nonbonding orbitals. However, strong hybridization causes both e_g states to split into bonding and antibonding levels. The two bonding e_g levels are highly dispersive states buried deep within the oxygen p block of Figure 6 and have mostly oxygen character. In contrast,

the two antibonding e_g levels are more localized around metal ions. The states labelled e_g in Figure 5 represent these antibonding orbitals, while the bonding e_g orbitals are omitted from Figure 5 because they are not involved in redox chemistry.

Another important subtlety is that the electronic structure undergoes significant changes during (de)intercalation: the donation of electrons to the transition metal upon Li insertion leads to an increase in on-site electrostatic repulsion among electrons that shifts the d levels of the transition metal upward and away from the oxygen p levels. This results in a rehybridization between the transition metal d levels and the oxygen p levels that changes the nature of the metal–oxygen bonds as Li is added to the host. In Li_xCoO_2 , for example, the insertion of Li progressively increases the degree of ionicity of the host with increased polarization of negative charge toward the oxygen ions.^[52,81,82]

A final caveat is that the alloying of different transition metals can influence the positions of redox-active energy levels.^[40,83] One factor is ion size.^[40] For example, Mn ions are larger than Ni and Co ions because of the lower nuclear charge on Mn; as a result, Mn ions are compressed in a Ni–Mn–Co alloy, which may stabilize Mn^{4+} relative to Mn^{3+} because of its smaller size. Jahn–Teller activity could similarly affect redox potentials: Mn^{3+} may be further destabilized by Co because Co^{3+} and Co^{4+} ions will impede the distortions induced by the Jahn–Teller activity of Mn^{3+} .

In addition to differences in the positions of energy levels, transition-metal oxides also differ in the nature of the charge carriers. Depending on the degree of intercalation and choice of transition metals, layered oxides can be metallic or insulating. Li_xCoO_2 undergoes a metal–insulator transition that is coupled with a first-order structural transformation upon deintercalation: it is insulating for $x > 0.95$ and metallic for $x < 0.75$.^[68–70] Mott-type and Anderson-type transitions have been proposed as the mechanisms for this transformation.^[69,70] In contrast, Li_xNiO_2 and Ni-rich alloys appear to be insulating for $x > 0.4$.^[84–86] (Electron transport for $x < 0.4$ has not been well characterized).

The charge transport mechanisms in the insulating phases are not fully understood. Band-like conduction, small-polaron hopping, and variable-range hopping associated with Anderson localization have been suggested.^[68–70] However, even in these “insulating” layered oxides, electron transport is typically orders of magnitude faster than Li-ion transport; consequently, electron transport within individual particles generally does not limit performance. The effects of transport on performance are discussed in more detail in Section 2.4.1.

2.3. Thermodynamics

The crystal structure and chemical components of the electrode materials determines the theoretical energy density, which can be calculated from $E = \int V dQ$, where E is the energy density (gravimetric or volumetric), Q is the capacity, or charge stored per unit mass or volume, and V is the difference in electrode potential between cathode and anode. High energy densities are achieved in materials that can store a high concentration of Li at high voltages; the layered oxides perform well in this aspect when light transition metals are utilized.

The voltage difference between the cathode and anode of a battery is equal to the difference in electron electrochemical potentials of the electrodes according to

$$V = -\frac{\eta_e^{\text{cat}} - \eta_e^{\text{an}}}{e} \quad (1)$$

where η_e^{cat} and η_e^{an} are the electrochemical potentials of electrons (also referred to as Fermi levels) in the cathode and anode, and e is the elementary charge. (Note that the electrochemical potential of electrons of a particular phase is not the same when in an electrochemical cell versus isolated in vacuum or air; this is discussed in more detail below.) When a Li-ion battery is at equilibrium, this voltage difference can be expressed in terms of the difference in Li chemical potential

$$V^{\text{eq}} = -\frac{\mu_{\text{Li}}^{\text{cat}} - \mu_{\text{Li}}^{\text{an}}}{e} \quad (2)$$

Here $\mu_{\text{Li}}^{\text{cat}} = dG^{\text{cat}}/dN_{\text{Li}}^{\text{cat}}$ and $\mu_{\text{Li}}^{\text{an}} = dG^{\text{an}}/dN_{\text{Li}}^{\text{an}}$ are the chemical potentials of Li in the cathode and anode, with G being the Gibbs free energy and N_{Li} the number of Li atoms. (A derivation of the above equation, sometimes referred to as the Nernst equation, is provided in Appendix A.) The lower Li chemical potential in the cathode relative to the anode creates a driving force for Li to move from anode to cathode. As Li^+ ions move across the electrolyte, electrons perform work on the external circuit.

The equilibrium voltage V^{eq} can change significantly with state of charge, and the shape of the voltage curve provides insight about the thermodynamic behavior of the electrode material due to the relation between voltage and Li chemical potential in Equation (2). Sloping portions of the voltage curve correspond to single-phase solid solutions, while plateaus indicate two-phase regions. Figure 7a shows qualitatively the free energy per MO_2 , g , for a typical layered-oxide cathode material exhibiting three distinct hosts (O3, H1-3, and O1), as a function of Li concentration at some fixed temperature and pressure. Figure 7b shows the corresponding voltage curve of the cathode material, which is related to the negative slope of the free energy curve: $V^{\text{eq}} = -(dg/dx)/e + \text{constant}$. (The constant is determined by what reference electrode the voltage is being measured with respect to).

The lower envelope of the free energies determines phase stability at equilibrium. In the example of Figure 7, the O3 host has a two-phase region at high Li concentrations due to a first-order phase transition, which manifests as a plateau in the voltage curve. At low x , additional first-order phase transformations convert O3 to H1-3 and H1-3 to O1. Continuous phase transitions are also possible, which would manifest as inflection points in the voltage curve with no region of two-phase coexistence between the phases. Such a continuous transition is depicted at $x = 1/2$ in Figure 7. In practice, continuous transitions are often difficult to distinguish from weak first-order transitions.

It is important to realize that the voltage of a Li battery is determined by the difference in electron electrochemical potentials of the electrodes when they are placed in contact with a common electrolyte. This is not the same as the difference in

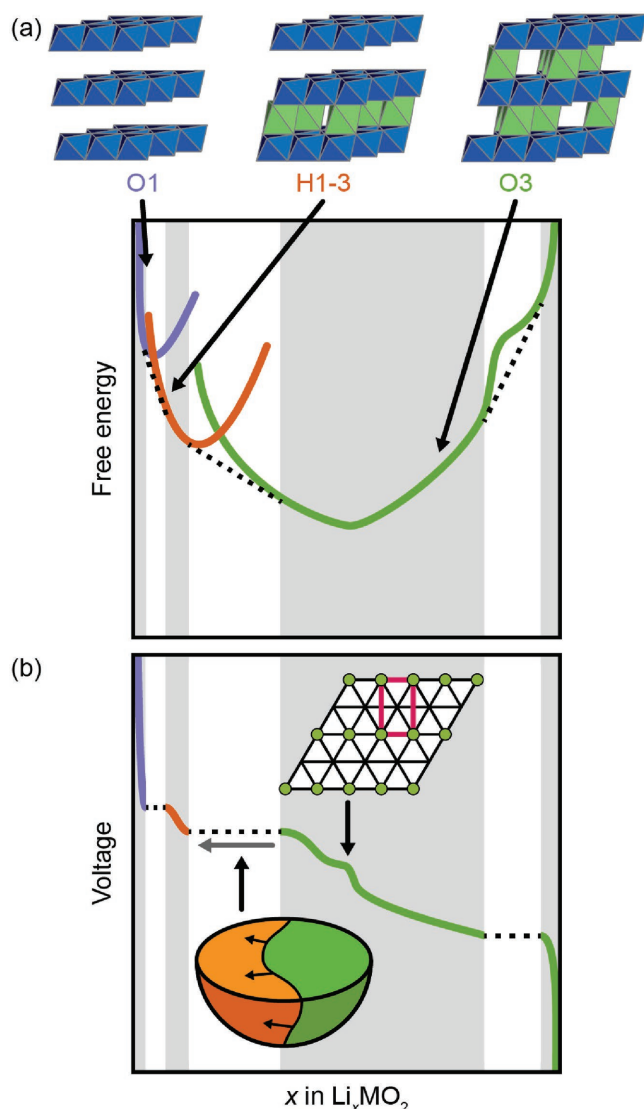


Figure 7. Relationship between Gibbs free energy and voltage for a hypothetical electrode material. a) Molar Gibbs free energy, g , versus Li concentration, x , with the dashed line representing two-phase regions determined by the common-tangent construction. b) Equilibrium voltage, V , versus Li concentration, where sloping regions correspond to single-phase equilibrium and plateaus two-phase equilibrium.

the electron electrochemical potentials of the isolated cathode and anode materials (i.e., not assembled in an electrochemical cell). The electron electrochemical potentials in the electrodes in an actual cell differs from that of the isolated materials due to the electric double layers at the electrode/electrolyte interfaces (that arise from the redistribution of Li^+ between the electrodes and electrolyte), which shift the electrostatic potential of the electrode's interior.

The effect of electric double layers on electrochemical potentials can be illustrated by considering what happens when a block of Li_xCoO_2 is submerged in an electrolyte. First, consider the change in free energy when a Li^+ ion is transferred from an isolated block of Li_xCoO_2 to the electrolyte. Let us suppose that the change in free energy is negative; this implies that

the electrochemical potential of Li^+ in the isolated Li_xCoO_2 is higher than that of the isolated electrolyte. When the Li_xCoO_2 is submerged in the electrolyte, Li^+ ions will spontaneously transfer from the Li_xCoO_2 into the electrolyte. This leads to the formation of an electric double layer: Li^+ ions accumulate in the electrolyte near the interface, balanced by the electrons left behind in the $\text{Co } t_{2g}$ states. The transfer of Li^+ ions from the Li_xCoO_2 to the electrolyte will stop when the electrostatic potential drop due to the double layer becomes large enough so that additional Li^+ transfer does not result in a net free energy change; this represents equilibrium, in which the electrochemical potential of Li^+ is equal in the electrolyte and Li_xCoO_2 . (Had the electrochemical potential of Li^+ been lower in Li_xCoO_2 than in the electrolyte, then Li^+ ions would transfer from the electrolyte to the Li_xCoO_2 , and the double layer would consist of excess Li^+ ions accumulating in Li_xCoO_2 balanced by salt anions left behind in the electrolyte.) The electrostatic potential drop resulting from the electric double layer shifts the electrochemical potential of electrons in the Li_xCoO_2 , and so the absolute position of the Fermi level changes when the Li_xCoO_2 is submerged in the electrolyte. The Nernst equation for Li-ion batteries (Equation (2)) expresses what the difference in Fermi level will be between two materials after they have equilibrated with the same electrolyte.

Although electric double layers shift the electrochemical potentials of materials when they are assembled into a cell, the relative positions of the energy levels and relative stabilities of Li^+ sites in different materials (when isolated) can, nevertheless, provide qualitative insight into their relative equilibrium voltages. To illustrate this, it is convenient to consider the intercalation of a Li atom as the combination of inserting a Li^+ ion and injecting an electron. This corresponds to splitting the chemical potential into a sum of a Li^+ chemical potential and an electron chemical potential according to $\mu_{\text{Li}} = \eta_{\text{Li}^+} + \eta_e = \mu_{\text{Li}^+} + \mu_e$ (see Appendix A). In this form, trends in the average voltage as a function of transition metal chemistry and crystal structure can be easily explained. For example, because Li^+ cations in LiNiO_2 and LiCoO_2 have similar chemical and electrostatic environments (octahedrally coordinated by oxygen), we can expect that $\mu_{\text{Li}^+}(\text{LiCoO}_2) \approx \mu_{\text{Li}^+}(\text{LiNiO}_2)$. In other words, it takes the same amount of free energy to insert a Li^+ ion into LiCoO_2 as LiNiO_2 when they are at the same electrostatic potential. In contrast, the highest unoccupied orbitals of LiCoO_2 , which determine μ_e , are significantly lower in energy than those of LiNiO_2 due to the crystal field splitting of the transition-metal sites (see Section 2.2); therefore $\mu_e(\text{LiCoO}_2) < \mu_e(\text{LiNiO}_2)$ (i.e., it is easier to inject an electron into LiCoO_2 than LiNiO_2 when they are at the same electrostatic potential). Combining these equalities shows that $\mu_{\text{Li}}(\text{LiCoO}_2) < \mu_{\text{Li}}(\text{LiNiO}_2)$, thereby explaining why LiCoO_2 has a higher intercalation voltage than LiNiO_2 . A similar analysis for the spinel oxides shows that the greater stability of the tetrahedral sites compared to octahedral sites, $\mu_{\text{Li}^+}(\text{tet}) < \mu_{\text{Li}^+}(\text{oct})$, can explain why the tetrahedral sites have a higher intercalation voltage despite operating on the same redox couple as the octahedral sites.^[23,60]

Thermodynamic considerations also provide some insight into the stability window of the electrolyte. If the voltage of the cathode is too high, the electrolyte will be oxidized, while if the voltage of the anode is too low, the electrolyte will be reduced.

The maximum practical voltage difference between anode and cathode is therefore limited by the electrochemical stability window of the electrolyte. Prior to the development of Li-ion batteries, most commercial electrochemical energy storage devices employed aqueous electrolytes, which are limited by the ≈ 1.3 V stability window of water. Nonaqueous electrolytes have enabled Li-ion batteries to operate above 4 V because of their wider stability windows.

In practice, many electrochemical cells (both aqueous and nonaqueous) can safely operate slightly beyond the stability window of the electrolyte if the oxidation/reduction of the electrolyte is self-limiting. This requires that the decomposition products be electronically insulating so that further decomposition does not occur, but ionically conducting so that Li^+ ions can pass through. Such passivating layers, referred to as solid-electrolyte interphases (SEIs), are crucial to the functioning of Li-ion anodes, which typically operate below the reduction potential of the electrolyte.^[32–34,87]

In the absence of a protective SEI, the limits of stability are determined by the kinetics of electrolyte oxidation/reduction and the details of the electrode/electrolyte interface. Although the kinetics of these reactions are quite complex,^[31] the gap between the highest occupied molecular orbital (HOMO) and lowest unoccupied molecular orbital (LUMO) of the electrolyte provides an upper bound on the size of the stability window. (In the case of solid electrolytes, the band gap similarly puts an upper bound on the stability window.) Note that the absolute positions of the HOMO and LUMO in the isolated electrolyte are not the same as those of an electrolyte in contact with an electrode because of the double layer at the electrode/electrolyte interface; therefore the HOMO/LUMO positions of the isolated electrolyte strictly speaking do not inform us about the position of the stability window, only its width. Furthermore, chemical decomposition reactions between species of the electrolyte and the electrode may occur at voltages that are well within the window bounded by the HOMO and LUMO of the electrolyte.^[88]

Lastly, we mention that the electric double layer has several relevant effects aside from the shifting of Li^+ and electron electrochemical potentials. Importantly, because the amount of charge separated across the interface changes with the applied voltage, the double layer contributes some capacity during cycling. For batteries, this double-layer capacitance is generally quite small compared to the capacity arising from the redox

activity of the electrode. However, some devices exploit this double-layer capacitance for energy storage, and are referred to as electric double-layer capacitors (EDLCs).^[89] The boundary between battery and EDLC can become fuzzy when particle sizes are very small: in the absence of solid-state diffusion limitations, intercalation electrodes exhibit electrochemical performance similar to a traditional capacitor. Devices operating in this regime have attracted attention for applications that require high rate capability, and are often referred to as “intercalation pseudocapacitors.”^[89,90]

2.4. Kinetics

Dissipation is present in all kinetic processes and is a direct result of the second law of thermodynamics, which stipulates that spontaneous processes can only occur as a result of an overpotential of some sort. Heat flow, for example, will occur only if there is a spatial variation in temperature while a piston will spontaneously move only if there is a pressure difference across it. Each of the various kinetic processes that occur during charge and discharge of an electrode material are similarly driven by a gradient or a spatial discontinuity in a free energy or a chemical potential.

The dissipation of free energy by kinetic processes controls important aspects of battery performance, such as rate capability, polarization, and usable capacity. Key kinetic processes that dominate during the charge and discharge of layered lithium oxides are illustrated in **Figure 8**. These include: lithium and electron transport, interfacial ion transfer, and phase transformations. This section describes the underlying mechanisms behind these kinetic processes and how they manifest in electrochemical behavior.

2.4.1. Transport

Theory: An important source of dissipation is the diffusion of cations between the surface of the electrode and the interior. Since, as described in Section 2.2, electrons are substantially more mobile than Li in layered transition metal oxides, they are not rate limiting and the transport of Li within the electrode is governed by equations of diffusion as in a typical metallic

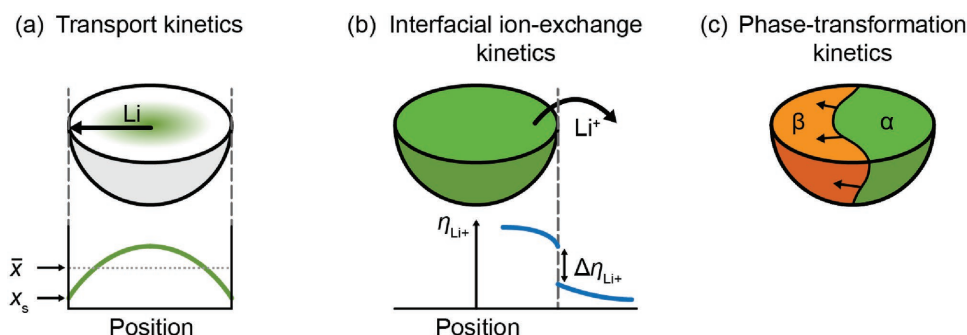


Figure 8. Transport and kinetic limitations in Li-ion cathode materials. a) Transport kinetics, which results in the surface Li concentration x_s differing from the average concentration \bar{x} . b) Interfacial ion-exchange kinetics, which results in a drop in Li^+ electrochemical potential η_{Li^+} across the electrode/electrolyte interface. c) Phase-transformation kinetics, represented here by the hypothetical transformation of a phase β into phase α .

phase. Li diffusion in layered intercalation compounds occurs by exchanges with vacancies and is primarily restricted to the 2D Li-intercalation layers between MO_2 sheets. The starting point for a description of diffusion within a crystalline host is an expression that relates the Li flux to a gradient in the Li chemical potential^[91,92]

$$J_{\text{Li}} = -L\nabla\mu_{\text{Li}} \quad (3)$$

where J_{Li} is the flux of the Li atoms, L is a kinetic Onsager transport coefficient and $\nabla\mu_{\text{Li}}$ is the gradient in chemical potential of Li. By application of the chain rule of differentiation, this equation can be converted to Fick's first law

$$J_{\text{Li}} = -D\nabla c_{\text{Li}} \quad (4)$$

which relates the flux to the chemical diffusion coefficient, D , and the gradient of the local Li concentration, c_{Li} . The concentration, c_{Li} , is defined as the number of Li ions per unit volume, which for layered intercalation compounds can be expressed as the fraction of filled octahedral Li sites, x , divided by Ω , the volume of the crystal per Li_xMO_2 formula unit. It is instructive to write the chemical diffusion coefficient as the product of a jump-diffusion coefficient, D_j , and the thermodynamic factor, Θ .^[93] The jump-diffusion coefficient is defined as

$$D_j = \frac{kT}{x} \Omega L \quad (5)$$

where k is the Boltzmann constant and T is temperature. The thermodynamic factor is a function of the chemical potential according to

$$\Theta = \frac{x}{kT} \frac{\partial\mu}{\partial x} \quad (6)$$

The thermodynamic factor of a thermodynamically ideal intercalation compound (in the sense that interactions among Li ions can be neglected) reduces to $\Theta = 1/(1-x)$. Any deviation from this behavior is an indication that there is some degree of interaction among the Li^+ ions. In addition to thermodynamic ideality, it is also useful to consider the limit of kinetic ideality, defined as compounds in which Li hops into adjacent vacant sites occur with a constant hop frequency, Γ , independent of the Li concentration and the local degree of Li-vacancy order or disorder.^[91] The jump diffusion coefficient, D_j , in an intercalation compound that is both thermodynamically and kinetically ideal takes an especially simple form and scales linearly with the vacancy concentration, i.e., $D_j \propto (1-x)$.^[94] The product of the thermodynamic factor, Θ , with the kinetic factor, D_j , in an ideal intercalation compound, therefore, yields a constant chemical diffusion coefficient, D , independent of Li concentration.

Most intercalation compounds rarely exhibit ideal thermodynamic and kinetic behavior: the chemical diffusion coefficient usually exhibits a strong concentration dependence. While the thermodynamic factor, Θ , approaches unity in the dilute limit of $x \approx 0$ where Li-Li interactions become negligible, it deviates rapidly from the $x/(1-x)$ composition dependence upon

insertion of Li.^[95-98] Thermodynamic factors often take values of 10 or greater in solid solutions at intermediate Li concentrations ($x \approx 0.5$).^[62,98,99] This deviation is a manifestation of interactions among Li ions that result in some degree of short-range order even within the solid solution. At stoichiometric compositions where Li-vacancy ordering occurs, the deviation from thermodynamic ideality is even more pronounced, with Θ exhibiting spikes that can be several orders of magnitude larger than unity.^[97,100] This is also true as x approaches 1, where even the ideal thermodynamic factor that scales with $x/(1-x)$ diverges.

The kinetic factor, D_j , will usually also deviate from the $(1-x)$ concentration dependence of a kinetically ideal compound. If vacancy clusters mediate Li diffusion, the kinetic factor becomes proportional to the vacancy cluster concentration instead of the concentration of individual vacancies, which is equal to $1-x$. The kinetic factor also depends exponentially on the activation barriers for diffusion. Any concentration dependence of the average activation barrier for Li hops will be amplified in D_j as a result of this exponential dependence.^[91]

Transport behavior of lithium transition-metal oxides: Although layered intercalation compounds exhibit highly nonideal transport kinetics, there are many common patterns in the diffusion phenomena in different layered materials. **Figure 9** shows the variation of the Li diffusion coefficient with state of charge in Li_xCoO_2 ,^[101] which captures many of the effects seen in different layered compounds. The shape of this curve can in large part be traced to the Li hop mechanism at the atomic scale.^[91,96-98]

Li hops between neighboring octahedral sites in a layered intercalation compound follow a curved trajectory through an adjacent tetrahedral site as illustrated in **Figure 10**.^[96,98] This path maximizes the distance between the migrating Li and the coordinating oxygen ions along the hop trajectory. A consequence of this hop trajectory is that the migration barrier becomes very sensitive to the local Li-vacancy ordering surrounding the hopping Li ion. First-principles calculations based on density functional theory (DFT) have shown that the migration barrier is substantially lower if the intermediate tetrahedral

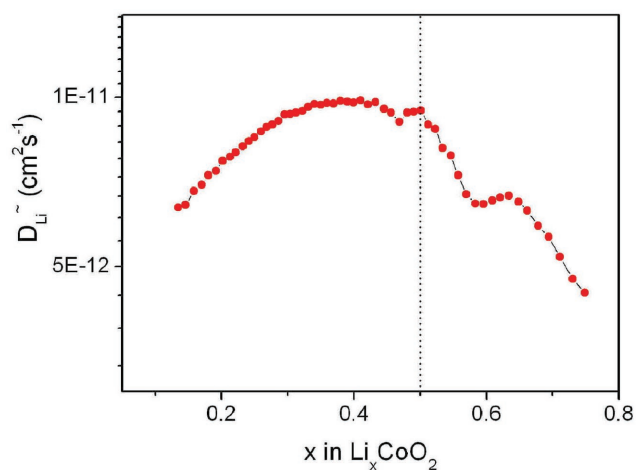


Figure 9. Experimentally measured variation of chemical diffusion coefficient with state of charge in Li_xCoO_2 .^[101]

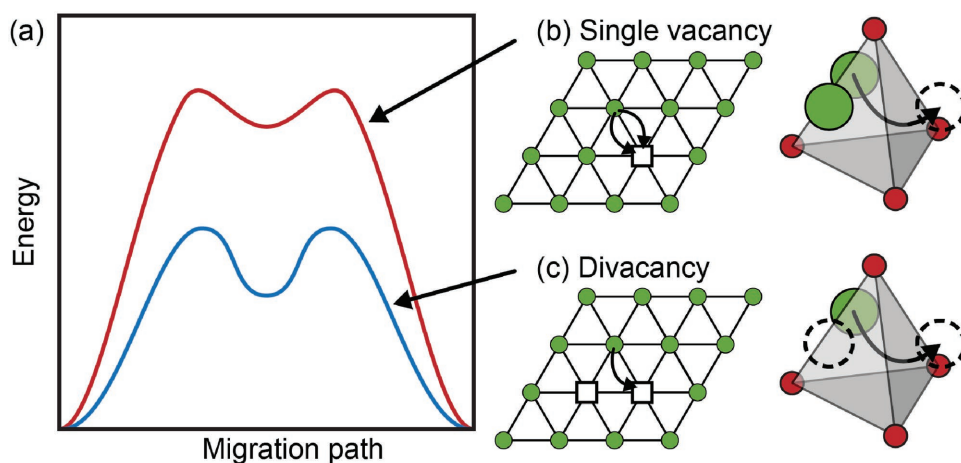


Figure 10. Monovacancy and divacancy Li migration mechanisms. Each tetrahedral site is face-sharing with three octahedral Li sites. In both mechanisms, the lithium atom moves between two of these octahedral sites by passing through the tetrahedral site. The two mechanisms differ in whether the third Li site is occupied or not.

site is surrounded by two vacant octahedral sites as opposed to only one vacant site as illustrated in Figure 10.^[96,98] A Li^+ ion hopping into an isolated vacancy must pass through a tetrahedral site that shares a face with an occupied octahedral site. This results in a strong electrostatic repulsion that is absent if the Li hops into a divacancy.

Kinetic Monte Carlo simulations have shown that the strong dependence of the migration barrier on local Li coordination results in divacancy hops being the dominant Li diffusion mechanism throughout most of the composition range.^[91,95,97,98] One consequence of the divacancy mechanism is that the chemical diffusion coefficient falls dramatically as x approaches 1, as can be seen for Li_xCoO_2 in Figure 9. This nonideal behavior arises because the concentration of divacancies decreases rapidly as the material approaches full intercalation, altering the concentration dependence of the jump diffusion coefficient, D_j . To first order the jump diffusion coefficient D_j for the divacancy mechanism is proportional to the square of the vacancy concentration, $(1 - x)^2$, as opposed to simply the vacancy concentration, $1 - x$, as in a kinetically ideal solid.

The Li diffusion coefficient of layered intercalation compounds also decreases rapidly as x approaches zero,^[95,96,98] as can be seen in Figure 9, due to increases in the migration barrier. The rise in migration barrier can be largely attributed to the collapse of interlayer spacing between MO_2 slabs.^[96,98] The decrease in the interlayer spacing penalizes the intermediate tetrahedral site more than the octahedral end-states, causing an increase in Li migration barriers. Additionally, as the Li concentration progressively decreases, the average oxidation state of the transition metal increases from +3 to +4; the greater degree of electrostatic repulsion destabilizes the tetrahedral sites because they share faces with the transition-metal sites.^[96,102]

The combined effect of a divacancy diffusion mechanism and a progressive increase in the migration barrier at low Li concentrations (due to a c -lattice parameter contraction and an increase in the average transition metal oxidation state) is to endow the chemical diffusion coefficient with a concentration dependence that exhibits a maximum at intermediate concentrations, as can be seen for Li_xCoO_2 in Figure 9. There

is likely little that can be done to alter the divacancy diffusion mechanism in layered intercalation compounds (responsible for the drop-off in the chemical diffusion coefficient at high Li concentrations) without a dramatic change in the local crystal structure. Strategies that minimize a contraction of the c -lattice parameter at low Li concentrations, however, could ameliorate the reduction in Li mobility as Li is extracted. A mixture of transition metals (e.g., Co, Ni and Mn) having different oxidation states (or differing degrees of hybridization with oxygen) may also offer strategies for enhancing diffusion. As long as the transition metals that least repulse Li ions form a percolating network, long-range diffusion can occur through tetrahedral sites that experience a minimal electrostatic repulsion.^[102,103]

Transport properties have been measured experimentally for the layered oxides, including Li_xCoO_2 ,^[100,101] Li_xNiO_2 ,^[104–106] NCA,^[86] and NMC;^[107,108] however, reported values often differ by orders of magnitude, and the dependence of diffusion coefficient on state of charge also varies widely between experiments. One challenge in the measurement of transport properties is isolating the diffusional relaxation of the electrode material from other kinetic processes, such as the diffusion of Li^+ ions in the electrolyte.^[86,101,107,108] This can be further complicated by the penetration of the electrolyte into the active material through microcracks formed at high states of charge.^[107] Assumptions about the diffusion length and particle geometry can also influence transport measurements.^[100] Additionally, the variation in the N_{Li} defect concentration in different samples may result in differences between experimental results: the contraction of the interlayer spacing induced by these defects has been hypothesized to hinder Li diffusion.^[102,103]

Because spinel and rocksalt phases often form as thin layers on the surface of layered intercalation compounds (see Section 2.5.1), the mechanisms and rates of Li diffusion through these structures also play a crucial role in determining the overall rate capability of layered intercalation compounds. Li diffusion mechanisms in spinel Li_xMO_2 are very sensitive to the overall Li concentration. Below $x = 0.5$, the Li ions occupy tetrahedral sites that form a diamond network. Hops between neighboring tetrahedral sites pass through intermediate

octahedral sites.^[62,109] Diffusion mechanisms involving vacancy clusters (e.g., divacancies as in the layered compound) are crystallographically not possible when Li hops between adjacent tetrahedral sites of spinel since the intermediate states centered at octahedral sites are exclusively coordinated by the endpoints of the hop.^[91] This results in very simple and relatively uncorrelated diffusion mechanisms^[62] in spinels below $x = 0.5$. In fact, the rate capabilities of spinel Li_xMO_2 compounds between $x = 0$ and 0.5 are generally quite high and depend most sensitively on the composition dependence of the migration barriers.^[62] Diffusion in spinel Li_xMO_2 becomes substantially more complex above $x = 0.5$. Between $x = 0.5$ and 1, spinel Li_xMO_2 forms a two-phase coexistence between $\text{Li}_{0.5}\text{MO}_2$ with Li occupying exclusively tetrahedral sites and LiMO_2 with Li occupying predominantly octahedral sites. Li diffusion within spinel LiMO_2 arises from hops between neighboring octahedral sites that pass through an intermediate tetrahedral site. As with the layered compounds, the passage through an intermediate tetrahedral site when hopping between neighboring octahedral sites makes the compound susceptible to vacancy cluster mechanisms, which can result in highly correlated diffusion.^[62,99]

Diffusion in disordered rocksalts is generally sluggish. This has been attributed to the smaller size of the tetrahedral sites, which represent intermediate states for Li hops between octahedral sites.^[110] Furthermore, the rocksalt phases observed to form on the surface of layered intercalation compounds tend to be metal rich (i.e., a transition metal to oxygen ratio greater than $\frac{1}{2}$). This further limits Li transport by reducing the connectivity of the Li sites. Li-excess disordered rocksalts, however, exhibit relatively facile Li transport.^[110] The use of such Li-excess rocksalts as cathodes is discussed in Section 4.7.

In addition to the Li mobility in the bulk, microstructure may also strongly affect transport. For example, grain boundary diffusion could significantly influence Li-ion transport:^[111] facile Li diffusion along grain boundaries would enhance transport, while slow Li diffusion across grain boundaries would impede it. Microcracks (as discussed in Section 2.5.3) that allow the electrolyte to penetrate deeper into the active material particles could also improve access to Li.^[107] Similarly pipe diffusion (Li motion along dislocations) could potentially influence transport behavior.

Impact on electrochemical performance: The gradients in chemical potential that are required to drive diffusion cause polarization in the voltage curve during charge and discharge. Under galvanostatic (fixed current) conditions, this can result in a shift of the average voltage as well as a reduction in cathode utilization. **Figure 11** illustrates diffusion limitations in an electrode particle during charge and discharge. The local depletion of Li at the surface relative to the Li concentration in the interior of the electrode particle leads to the emergence of a Li concentration gradient. Figure 11a illustrates how these concentration gradients will manifest as polarization and losses in capacity when (dis)charge starts from a fully (de)lithiated particle. Cycling in a real battery is more complex because the incomplete cathode utilization on charge means that discharge does not start from a fully delithiated state. Similarly, charge cycles (except for the initial charging) will not start from a completely lithiated state. Figure 11b therefore illustrates how Li transport might influence the voltage curve for galvanostatic cycling.

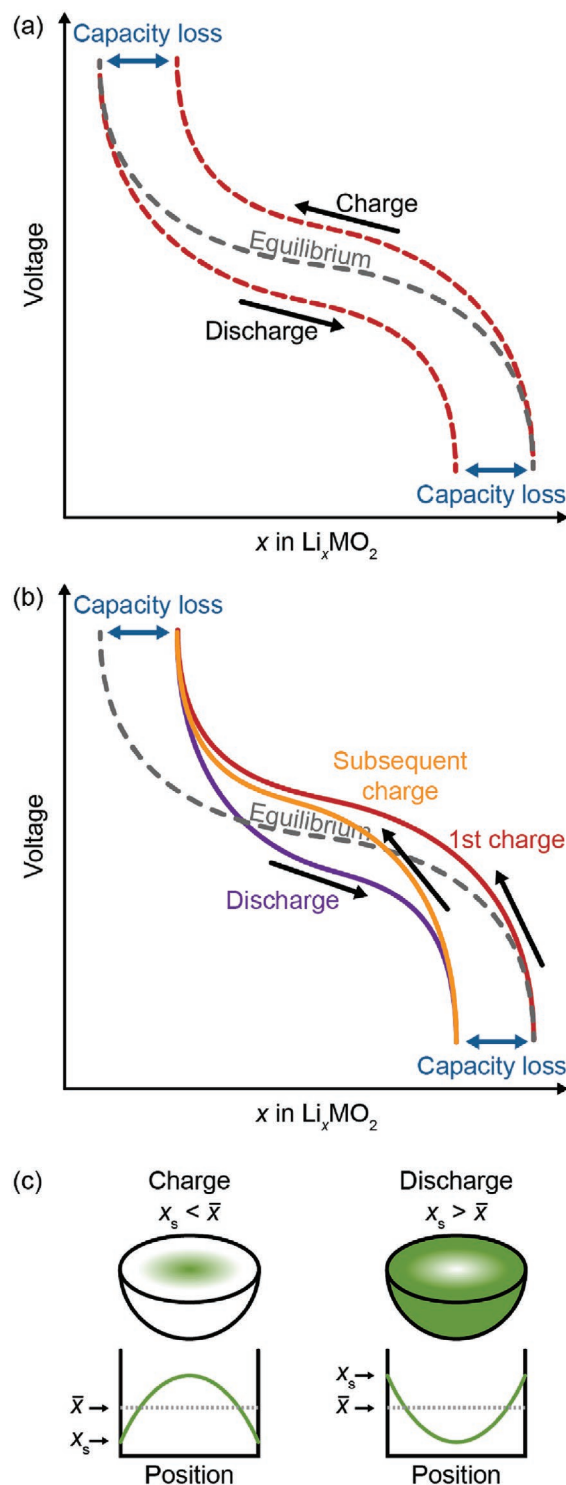


Figure 11. Qualitative effect of diffusion limitations on galvanostatic (dis)charge curves. a) Hypothetical (dis)charge curves when starting from the fully (de)lithiated state. b) Hypothetical voltage curves for cycling starting from a fully lithiated material. c) Concentration profile of Li within a particle during charge and discharge.

The deviation of the experimentally observed voltage curve from the equilibrium voltage curve originates from the fact that the measured voltage is determined by the Li concentration at

the electrode/electrolyte interface x_s , not the average Li concentration in the particle \bar{x} . (See Appendix A for details.) As is clear from Figure 11c, during charging the Li concentration at the electrode surface is lower than the average Li concentration within the electrode. Because the equilibrium voltage increases with decreasing concentration, the voltage at the surface concentration is higher than that at the average Li concentration: $V^{\text{eq}}(x_s) > V^{\text{eq}}(\bar{x})$. The electrochemist measuring the voltage curve does not plot the measured voltage as a function of the surface concentration x_s , a quantity that is very difficult if not impossible to measure, but rather as a function of the average concentration, \bar{x} , which can easily be estimated by integrating the current of electrons extracted from the electrode. The measured voltage upon charging an electrode is therefore always higher than the true equilibrium voltage curve. The reverse occurs during discharge.

In addition to polarization in the voltage, the presence of Li concentration gradients prevents a realization of the full theoretical capacity during galvanostatic cycling because discharge/charge stops when the surface becomes fully intercalated/deintercalated. (Or more specifically, when the Li content on the surface reaches the value corresponding to the cutoff voltage.) The utilization will decrease with increasing rate because the difference between the surface concentration and the average concentration gets larger as the rate increases. Importantly, this loss of utilization cannot be overcome by making the voltage cutoffs more extreme: a substantial fraction of the electrode's theoretical capacity will still remain unused.

The effects of limited Li diffusion on polarization and capacity can be illustrated with a simple model of an electrode that is both thermodynamically and kinetically ideal. Such an electrode exhibits an ideal-solution equilibrium voltage and has a constant diffusion coefficient, independent of the Li concentration. The voltage is determined by the surface concentration, and is plotted in **Figure 12** for a cylindrical geometry with constant current boundary conditions. The surface concentration was found by numerical solution of the diffusion equation (Equation (4)), as described in Appendix B.

As can be seen from Figure 12, this simple model illustrates the strong dependence of the discharge voltage curve

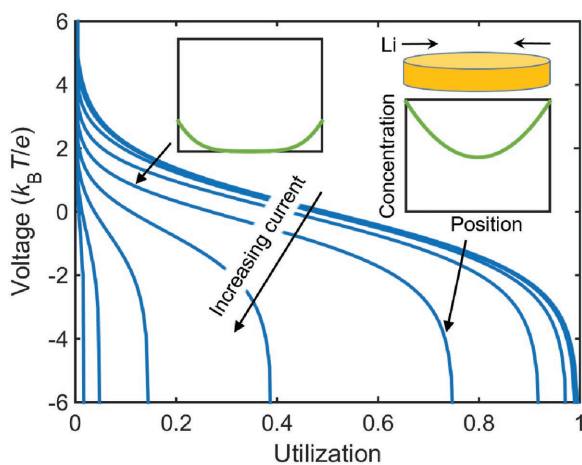


Figure 12. Simulated galvanostatic discharge curves for ideal diffusion in a cylindrical particle at different rates.

on discharge rate. At low currents, where concentration gradients are small, the discharge curve approaches the equilibrium voltage curve. As the discharge current increases, internal Li concentration gradients must become larger to produce the larger Li fluxes and as a consequence, the overall voltage and electrode utilization decreases. The simple model clearly shows that transport limitations can manifest as an apparent loss in capacity. The reason for this incomplete utilization is that discharge ends when the surface becomes fully lithiated, which, due to internal Li concentration gradients occurs well before the interior of the electrode particles are fully lithiated. This is illustrated in the insets in Figure 12, which show the distribution of Li within the particle during discharge. As the surface approaches full lithiation ($x_s \rightarrow 1$), the voltage diverges to very low values due to the entropic costs of adding Li to a solution that contains very few vacancies.

While the above discussion has focused on transport within the electrode material, the transport of Li^+ ions within the electrolyte can similarly result in electrode polarization and incomplete electrode utilization.^[112] Although Li^+ ions generally are much more mobile in the electrolyte than in the electrode material, the distances over which diffusion occurs are orders of magnitude larger in the electrolyte ($\approx 100 \mu\text{m}$) than in the electrode particles ($\approx 100 \text{nm}$).

2.4.2. Interfacial Ion-Transfer Kinetics

Interfacial ion transfer at the electrode/electrolyte interface is a complex process that can result in kinetic limitations. This process involves Li^+ desolvation and insertion into the cathode material. Kinetic limitations associated with the diffusion of Li^+ ions through any surface film and any rocksalt- or spinel-like regions near the cathode surface (see Section 2.5) may also be interpreted as part of the ion-transfer process. Impedances associated with these surface processes are sometimes referred to as “charge-transfer resistance.”

Under open-circuit conditions, the exchange of Li^+ between the electrode and electrolyte resides in dynamic equilibrium, expressed by the reaction $\text{Li}(\text{electrode}) \leftrightarrow \text{Li}^+(\text{electrolyte}) + e^-$ (electrode), or equivalently, $\text{Li}^+(\text{electrode}) \leftrightarrow \text{Li}^+(\text{electrolyte})$. This equilibrium condition, illustrated in the center panel of **Figure 13**, implies that the electrochemical potential of Li^+ is equal in the electrode and electrolyte: $\eta_{\text{Li}^+}^{\text{electrode}} = \eta_{\text{Li}^+}^{\text{electrolyte}}$. During (dis)charge, however, the interface is not in equilibrium and an electrochemical potential difference $\Delta\eta_{\text{Li}^+} = \eta_{\text{Li}^+}^{\text{electrode}} - \eta_{\text{Li}^+}^{\text{electrolyte}}$ drives the transfer of Li^+ ions, as illustrated in the left and right panels of Figure 13; this is analogous to how a difference in temperature drives the flow of heat. The drop in electrochemical potential across the electrode/electrolyte interface manifests as a decrease in discharge voltage and an increase in charge voltage relative to the thermodynamic equilibrium voltage, as discussed in Appendix A.

Although in the present analysis we focus on the Li^+ electrochemical potential, some literature instead chooses to describe ion-transfer kinetics in terms of the difference in electrostatic potential across the interface, $\Delta\phi$. The two descriptions are identical, however, due to the equality $\Delta\eta_{\text{Li}^+} = e(\Delta\phi - \Delta\phi_{\text{eq}})$, where $\Delta\phi = \phi^{\text{electrode}} - \phi^{\text{electrolyte}}$ is the drop in electrostatic

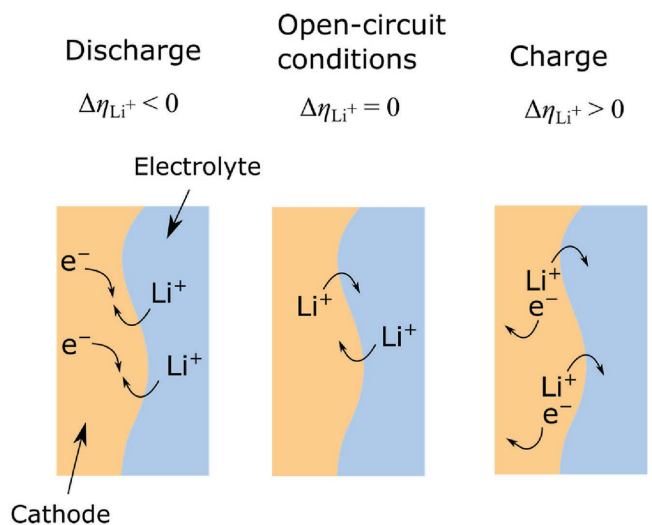


Figure 13. Schematic illustration of how differences in Li^+ electrochemical potential drive ion-transfer kinetics at the electrode/electrolyte interface.

potential across the interface and $\Delta\phi_{\text{eq}} = -(\mu_{\text{Li}^+}^{\text{electrode}} - \mu_{\text{Li}^+}^{\text{electrolyte}}) / e$; see Appendix A for details.

The simplest description of interfacial ion-transfer processes is the Butler–Volmer model, which relates the current density j to the difference in Li electrochemical potential across the interface $\Delta\eta_{\text{Li}^+}$ ^[92]

$$j = j_0 \left\{ \exp\left[\frac{\alpha\Delta\eta_{\text{Li}^+}}{k_{\text{B}}T}\right] - \exp\left[-\frac{(1-\alpha)\Delta\eta_{\text{Li}^+}}{k_{\text{B}}T}\right] \right\} \quad (7)$$

The two terms represent the rates at which ions cross the interface in each direction, with j_0 being the exchange current density and α a symmetry factor. (Equation (7) differs subtly from the original expression of the Butler–Volmer model: instead of describing electron-transfer rate in terms of differences in electron electrochemical potential, Equation (7) expresses ion-transfer rate in terms of differences in Li^+ electrochemical potential).

The value of the exchange current provides a quantitative measure of how facile ion-transfer is. Importantly, the exchange current density may vary with temperature and Li

concentration. Experimental measurement of the exchange current density is often based on the behavior in the low-current regime. In this limit, the Butler–Volmer model reduces to an Ohmic resistor $\Delta\phi - \Delta\phi_{\text{eq}} = JR$ with a resistance of $R = k_{\text{B}}T / Aj_0e$, where J is the total current and A is the electrochemically active surface area of the electrode. This resistance is referred to as the “ion-transfer resistance” or sometimes “charge-transfer resistance.”

Ion-transfer kinetics at layered lithium oxide interfaces have been indirectly probed through electrochemical impedance spectroscopy (EIS). Ion-transfer resistances measured by EIS imply exchange current densities on the order of 0.1–10 mA cm^{-2} for layered oxides.^[113,114] However accurate measurements of ion-transfer kinetics are difficult; for example, determining the electrochemically active surface area is non-trivial, especially if the particles crack during (de)lithiation. Ion-transfer kinetics are also expected to vary with different crystallographic surface facets, with {0001} surfaces impeding ion insertion.^[115,116] Extensive studies of interfacial ion transfer at graphitic anodes may serve as a useful starting point for the understanding of ion-transfer at layered oxide cathodes.^[117]

2.4.3. Phase-Transformation Kinetics

Phase-transformation kinetics can result in a hysteresis in the voltage curve that arises from a free-energy barrier for individual crystallites to undergo a phase transformation.^[44,118–120] This free-energy barrier represents the coherency strain energy and interfacial energy that exists during two-phase coexistence within a single particle.^[118] To illustrate this phenomenon, we consider the free energy of a hypothetical ensemble of particles, as shown in **Figure 14**. The left panel shows the equilibrium state of the ensemble as a function of composition. The common-tangent construction shows that at intermediate compositions, the equilibrium state is a two-phase coexistence with some particles being Li-rich and others Li-deficient. During (de)intercalation, the particles will one-by-one transform between the Li-rich and Li-deficient phases. However, to drive the transformation of individual particles at an appreciable rate, an overpotential needs to be applied; this can be seen by considering the free energy curve for a single particle, shown in the center panel of **Figure 14**. Because coherency strain

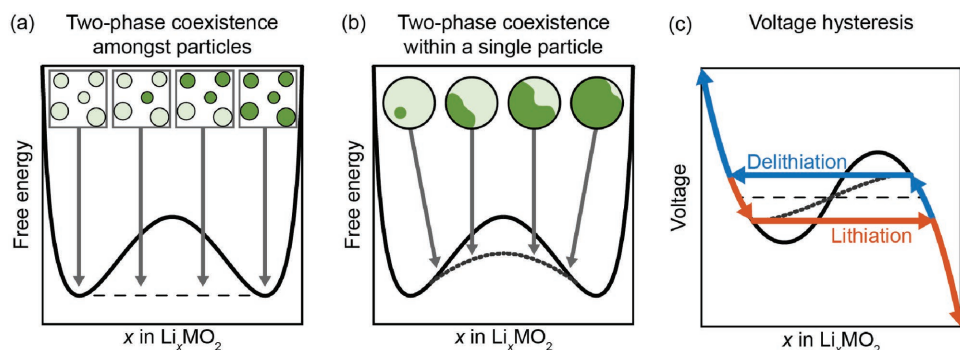


Figure 14. Schematic illustration of how coherency strains lead to a barrier for phase transformation. a) Free energy for two-phase equilibrium amongst multiple particles, derived by the common tangent construction. b) Free energy for a coherent two-phase mixture within a single particle. c) Hysteresis in the voltage curve resulting from coherency strain.

and interfacial energy penalize two-phase coexistence within a single particle, the free energy at intermediate compositions (dashed line in Figure 14b) is higher than the common tangent construction. Overcoming this barrier requires that a voltage above/below the equilibrium voltage be applied on charge/discharge.^[118,121] This results in a hysteresis in the voltage curve, as shown in the right panel of Figure 14.

In some cases, the coherency strain and interfacial energy can be large enough to suppress phase separation within individual particles.^[119,122] This occurs when the free energy for a coherent two-phase mixture is higher than that of a homogeneous solid solution, and results in an electrochemical hysteresis similar to the nucleation and growth mechanism above. This suppression of phase separation by coherency strains has been recently hypothesized to occur in Li_xFePO_4 , where a hysteresis of ≈ 20 mV remains even at rates as low as $C/1000$.^[44,119]

For coherent phase transformations that involve only a change in Li concentration without any crystallographic changes (aside from modest differences in lattice parameter), the above kinetic phenomena can be described by classical Cahn–Hilliard models for spinodal decomposition.^[123] Although this formalism was originally developed to describe quenching into a miscibility gap from high temperature, it can equally describe phase transformation kinetics in battery materials (i.e., movement through the miscibility gap at constant temperature by changing Li concentration).^[124] The hypothesized suppression of phase separation in Li_xFePO_4 ^[119] is analogous to Cahn’s picture of spinodal decomposition, where coherency strains suppress two-phase decomposition by lowering the maximum temperature of the miscibility gap when the free energy of a solid solution is less costly than the strain free-energy penalty of coherent two-phase coexistence.^[123]

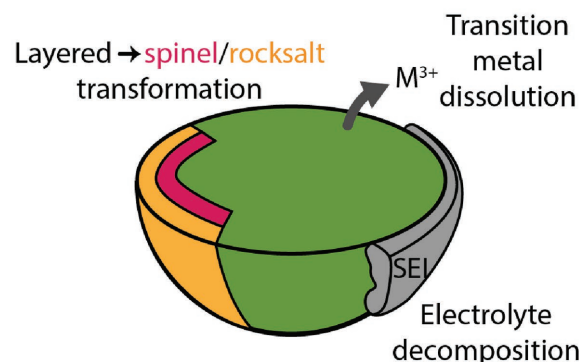
Although Figures 7 and 8 show the phase transformation propagating across a particle, the geometry of the transformation will depend on the kinetics of nucleation, phase-boundary propagation, Li diffusion, and Li^+ ion exchange with the electrolyte. Coherency strain, as well as interfacial and surface energies, also play important roles.^[44,118] Perhaps the simplest transformation geometry is the core–shell model, where the transformation starts on the surface and propagates inward. Another geometry is 1D propagation along the crystallographic axis that minimizes coherency-strain energy.

The dynamics of phase transformations in the layered oxides are not fully understood, especially in the case of stacking-sequence phase transformations. Stacking-sequence changes can be realized by the passage of partial dislocations through the crystal.^[125] In this picture, the interface between different stacking sequences consists of an array of partial dislocations; this allows for a coherent interface, despite the crystallographic differences between the two phases.

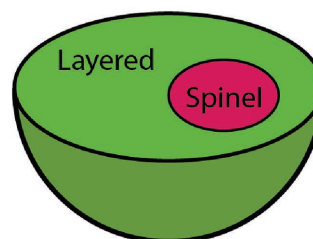
2.5. Degradation Mechanisms

Kinetic limitations can be compounded by many different degradation processes that reduce battery performance over time. This section summarizes conceptually the degradation challenges that have been hypothesized, which are summarized in

(a) Surface decomposition



(b) Bulk transformation to spinel



(c) Mechanical degradation

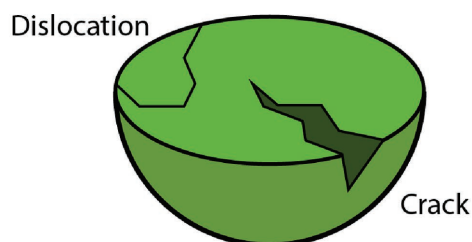


Figure 15. Degradation mechanisms in layered lithium oxides.

Figure 15. Although it is useful to think of these as separate phenomena, they in fact are deeply interconnected.

2.5.1. Transformations to Spinel- and Rocksalt-Like Phases

As discussed in Section 2.1, the layered oxides all exhibit strong thermodynamic driving forces upon deintercalation to transform to spinel via the rearrangement of cations and to transform to rocksalt via the evolution of oxygen. The cyclability of Li-ion batteries is possible only because of the kinetic limitations in these transformations. Transformations to the cubic phases nevertheless occur near the surface in essentially all layered oxides, as shown in Figure 16, with a rocksalt-like phase with approximate composition MO on the surface and a spinel-like phase in the subsurface.^[126] While the layered structure of the O3 phase can be seen in the bulk, the presence of transition-metal ions in the Li layer (characteristic of the cubic phases) can be seen near the surface.

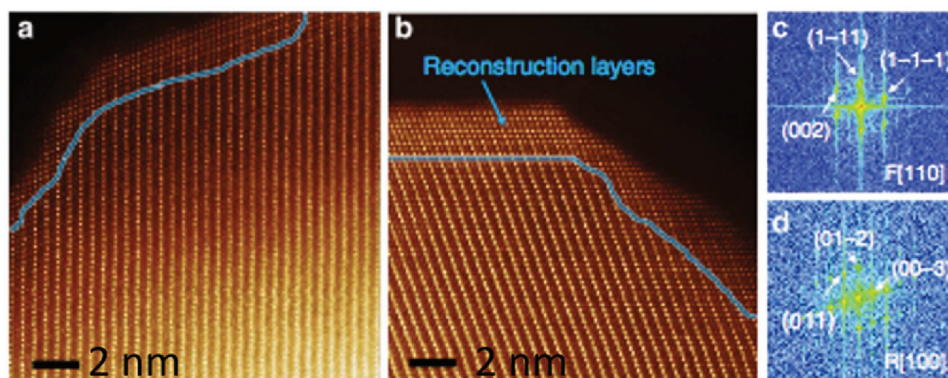


Figure 16. Rearrangement of transition-metal sites from layered to cubic in NMC, as visualized by atomic resolution annular dark-field scanning transmission electron microscopy (ADF-STEM). a) ADF-STEM after storing in the electrolyte for about 30 h (equivalent to the amount of time for one cycle), b) ADF-STEM upon cycling between 2.0–4.7 V, c,d) Fourier transform from the reconstruction layer with cubic structure and the bulk with rhombohedral structure. Reproduced with permission.^[126] Copyright 2017, Macmillan Publishers.

These surface reactions have traditionally been viewed as an undesirable process, as the poor conductivity of the cubic phases (see Section 2.4.1) can increase cell impedance. However, surface reconstruction layers may in fact be critical to the success of layered oxide cathodes: by forming a passivating layer, they may protect the cathode in much the same way as an SEI protects the anode.

The mechanistic triggers that initiate oxygen loss and surface reconstruction are not well understood. One interpretation is that it is the depletion of oxygen 2p states upon deintercalation, due to hybridization with transition-metal d orbitals (Figure 6), that triggers oxygen loss.^[23] As these states deplete, holes self-trap in oxygen p states to form peroxide O_2^{2-} dimers, which, being highly reactive, will result in oxygen loss.

The rate of layered \rightarrow cubic transformations is also influenced by the barrier for transition-metal migration from octahedral sites in the transition-metal layer to octahedral sites in the lithium layer, which occurs via diffusion through tetrahedral sites. Although Ni, Mn, and Co have similar sizes, the migration barriers vary significantly because of the effect of crystal-field splitting and other electronic-structure effects on the relative energies of octahedral and tetrahedral sites.^[66,67] Experiments have found that Li_xMnO_2 is particularly susceptible to transformations to spinel (see Section 3.1.3).^[60,127,128] DFT calculations suggest that this is because Mn is highly stable in the tetrahedral sites when reduced to 2+ via the disproportionation reaction $2Mn^{3+} \rightarrow Mn^{2+} + Mn^{4+}$, resulting in a low barrier for interlayer migration.^[66,67]

Surface reconstructions are not only controlled by the cathode material itself, they are also strongly coupled to the environmental conditions and interactions with the electrolyte. Recent experiments have illustrated this elegantly by examining the susceptibility of NCA to surface reconstructions upon exposure to different gases: O_2 gas delays the onset of densification, while reducing environments such as H_2 gas promote it.^[129]

2.5.2. Reactions at the Cathode/Electrolyte Interface

The reaction of the cathode material with the electrolyte and other inactive cell components can degrade battery

performance, and is likely related to surface transformations to rocksalt spinel. These surface reactions potentially include chemical and electrochemical reactions involving the active material, solvent, salt, binder, and conductive additives. One of the consequences of these surface reactions is the dissolution of transition-metal species that can poison the anodic SEI.^[33,34,130] Another consequence is the formation of a SEI-like film on the cathode, consisting of several compounds including Li_2CO_3 , LiF, and alkyl carbonates.^[33,34,130] This film could contribute to performance degradation if this impedes Li^+ transport, or if continual growth consumes Li.

The mechanisms by which the cathode surface reacts with the electrolyte are not fully understood. Earlier conventional wisdom held that transition-metal dissolution occurs via attack by hydrofluoric acid (HF) generated by the reaction of $LiPF_6$ and other fluorine-containing compounds with water and other protic contaminants.^[14,34] This picture was originally inspired by the chemical conversion of spinel $LiMn_2O_4$ to MnO_2 in acidic aqueous solutions.^[131] However, more recent studies finding that the dissolved transition-metal ions form organometallic complexes suggest that direct reactions between the cathode and organic solvent molecules, rather than acid attack, may be the dominant transition-metal dissolution mechanism in many cell designs.^[132]

Studies of surface reactivity focused on the spinel lithium nickel manganese oxides suggest that surface reactions could occur by the transfer of electrons from solvent molecules to surface transition-metal ions accompanied by the donation of protons from the solvent to surface oxygen sites or salt anions.^[132,133] Furthermore, the oxygen released during the densification of layered phases to MO rocksalt may react with the electrolyte. However, because of the complexity of the reactions and interfacial structure, more work is needed before these processes can be fully understood.

Understanding surface reactions occurring during cycling is further complicated by the fact that the cathode/electrolyte interface is not clean to begin with.^[33,130] First, impurities such as Li_2CO_3 are typically leftover on the surface of layered oxides after synthesis. Second, the layered materials and impurities on their surfaces will undergo chemical reactions when placed in contact with the electrolyte, before any voltage is applied.

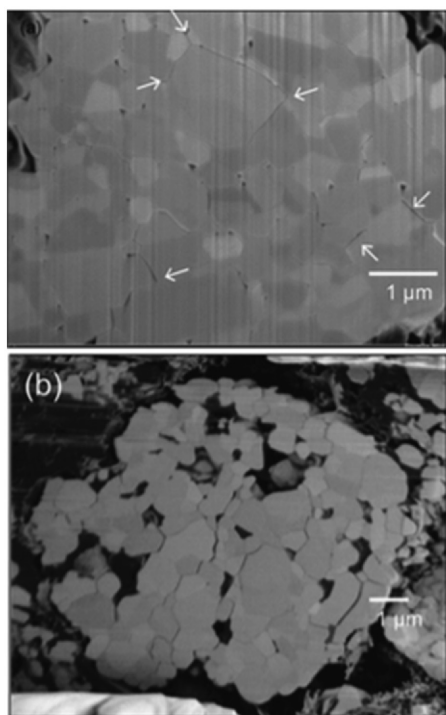


Figure 17. SEM images of a single $\text{Li}(\text{Ni}_{0.8}\text{Co}_{0.15}\text{Al}_{0.05})\text{O}_2$ particle showing the formation of cracks a) after one cycle and b) after 4500 cycles. The arrows in panel (a) indicate the positions of cracks inside the particle. Adapted with permission.^[135] Copyright 2013, Wiley-VCH.

2.5.3. Mechanical Degradation

Mechanical degradation, e.g., fracturing (often along grain boundaries) and the accumulation of dislocations, can contribute significantly to performance loss (Figure 15c).^[134] Mechanical failure hinders performance because (i) fracture can result in loss of electrical contact between active material particles and the current collector, and (ii) cracks in the active material or surface passivating layers expose virgin active material to the electrolyte, potentially resulting in further surface reactions. However, some mechanical changes could potentially have beneficial effects. For example, microcracks that allow the electrolyte to penetrate deep into particles could improve Li-ion transport.

Figures 17 and 18 illustrate ways in which mechanical changes alter the structure. In Figure 17,^[135] small microcracks along grain boundaries formed after one cycle (top panel) grow into large cracks and voids after repeated cycling (bottom panel). Figure 18^[136] shows how surface reactions can occur on the material exposed by microcracks, resulting in the formation of a cubic phase along the grain boundaries. This appears in Figure 18a as an ≈ 20 nm thick white layer. Panels A1, B1, and C1 show how the structure transforms from layered to cubic as one approaches the surface exposed by the crack.

Mechanical degradation is often attributed to the substantial shape/volume changes that occur during (de)lithiation, especially the precipitous drop in interlayer spacing at high states of charge.^[134] This can cause mechanical stresses in two ways. First, shape/volume changes can lead to large stresses as expanding particles impinge on each other. Second, the

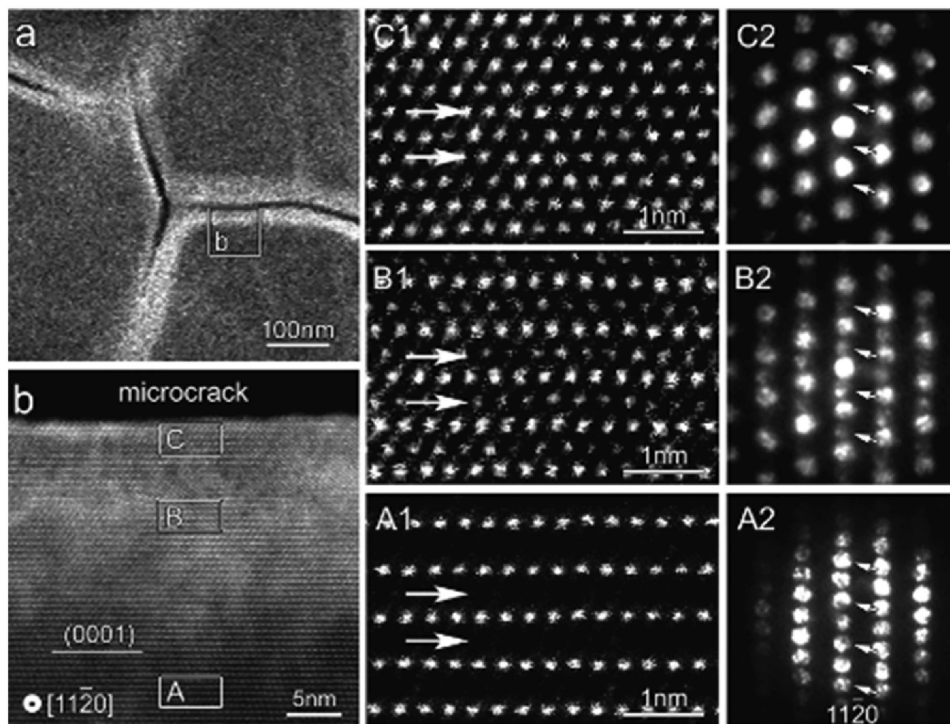


Figure 18. Microcracks formed along grain boundaries during the first cycle of an NCA cathode, visualized by scanning tunneling electron microscopy (STEM). High-magnification STEM images (A1, B1, and C1) and diffraction patterns (A2, B2, and C2) illustrate the transformation from layered to rocksalt near the microcrack, and correspond to the regions marked A, B, and C in panel (b). Reproduced with permission.^[136] Copyright 2011, The Electrochemical Society.

coherency strain caused by the inhomogeneous (de)lithiation of individual crystallites can result in internal stresses. Such lattice mismatch can occur either because of phase separation (e.g., during an O1 \leftrightarrow O3 transition), or because of concentration gradients that emerge due sluggish Li diffusion or high rates (sometimes referred to as “electrochemical shock”^[137]).

3. Materials

This section discusses how the phenomena enumerated above play out in state-of-the-art cathode materials. We first consider the baseline materials, Li_xCoO_2 (LCO), Li_xNiO_2 (LNO), and Li_xMnO_2 (LMO), and then discuss the alloys NCA and NMC, represented by formulas $\text{Li}_x(\text{Ni}_y\text{Co}_z\text{Al}_{1-y-z})\text{O}_2$ and $\text{Li}_x(\text{Ni}_y\text{Mn}_z\text{Co}_{1-y-z})\text{O}_2$. (While in some contexts “alloy” refers exclusively to solid solutions of elemental metals, here we will use it to refer to solid solutions of metal cations over the transition metal sites of oxides.) The voltage curves (Figure 19) and interlayer spacing (Figure 20) illustrate some of the similarities and differences between these materials, such as the lower redox potential for Ni than Co (cf. Figure 6) and the stronger tendency for lithium/vacancy ordering in the pure materials (LCO and LNO) as compared to the alloys (NCA and NMC). (Lithium/vacancy ordering results in sharp features in the voltage curve, whereas a disordered solid solution will generally exhibit a smooth charging profile.) These differences are discussed in more detail in the sections below. Figures 19 and 20 exclude Li_xMnO_2 because this material does not retain the layered structure upon deintercalation, as discussed below.

3.1. Baseline Materials

3.1.1. Li_xCoO_2

LCO can be thought of as the prototypical layered Li-intercalation oxide because of its advent as the first widely adopted

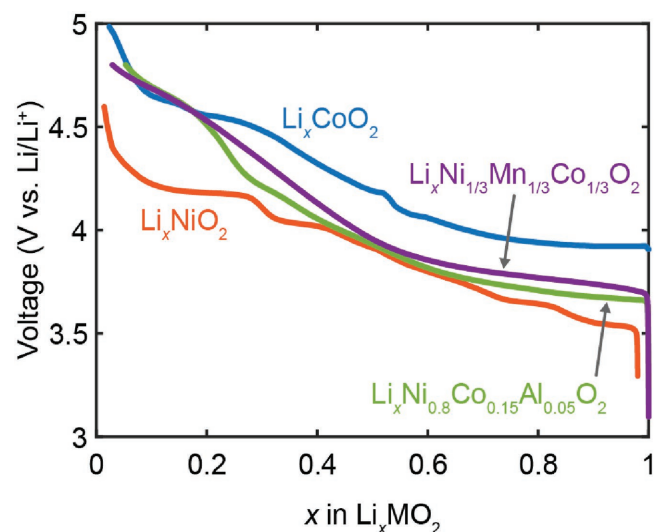


Figure 19. Voltage curves upon first charging of different layered oxides.^[75,138] Data for NCA and NMC courtesy K. Wiaderek.

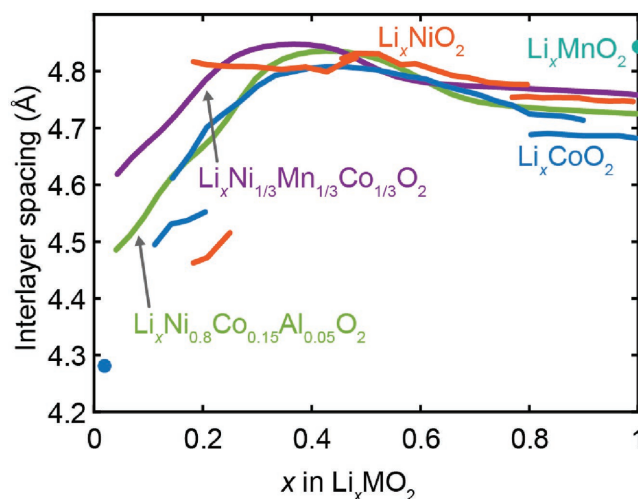


Figure 20. Interlayer spacing as a function of state of charge for different layered oxides.^[127,139,140] Data for NCA and NMC courtesy K. Wiaderek.

Li-ion cathode. It was first proposed as a cathode material by the Goodenough group in 1980,^[141] and then launched commercially by Sony in 1991. (See earlier works by Whittingham,^[12] Goodenough,^[48] and Thackeray et al.^[25] for a detailed history of Li-ion batteries.) Despite its long history, the practical capacity of LCO remains about half of its theoretical capacity.^[12,13] Mechanical damage has been widely observed through transmission electron microscopy (TEM)^[142–145] and acoustic emission monitoring^[146] when LCO is charged beyond its practical capacity. This can be attributed to large shape and volume changes during (de)intercalation, including those associated with first-order phase transformations from O3 to H1-3 and then to O1 stacking sequences at high states of charge ($x < 0.2–0.3$).^[52,139,147–149] Surface reactions and reconstructions have also been observed. This includes the formation of an SEI-like film on LCO,^[150] the dissolution of cobalt,^[151] and transformation to the spinel phase.^[143]

LCO exhibits a rich phase diagram with numerous phase transitions occurring upon (de)intercalation, which manifest as bumps and kinks in the voltage curve (Figure 21). As LiCoO_2 is deintercalated, the material first undergoes a first-order transformation from an insulating phase to a metallic phase (either a Mott^[69] or Anderson transition^[70]), resulting in a large plateau. Further deintercalation results in a sloping voltage curve in a single-phase region. However, two bumps in the voltage curve occur within this single-phase region, near $x = 1/2$. These represent continuous (or nearly continuous) phase transitions associated with the row ordering of Li^+ ions, which reduces the crystal symmetry from rhombohedral to monoclinic. A voltage plateau representing two-phase coexistence separates the O3 solid solution and a hybrid O1/O3 (H1-3) solid solution, which appears as a small step around $x = 0.2$. Further deintercalation results in a two-phase coexistence of O1/O3 and O1.

The Li content on the x -axis in Figure 21 is somewhat misleading: simple Coulomb counting can lead to systematic errors in estimating the state of charge. This could arise, for example, if not all cathode particles are electrically connected or if there was some uncertainty in the initial composition.^[59] We have

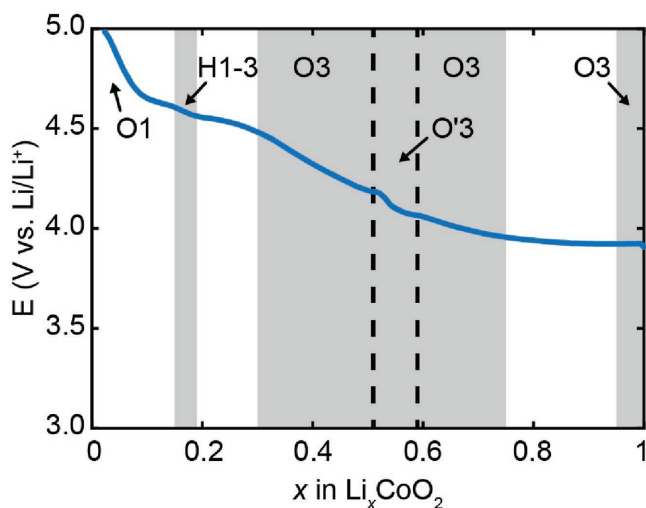


Figure 21. Voltage curve and phase diagram for Li_xCoO_2 .^[138] Gray regions represent single phases, white regions two-phase equilibria, and dashed lines continuous phase transitions.

nevertheless chosen to align the phase boundaries with features in the voltage curve to highlight the connection between the shape of the voltage curve and intercalation thermodynamics.

Of all the layered oxides, LCO is arguably the one for which diffusion has been the most closely examined. As discussed in Section 2.4.1, the Li diffusion coefficient in Li_xCoO_2 is strongly dependent on the state of charge.^[95,100,101] Diffusion is fastest around $x = 0.4$ because full lithiation results in a scarcity of divacancies and full delithiation results in large migration barriers.^[97] Additionally, the diffusion coefficient exhibits features around $x = 0.5$ due to the row ordering of lithium at this composition.

3.1.2. Li_xNiO_2

Li_xNiO_2 (LNO) could in principle offer a dramatic reduction in cost over LCO due to the low price of nickel relative to cobalt; however, LNO was unable to achieve adequate performance to supplant LCO. The main differences between LNO and LCO are that LNO exhibits lower voltages and a much greater degree of off-stoichiometry.^[40,73,152] In other aspects, such as stacking-sequence changes,^[77] LNO behaves similarly to LCO.

As can be seen from the voltage curves (Figure 19), (de)intercalation occurs at voltages about 0.2–0.3 V lower in LNO than LCO because nickel redox involves e_g orbitals rather than t_{2g} orbitals (see Section 2.2). This shift in voltage has important consequences for electrochemical performance and the interpretation of experimental data. In particular, the difference in (de)intercalation voltage means that the common practice of comparing electrodes cycled over a fixed voltage range does not necessarily provide an apples-to-apples comparison. For example, based on the voltage curves in Figure 19, we would expect charging to 4.2 V to extract 90% of the Li from LNO but only 50% of the Li from LCO.

Like LCO, LNO experiences a number of phase transitions that appear as steps and kinks in the voltage curve (Figure 22).

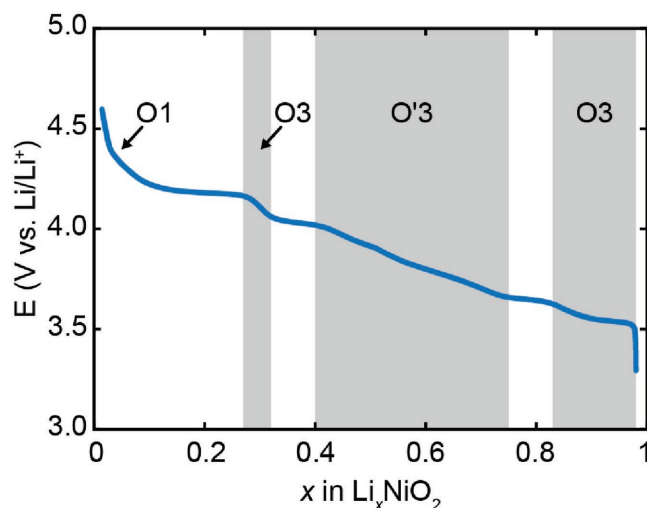


Figure 22. Voltage curve and speculative phase diagram for Li_xNiO_2 .^[75] Gray regions represent single phases and white regions two-phase equilibria.

Upon deintercalation, LNO undergoes a first-order phase transformation from O3 to a monoclinic phase, with the lowering in symmetry driven by the Jahn–Teller activity of the Ni^{3+} ions and the ordering of Li ions.^[72,73] Further deintercalation is accompanied by additional first-order transformations, first to a rhombohedral phase with a $\sqrt{3} \times \sqrt{3}$ Li ordering and then to O1.^[72,73]

Unlike other layered transition-metal oxides, LNO suffers from a tendency for Ni atoms to reside in the Li layer,^[40,152] which manifests itself in the voltage curve (Figure 22) as a reduction in the maximum Li content. This off-stoichiometry is believed to arise from the occupation of Li^+ sites by Ni^{2+} ions. In order to balance charge, an equal number of Ni^{3+} ions in the transition-metal layer are reduced to Ni^{2+} , resulting in a net formula of $\text{Li}_{1-y}\text{Ni}_y^{2+}\text{Ni}_{1-y}^{3+}\text{O}_2$ in the fully lithiated state.^[152] This off-stoichiometry can be mitigated by doping with other elements, such as Co; this is discussed in more detail in the context of NCA alloys below (Section 3.2.1).

The presence of Ni in the Li layer has negative consequences for electrochemical performance, especially first-cycle capacity loss.^[152,153] One possible explanation is that when Ni^{2+} in the Li layer oxidizes to the smaller Ni^{3+} during charging, it results in a contraction of the interlayer spacing, making the reinsertion of Li difficult.^[152,153] It has also been suggested that the contraction of the interlayer spacing induced by substituting Ni for Li would increase the migration barrier for Li diffusion;^[102,103] this hypothesis is corroborated by experimental evidence that Li diffusion is somewhat slower in Li_xNiO_2 as compared to Li_xCoO_2 .^[104,105] On the other hand, the presence of Ni in the Li layer has one potentially beneficial effect: preventing stacking sequence changes to O1.^[75] This can be attributed to the face-sharing of cation sites in the O1 structure, as discussed in Section 2.

While many studies have investigated the fully intercalated LiNiO_2 , some questions remain about the details of its structure. Although Ni^{3+} is Jahn–Teller active, LiNiO_2 appears to retain rhombohedral (or nearly rhombohedral) symmetry even at low temperature;^[154,155] however, the presence of two distinct

Ni–O bond lengths indicates the material is locally distorted.^[154] Several possible explanations for these facts have been hypothesized, including: (i) the disruption of long-range ordering of Jahn–Teller distortions by defects;^[154] (ii) the formation of complex noncollinear orderings of Jahn–Teller distortions;^[155,156] and (iii) the disproportionation of Ni³⁺ to Ni²⁺ and Ni⁴⁺.^[157]

3.1.3. Li_xMnO_2

Layered Li_xMnO_2 (LMO) has also been considered as an intercalation electrode, although it was not until 1996 that well-layered LiMnO_2 was synthesized.^[158,159] (The greater difficulty in producing layered LiMnO_2 compared to LiCoO_2 and LiNiO_2 can be attributed to the Mn^{3+} being closer in size to Li^+ .) Layered Li_xMnO_2 is not practical as a cathode material because it rapidly transforms to the spinel phase upon cycling, resulting in an irreversible loss of capacity.^[60,127,128] As discussed in Section 2.5.1, the ease by which this transformation occurs has been attributed to the facile migration of Mn to the Li layer via the dumbbell mechanism;^[66,67] this mechanism is thought to be quite fast for Mn because of the high stability of Mn^{2+} in the tetrahedral sites, which serve as an intermediate step in the interlayer migration.

Even if Li_xMnO_2 were able to retain the layered structure upon cycling, one would expect it to have poor reversibility. First, Mn, when in the +3 oxidation state, is particularly susceptible to dissolution in the electrolyte.^[160] Second, the strong Jahn–Teller activity of the Mn^{3+} ion causes LiMnO_2 to adopt the monoclinic $\text{O}3$ structure.^[58,127,158,159] The removal of this distortion upon deintercalation will result in large mechanical stresses that could fracture the material. Both of these problems (Mn dissolution and large strains associated with Jahn–Teller distortions) are recognized to significantly limit the cyclability of spinel $\text{Li}_x\text{Mn}_2\text{O}_4$ cathodes.^[45,46,60,151] Because the challenges associated with Mn-based cathodes are associated with reduced cations (Mn^{3+} and Mn^{2+}), alloying with nickel to keep Mn oxidized to 4+ can mitigate these problems; this is discussed in more detail below in the context of Ni–Mn–Co alloys.

3.2. Candidate Materials

While LCO was the first commercially successful Li-ion cathode material, current battery manufacturing has pivoted toward alloys which offer superior performance, especially Ni–Mn–Co (often referred to as NMC or NCM) and Ni–Co–Al (NCA) oxides.^[24] In part, this doping serves to dilute expensive and toxic elements, such as cobalt, with elements that are safe and inexpensive, such as aluminum and manganese. However, alloying can also have synergistic effects in which the whole is more than the sum of the parts, and the alloy performs better than any of the end members.

3.2.1. NCA

NCA emerged in the early 2000s as an improvement to the Li_xCoO_2 chemistry.^[15,16] As of 2017, it is widely used

commercially, including in Tesla electric vehicles.^[24] It typically is formulated to be Ni-rich with only a small amount of Al, often as $\text{Li}(\text{Ni}_{0.8}\text{Co}_{0.15}\text{Al}_{0.05})\text{O}_2$.^[161–163] Aluminum, which is electrochemically inactive, can stabilize the layered structure and cell impedance, thus improving the performance. However, like the other layered oxides, NCA battery materials undergo capacity fading upon cycling at high temperatures and high current rates.^[164]

Comparing the NCA voltage curve (Figure 19) to the voltage curves for LCO and LNO, which represent end members of the NCA composition space, illustrates some of the key effects of alloying. First, when Ni–Co alloys are deintercalated, Ni is oxidized before Co,^[40] as expected from the relative alignment of redox levels (Figure 6). Thus for large x the NCA has a similar voltage to LNO, but for small x NCA has a similar voltage to LCO. Second, unlike LCO and LNO, the NCA alloy exhibits a very smooth and featureless voltage curve due to the absence of pronounced phase transitions.^[165] This loss of lithium/vacancy ordering upon alloying occurs in many layered oxides, and can be attributed to the disruption of long-range Li ordering by the random arrangement of transition metals.^[40]

One synergistic benefit of alloying in NCA is that the presence of Co reduces the degree of Li/Ni off-stoichiometry. This has been attributed to the smaller size of Co, which results in a slight compression of the transition metal layer that destabilizes the Ni^{2+} ions needed to charge-compensate excess Ni in the Li layer.^[166]

The role of Al is less clear, particularly given that even a small amount has been reported to have a beneficial effect on the cycle life and thermal stability of layered oxides.^[15,167–170] One hypothesis is that the Al, being electrochemically inactive, improves stability by preventing full delithiation.^[15,168] The presence of this residual lithium may also explain why transformations to O1 are not observed in NCA.^[163] Additionally, Al is thought to raise the voltage for lithium (de)intercalation,^[83] although the voltage shift will be very small at 5% doping levels.

Understanding the distribution of Al within the material is central to unraveling its effects on performance. Experiments have found a tendency for $\text{Li}(\text{Ni}_{1-y}\text{Al}_y)\text{O}_2$ to segregate into coherent Ni-rich and Al-rich domains for nondilute Al concentrations ($y \geq 0.1$).^[171] However, recent NMR and atom-probe tomography work has shown Al to be uniformly distributed in the standard $\text{Li}(\text{Ni}_{0.8}\text{Co}_{0.15}\text{Al}_{0.05})\text{O}_2$ material.^[172]

NCA nevertheless experiences capacity fade associated with surface reactions and mechanical degradation. Transformations to rocksalt/spinel-like structures have been extensively observed using S/TEM^[173–175] and X-ray absorption spectroscopy (XAS).^[176–178] Mechanical degradation in NCA has been extensively documented using TEM^[136] and scanning electron microscopy (SEM).^[135]

3.2.2. NMC

Several studies in the early 2000s revealed the benefits of alloying the baseline materials LiCoO_2 , LiNiO_2 , and LiMnO_2 together to form a layered Ni–Mn–Co lithium oxide $\text{Li}_x\text{Ni}_y\text{Mn}_z\text{Co}_{1-y-z}\text{O}_2$ (NMC).^[17–20] NMCs, sometimes blended with spinel oxides, are used commercially in electric vehicles

such as the Nissan Leaf and Chevrolet Volt.^[24] NMC often is formulated as $\text{Li}_x(\text{Ni}_{1/3}\text{Co}_{1/3}\text{Mn}_{1/3})\text{O}_2$, referred to as NMC 333 (or sometimes NMC 111). However there is also much interest in Ni-rich NMCs, such as $\text{Li}_x(\text{Ni}_{0.5}\text{Co}_{0.3}\text{Mn}_{0.2})\text{O}_2$ (NMC 532).

In some aspects, NMC alloys behave similarly to NCA alloys. The presence of Co reduces the degree of Li/Ni off-stoichiometry, although a Li/Ni mixing of 1%–6% is still commonly observed.^[12,163] The alloying of Ni, Mn, and Co also suppresses lithium/vacancy ordering, resulting in a smooth voltage curve characteristic of a solid solution. However, unlike NCA, NMC alloys can exhibit transformations to O1 upon extreme delithiation.^[179]

The addition of Mn results in qualitative differences between NMC and NCA. While Mn generally improves cyclability^[17–20] and thermal stability,^[17,180] the detailed mechanisms are complex. As discussed in Section 2.2, the $\text{Mn}^{3+}/\text{Mn}^{4+}$ couple in layered NMC has a lower equilibrium voltage than the $\text{Ni}^{2+}/\text{Ni}^{3+}$ couple.^[23,79] As a result, in the fully lithiated state, Mn is oxidized to 4+ while Ni is reduced to 2+. During deintercalation, first Ni is oxidized from 2+ to 4+, followed by the oxidation of Co from 3+ to 4+, while Mn remains unchanged.^[23,40,79]

The Ni–Mn charge transfer, which results in the oxidation of Mn to Mn^{4+} , is thought to mitigate the failure modes inherent to layered and spinel oxides containing Mn^{3+} . First, the transformation to spinel is mitigated; presumably this is because Mn^{4+} is unlikely to migrate to tetrahedral sites because it cannot be readily reduced to Mn^{2+} . Second, Mn^{4+} is less susceptible to dissolution than Mn^{3+} .^[160] For example, one study found the rate of Mn dissolution to be around 16 times slower in NMC 333 than LiMn_2O_4 .^[160] Third, keeping Mn oxidized to 4+ avoids mechanical stresses associated with Jahn–Teller distortions arising from Mn^{3+} .

However, a clear understanding of why Mn doping improves Ni–Co alloys is lacking. One potentially important effect of Mn doping is that electrostatic interactions between Ni^{2+} and Mn^{4+} may result in strong short-range ordering (or possibly even nanoscale phase separation) in NMCs favoring Ni–Mn coordination.^[181] It has also been hypothesized that Ni–Mn charge transfer will enhance Li diffusion at low states of charge because tetrahedral sites that are face-sharing with a 2+ transition metal will experience less electrostatic repulsion than those face-sharing with 3+ transition metals; a percolating network of such sites could lead to facile long-range diffusion.^[102,103] Lastly, the decrease in oxidation state of Ni due to the donation of electrons by Mn could potentially reduce surface reactions associated with oxidized Ni.

Despite these synergistic effects of Ni–Mn–Co alloying, NMC nevertheless exhibits surface and mechanical degradation. Surface reconstructions to spinel/rocksalt have been widely observed in NMC cathodes after electrochemical cycling, as observed by XAS,^[182] S/TEM,^[183] and X-ray photoelectron spectroscopy (XPS).^[184] The dissolution of transition-metal ions and their deposition on the anode has also been observed.^[160,185] Mechanical degradation has been widely observed in NMC materials using SEM and TEM,^[186] including microcracks similar to those seen in the other layered oxides.

4. Modifications and Extensions

Many strategies for narrowing the gap between the theoretical and practical energy densities of layered oxides have been proposed. This section first discusses modifications based on altering the composition of the bulk material through doping and overlithiation, as well as modifying the composition near the surface through surface modification and core–shell structures. Although this review focuses on the cathode material itself, a section on high-voltage electrolytes is included because of the important role that electrolyte composition plays in interface stability. Lastly, extensions beyond layered lithium oxides are discussed, including the replacement of Li with other intercalants (e.g., Na), and disordered-rocksalt electrode materials.

4.1. Surface Modification

Many surface modifications have been applied to improve the electrochemical performance of classical layered oxides. The common idea is to reduce potential side reactions and their effects, including transformations to rocksalt/spinel, the dissolution of transition-metal ions, and the formation of an undesirable SEI-like film between electrode and electrolyte at high working voltage.^[187] Surface modifications can be thought of as an artificial SEI, serving as a Li^+ -conductive passivation layer.

A good surface coating layer should possess several key properties:

1. The coating should be a thin layer uniformly distributed on the particle surface so as to minimize weight.
2. The coating material should be a good Li-ion conductor and electron conductor.
3. The coating material should be electrochemically stable within the operating voltage window.
4. The coating should have a high enough mechanical strength to prevent fracture associated with shape/volume changes of the electrode during (de)intercalation.

The most widely used surface modification materials (Table 1) are oxides (e.g., ZrO_2 ,^[188] CeO_2 ,^[189] Al_2O_3 ,^[190–195] ZnO ,^[196] CuO ,^[197] and Sb_2O_3 ^[198]), fluorides (e.g., AlF_3 ,^[199–203] LaF_3 ,^[204] and ZrF_x ^[205]), and phosphates (e.g., FePO_4 ^[206] and AlPO_4 ^[207]). However, most of these materials have poor electronic and ionic conductivity. Learning from the case of LiFePO_4 , carbon has also been used as a coating layer on classical layered oxides in order to improve the electronic conductivity of the material.^[208–211] Other researchers have introduced an ionic conductor to the surface of classical layered oxides, such as, lithium lanthanum titanium oxides (LLTO),^[187,212–214] LiFePO_4 ,^[215,216] Li_3PO_4 ,^[217] and Li_3VO_4 .^[218] The results in Table 1 indicate that FePO_4 ,^[206] LLTO,^[213] and AlF_3 ^[199–203] are arguably the best coatings for improving the cycling stability of NMC at high voltages.

Achieving a uniform coating of the desired thickness remains a challenge. Wet chemistry methods are widely used to coat these surface modification materials on layered oxide powders; however, the coating conditions need to be optimized in each case to achieve a uniform coating layer. On the other

Table 1. Summary of different surface modifications and corresponding performance.

Coating	Composition (Ni:Mn:Co)	Voltage [V]	First cycle comparison (modified vs pristine)		Retention comparison (modified vs pristine)		Ref.
			Capacity [mA h g ⁻¹]	Rate	Retention	Rate	
Al ₂ O ₃	333	3–4.5	199 versus 196	30 mA g ⁻¹	93% versus 78.8%, 100 cyc	75 mA g ⁻¹	[194]
ZrO ₂	333	3–4.5	166 versus 168	30 mA g ⁻¹	99.1% versus 78.8%, 100 cyc	75 mA g ⁻¹	[188]
CeO ₂	333	2.8–4.5	162 versus 157	0.2C	100% versus 85.9%, 24 cyc	2C, 60 °C	[189]
CuO	532	3–4.6	180 versus 162	5C	89% versus 60%, 50 cyc 43% versus 39%, 50 cyc	5C, 3–4.6 V, 60 °C 1C, 3–4.8 V	[197]
TiO ₂	622	3–4.5	194 versus 188	28 mA g ⁻¹	88.7% versus 78.1%, 50 cyc	140 mA g ⁻¹	[219]
ZnO	532	2.5–4.5	238 versus 201	20 mA g ⁻¹	91.5% versus 87.4%, 60 cyc	400 mA g ⁻¹	[220]
Sb ₂ O ₃	333	3–4.6	170 versus 176	100 mA g ⁻¹	91.4% versus 73.5%, 100 cyc	100 mA g ⁻¹	[198]
AlF ₃	333	3–4.5	182 versus 182	16 mA g ⁻¹	93% versus 75%, 50 cyc 92% versus 72%, 50 cyc	80 mA g ⁻¹ , 3–4.5 V 80 mA g ⁻¹ , 3–4.6 V	[199]
(NH ₄) ₃ AlF ₆	333	2.7–4.5	192 versus 192	32 mA g ⁻¹	92% versus 76%, 70 cyc	80 mA g ⁻¹ , 55 °C	[221]
ZrFx	333	3–4.6	177 versus 170	1C	89.9% versus 86.4%, 100 cyc	1C, 3–4.3 V, 60 °C	[205]
LaF ₃ MgF ₂	532	3–4.6	190 versus 190	0.5C	89.8% versus 71.4%, 50 cyc	1C, 3–4.8 V	[222]
FeF ₃	333	3–4.8	210 versus 180	40 mA g ⁻¹	84% versus 57%, 50 cyc	40 mA g ⁻¹	[223]
LiAlO ₂	333	2.8–4.5	177 versus 174	0.2C	96.7% versus 82.3%, 50 cyc	0.5C	[224]
[Li,Li]TiO ₃	333	2.5–4.5	179 versus 171	40 mA g ⁻¹	89% versus 64%, 50 cyc	40 mA g ⁻¹	[214]
Li ₃ PO ₄	433	3–4.8	197 versus 196	1C	73.9% versus 64.1%, 50 cyc	1C	[217]
FePO ₄	532	2.5–4.6	213 versus 214	0.2C	91.2% versus 82.1%, 50 cyc	1C	[206]
Li ₃ VO ₄	532	3–4.8	180 versus 182	18 mA g ⁻¹	63% versus 41.5%–100 cyc	180 mA g ⁻¹	[218]
C	333	2.8–4.6	175 versus 162	1C	97.8% versus 85.3%, 100 cyc	1C	[211]
PEDOT	333	2.8–4.5	156 versus 168	150 mA g ⁻¹	85.9% versus 69.6%, 80 cyc	150 mA g ⁻¹	[225]
Rocksalt-like NMC	622	3–4.45	192 versus 192	0.1C	80% versus 65%, 150 cyc	1C, 60 °C	[226]

hand, atomic layer deposition (ALD) always provides a uniform coating layer with controllable thickness.^[190,196] The limiting factors of ALD are the limited chemical choices and difficulties in achieving large-scale production.

4.2. Bulk Substitution

Besides surface modifications, bulk substitutions with different elements have been applied to improve the electrochemical performance of layered oxides upon cycling. Bulk substitution can be divided into three categories: cation substitution (e.g., Mg,^[227–229] Fe,^[230] Al,^[228,230,231] Mo,^[232] V,^[233] Ti,^[234] and Cr^[228]); anion substitution (e.g., O substituted by F);^[235] and cation and anion co-substitution.^[236–240] **Table 2** summarizes bulk substitutions explored in NMC and NCA materials. However, some caution is required in the interpretation of experiments on doped battery materials: in some cases, the “dopant” is not incorporated into the bulk material but segregates out at grain boundaries, nanodomains, or other defects.

There are many mechanisms by which substitutions could potentially affect performance, and how these mechanisms play out for specific dopants is generally not well understood. First, some dopants may reinforce the structural stability of the layered phase by postponing stacking-sequence changes or mitigating the collapse of the interlayer spacing upon delithiation.

Second, the charge compensation of substitutions may influence electrochemical behavior. For example, replacing redox-active transition metals with inactive ions (e.g., Mg or Al) can also result in overcharge protection by preventing full delithiation.^[15] Furthermore, the charge required to balance aliovalent substitutions can modify the oxidation state of transition metals; for example, replacing Ni³⁺ with Mg²⁺ could be compensated by the oxidation of other Ni³⁺ sites to Ni⁴⁺.^[40] Lastly, substitutions can shift the voltage of transition metal redox couples by modifying the electronic structure of the material.^[40,83]

4.3. Morphology and Mesostucture Design

Morphology and mesostructure design, including particle size, shape, agglomeration, and transition-metal distribution, have a significant impact on electrochemical performance. For example, small dispersive particles can suffer from extensive surface side reactions.^[130,245] This problem can be solved by either synthesizing large (micrometer-sized) primary particles or designing mesostructured secondary spherical particles comprised of nanosized primary particles. However, large size primary particles can result in poor performance due to Li diffusion limitations. Also important is the tap density, which is controlled by the distribution of particle shapes and sizes. Generally compared with large primary particles with irregular

Table 2. Summary of different bulk substitutions and corresponding performance.

Element	Composition (Ni:Mn:Co)	Voltage [V]	First cycle comparison (modified vs pristine)		Retention comparison (modified vs pristine)		Ref.
			Capacity [mA h g ⁻¹]	Rate	Retention	Rate	
Si	333	2.75–4.5	180 versus 174	0.2C	94.7% versus 85.7%, 50 cyc	1C	[241]
Mg	333	2.8–4.4	176 versus 165	28 mA g ⁻¹	98% versus 95%, 30 cyc	28 mA g ⁻¹	[227]
Mg, F	442	2.8–4.6	187 versus 197	20 mA g ⁻¹	100% versus 92%, 50 cyc 97% versus 87%, 100 cyc	20 mA g ⁻¹ 170 mA g ⁻¹	[242]
Mg, Al, Cr	333	2.8–4.6	170 versus 173.3	32 mA g ⁻¹	97% versus 86.6%, 50 cyc for Cr	32 mA g ⁻¹	[228]
Mo	333	2.3–4.6	222 versus 180	20 mA g ⁻¹	83.9%, 50 cyc	20 mA g ⁻¹	[232]
F	333	3–4.6	177 versus 199	32 mA g ⁻¹	97.3% versus 83.5%, 30 cyc	32 mA g ⁻¹	[235]
Ti, F	333	2.6–4.4	168.8 versus 160.4	0.2C	96% versus 83.4%, 50 cyc	0.2C	[243]
Fe, Al	333	2.5–4.4	165 versus 172	0.1C	98% versus 92%, 40 cyc	0.1C	[230]
Al	811	3–4.5	160 versus 205	20 mA g ⁻¹	81% versus 73%, 30 cyc	20 mA g ⁻¹	[244]
V	532	2.7–4.4	192.6 versus 195.2	18 mA g ⁻¹	94% versus 94%, 50 cyc	18 mA g ⁻¹	[233]

shape, the designed mesostructure has higher density due to smaller quantity of space within the powders.^[246] Consequently, micrometer-sized secondary “meatball” particles comprised of 100–200 nm primary particles with homogeneous transition metal distribution is preferred in the morphology and mesostructured design of layered oxides. In this structure, small primary particles decrease lithium diffusion distance and the uniform secondary-particle size distribution increases tap density, which together enable excellent power and energy density.

Different synthetic routes have a distinct effect upon morphology and mesostructure. While there has been an exploration of solid-state,^[247] sol–gel, and hydro/solvothermal^[248,249] synthesis methods,^[250] the most common method for synthesizing layered-oxide electrode materials in both academia and industry is co-precipitation.^[251–253] Compared with other synthesis methods, it has many advantages: the formation of high tap density secondary particles with a narrow particle-size distribution; accurate stoichiometric proportions of transition metal precipitation; and lower synthesis temperature compared with solid-state method. However, the co-precipitation method is largely contingent on the careful control of different parameters including pH value, reaction time, reaction temperature, salt precursor concentration, stirring rate, and use of a gas purge. A systematic study is still in need for understanding the impact of these different control parameters on the morphology and mesostructure of materials synthesized via co-precipitation.

Hydro/solvothermal reactions are widely used for tailoring diverse particle morphologies. The extreme crystal growth conditions of high temperature and pressure allow for some degree of control over particle shape and homogeneity, as well as the exposure of specific crystallographic facets. For example, dumbbell-like NMC microspheres comprised of nanocubes were recently synthesized via a urea-assisted solvo/hydrothermal method.^[249] Experiments suggest that layered oxides produced by hydro/solvothermal synthesis could exhibit improved electrochemical performance.^[248,249]

Based on the spherical morphology designs for the secondary particle of classical layered oxides, researchers developed core–shell^[254] and gradient^[255,256] classical layered oxides.

Core–shell structures could be considered a conceptual extension of surface coatings. The coating layer is replaced with a Mn-rich cathode material which possesses better thermal and structural stability. Manipulating the core and shell with different components will make the performance of the core or the shell itself different from the performance of the new functional materials.^[257,258] However, the structural mismatch between the core and the shell can lead to void formation at the core/shell interface after long-term cycling, which deteriorates cycling stability.

Concentration-gradient structures, in which the concentration of transition metal is continuously varied from the bulk to the surface, can minimize the lattice parameter mismatch at the interface between the core and the shell.^[259,260] An example of the structure and electrochemical performance of a concentration-gradient NMC cathode material is shown in **Figure 23**.^[256] Figure 23b compares the electrochemical performance of full concentration-gradient (FCG) cores with different shells under severe test conditions. Shells with low nickel content resulted in improved capacity retention compared to the bare FCG core.

4.4. Li-Excess Layered Oxides

Lithium-excess layered oxides, Li_xM_{1-y}O₂ where 0 < x < 1 + y, have attracted substantial attention because of their ability to achieve capacities well beyond the classical layered oxides.^[41–43] These materials (sometimes referred to as Li-rich or Li-rich-Mn-rich), differ from the classical materials in that some Li resides in the transition-metal layer. At the atomic scale, these materials have been described as nanocomposites of layered Li(Li_{1/3}M'_{2/3})O₂ and layered LiMO₂ (with M' typically being Mn and M a mixture of Ni, Mn, and Co),^[261] or as single-phase solid solutions.^[262] To what extent these materials are better described by a two-phase nanocomposite or single-phase solid solution may depend on the specific composition of the material and synthesis conditions.^[41,42]

Remarkably, the Li-excess layered oxides can achieve reversible capacities beyond what would be expected from tradition

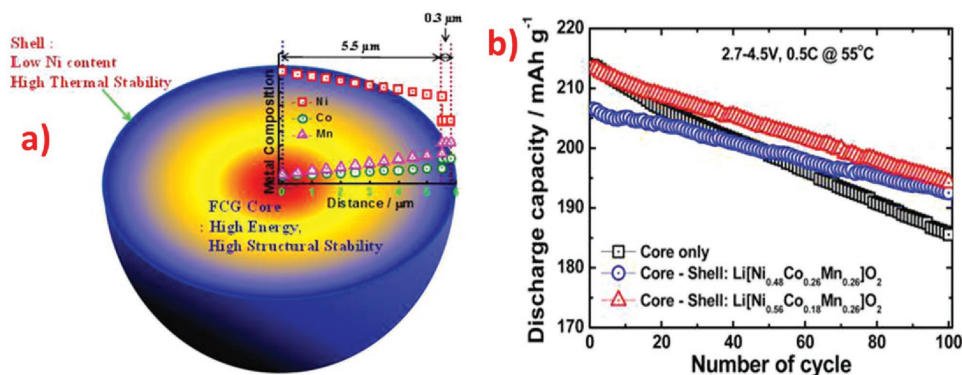


Figure 23. a) Schematic showing the mesostructure of a core-shell particle with a full concentration-gradient (FCG) core and thin shell with low nickel content. b) Discharge capacity versus cycle life for a FCG core with different shells under severe test conditions. Adapted with permission.^[256] Copyright 2014, American Chemical Society.

transition-metal redox chemistry. This anomalous capacity is accessible only after “activating” the material by charging to high voltages (≈ 4.6 V) at low rates; the role of this activation process is not well understood, although it has been suggested to result in a densification of the cathode material, wherein oxygen is lost at the surface and transition-metal cations diffuse back into the bulk.^[263,264] Reversible anion redox activity (i.e., the reduction and oxidation of oxygen) has been hypothesized to be the main source of anomalous capacity in Li-excess materials.^[265,267] One possible mechanism for anion redox activity is orphaned p states on oxygen atoms that are coordinated by a large number of Mn and Li atoms.^[265,266] Another is the formation of peroxy-like O_2^- species, especially in the 4d transition-metal oxides.^[267–269]

Despite the fact that Li-excess materials may exhibit reversible discharge capacities greater than 280 mA h g^{-1} , there are several inherent material issues that limit its practical application.^[41–43] First, the rate capability does not satisfy high-power applications. Second, severe voltage fade occurs after long cycles, which results in a significant decrease in energy density. These problems are thought to be linked to the migration of transition metal ions to octahedral and tetrahedral sites in the lithium layer.^[41–43]

4.5. High Voltage Electrolytes

Although this review focuses on the cathode materials, this section discusses the electrolyte because of its important role in cathode stability and surface reactions, especially at high voltages. In addition to stability against the cathode material, there are many other properties that an electrolyte must have in order to be effective in a battery, including high Li-ion conductivity and the formation of a stable SEI on the anode. High thermal stability and low flammability are also desirable for safety reasons.

Practical cells usually employ an organic liquid electrolyte (OLE) comprised of a mixed carbonate solvent, Li containing salts, and one or more additives. Solvent mixtures are designed to provide high Li-salt solubility, high Li^+ mobility, and stable anodic SEI formation. These mixtures often include ethylene carbonate (EC), dimethyl carbonate, diethyl carbonate, and

ethylmethyl carbonate.^[33] In fact, the ubiquity of EC in Li-ion batteries has led some to refer to it as the “new water.”^[270] LiPF₆ is commonly used as the salt, while additives such as vinyl carbonate and fluoroethylene carbonate are added in small amounts to modify the anodic SEI.^[33,271,272]

Much work has been done exploring new solvents, salts, and additives for OLEs,^[33,271] as well as ionic-liquid and polymer electrolytes.^[33] However, there are still many unanswered questions about how new liquid and polymer electrolytes interact with layered-oxide cathodes.^[34,130] Research tends to focus more on the graphitic SEI, and to a lesser extent the interaction of the electrolyte with high-voltage spinel cathodes.^[33,45,273] For example, the fluorination of organic solvents has been used as a strategy to improve electrolyte stability with respect to high-voltage cathodes.^[33,45,273]

Inorganic solid electrolytes represent an alternative to liquid and polymer electrolytes.^[35–39] Solid Li-ion conductors include perovskites such as $Li_3La_{2/3-y}TiO_3$ (LLTO),^[36,38] garnet oxides such as $Li_7La_3Zr_2O_{12}$ (LLZO),^[35] LiSICON-type phosphates,^[36,38] as well as sulfide solid electrolytes such as $Li_{10}GeP_2S_{12}$ (LGPS) and thio-LiSICON.^[37,274–276] Among all the solid electrolytes, the sulfide solid electrolytes show the highest conductivity at room temperature (10^{-3} – $10^{-2} \text{ S cm}^{-1}$).^[37,274–276] However, sulfide electrolytes are generally not stable against layered oxide cathodes or common anode materials.^[37,88,274,275] Some sulfide electrolytes appear to nevertheless be compatible with certain electrodes because the decomposition reactions at the interface are self-limiting and yield Li-ion conductive products, much like SEI formation with OLEs.^[37,275] Additionally, the use of coatings has been found to mitigate interfacial resistances between sulfide electrolytes and layered oxide cathodes.^[39]

4.6. Na and Other Intercalants

Many researchers have sought to electrochemically intercalate Na, rather than Li, in layered oxide and sulfide battery materials.^[7,8] Recently, the intercalation of other elements, such as Mg,^[277,278] has attracted attention as the battery community looks beyond lithium. While the science of these materials is extensive and beyond the scope of this review, this section seeks

to point out how the fundamental issues described in Section 2 play out differently for beyond-lithium chemistries.

Although Li and Na are both Group 1 elements, there are many important differences in their behavior during electrochemical intercalation. One obvious difference is that the mass of Na is three times greater than that of Li, resulting in a lower theoretical capacity. For example, Na_xCoO_2 has a theoretical capacity of 235 mA h g^{-1} , 14% smaller than that of Li_xCoO_2 (274 mA h g^{-1}). In addition to the larger mass of Na, there are several fundamental differences in intercalation chemistry of Li and Na that become apparent upon comparing the voltage curves obtained from Li_xCoO_2 and Na_xCoO_2 (Figure 24).

The first difference is that Na electrodes tend to have lower average voltages (vs Na/Na^+) than Li electrodes (vs Li/Li^+);^[280] this translates into a lower energy density. The higher voltage of Li intercalation is in line with the general notion that Li is a stronger reducing agent than Na, a fact that can be attributed to its smaller size: a shorter cation–anion distance results in a more negative electrostatic energy in Li compounds versus Na compounds.^[281] This ion-size effect is evidently strong enough to more than compensate for the fact that the 3s electrons of Na are less tightly bound than the 2s electrons of Li.

A second difference between Li and Na intercalation compounds is that intercalation in Na compounds generally occurs over a larger voltage window than in their Li analogues;^[76] in other words, the voltage curves for Na (de)intercalation are more steeply sloped. For example, Figure 24 shows that while essentially all of the capacity of Li_xCoO_2 can be accessed over a voltage window of $\approx 0.7 \text{ V}$, the voltage window of Na_xCoO_2 is at least 1.5 V . The larger voltage window required for (de)intercalation can be interpreted as a consequence of strong Na–Na repulsion due to the high electropositivity of sodium: the slope of the voltage curve is related to the curvature of the free-energy convex hull (see Section 2.3), and strong intercalant–intercalant repulsion results in a deeper hull.^[76] Having a more sloped voltage may reduce the practical energy density because cycling is typically performed only over $\approx 0.5 < x < 1$ to preserve cycle life.

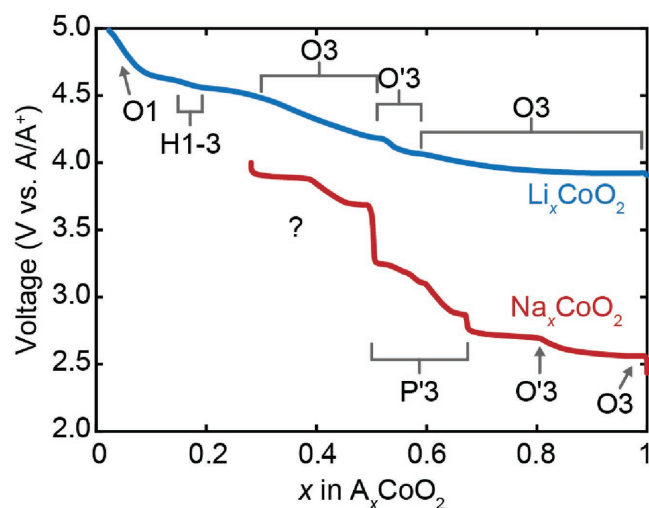


Figure 24. Comparison of voltage curves and stacking-sequence changes upon first charge for Li_xCoO_2 and Na_xCoO_2 .^[57,138,279]

A third difference between Li and Na intercalation chemistry is that phase transitions upon (de)intercalation are much more prevalent in Na compounds, which manifests in the voltage curve as a greater number of steps and bumps. In large part, this can be attributed to the fact that Na^+ ions, unlike Li^+ ions, are large enough to reside in prismatic coordination, making the P2 and P3 structures stable at intermediate compositions.^[7,8,76,282] For example, $\text{O}3 \text{ Na}_x\text{CoO}_2$ undergoes a first-order transformation to P'3 when deintercalated beyond $x \approx 0.8$,^[57] as shown in Figure 24. The prevalence of stacking sequences with prismatic coordination has several implications. First, the greater number of phase transformations in Na materials as compared to Li ones suggests that mechanical degradation may be a larger problem. Second, the honeycomb lattice of intercalant sites in P3 can result in complex sodium/vacancy ordering phenomena not seen in layered Li compounds.^[282] Lastly, ion transport may be very different in these prismatic-coordination materials because the migration mechanisms will be unlike those described in Section 2.4.1 for octahedral environments.^[8,282]

The larger ionic radius of Na^+ (1.16 \AA ^[283]) compared to Li^+ (0.90 \AA ^[283]) also has other effects besides the stabilization of prismatic structures. First, the strains associated with (de)intercalation of Na will be larger, potentially resulting in more rapid mechanical degradation. A second consequence of the larger size of Na^+ is that the greater discrepancy between the Na^+ radius and transition-metal radii results in a stronger tendency toward layering. Consequently, many layered sodium oxides are much easier to synthesize than their lithium analogues. The strong layering tendency of Na is in fact exploited for the synthesis of Li materials by performing Na^+/Li^+ ion exchange. This technique is what enabled the synthesis of well-layered LiMnO_2 ,^[60,158,159] and Na^+/Li^+ ion exchange has also been used to improve the layeredness of lithium nickel oxides.^[103]

The electrochemical (de)intercalation of magnesium has recently attracted renewed interest.^[278,284–286] Mg exhibits very different behavior than the (de)intercalation of Li and Na. Bulk diffusion and interfacial ion-transfer kinetics appear to be much slower for magnesium,^[277,287,288] and so some materials that are excellent for Li and Na batteries do not permit the electrochemical (de)intercalation of Mg. This may be in part due to strong interactions between the highly charged Mg^{2+} ions and anions in the host crystal and electrolyte.^[287,289] Nevertheless, reversible Mg (de)intercalation has been achieved in a few layered materials, such as MoS_2 ,^[285] WSe_2 ,^[285] and TiS_2 .^[278,288]

Relatively few studies have reported on the electrochemical (de)intercalation of elements beyond Li, Na, and Mg in layered materials. Recently, potassium (de)intercalation was reported in layered K_xMnO_2 ^[290,291] and aluminum (de)intercalation in layered Al_xTiS_2 .^[292] Many other analogues of classical Li-ion battery materials have been synthesized, such as K_xTiS_2 ,^[293] K_xCoO_2 ,^[294] and Ca_xCoO_2 ,^[295] however, we have not found reports of electrochemical studies on these materials.

4.7. Cation-Disordered Rocksalts

While conventional wisdom has held that the Li diffusion is quite slow in disordered rocksalts, some Li-excess disordered

rocksalts $\text{Li}_x\text{M}_{1-y}\text{O}_2$ can nevertheless be reversibly (de)intercalated. The disordered rocksalts are intimately related to the layered oxides: the anion sublattice is the same as O_3 , but the transition metal and intercalant cations are mixed, as discussed in Section 2.1. To the best of our knowledge, the study of $\text{Li}_3\text{V}_2\text{O}_5$ in the early 1990s was the first demonstration of reversible intercalation in a Li-excess disordered rocksalt.^[296,297] Recent interest in this class of materials, however, was spurred by the demonstration of a large reversible capacity in $\text{Li}_{1.21}\text{Mo}_{0.47}\text{Cr}_{0.3}\text{O}_2$ in 2014.^[110] Disordered-rocksalt materials could have some advantages over layered materials: transition-metal migration between layers would no longer be a concern, and smaller volume changes during (de)intercalation would reduce mechanical stress.

The key to enabling electrochemical activity in rocksalts is a Li-excess off-stoichiometric composition, $\gamma > 0$ in $\text{Li}_x\text{M}_{1-y}\text{O}_2$, which enables Li diffusion.^[110,298,299] Stoichiometric rocksalts, Li_xMO_2 , are generally electrochemically inactive because of large barriers for Li migration. The remarkable electrochemical activity of off-stoichiometric rocksalts has been attributed to the percolation of divacancy diffusion pathways wherein Li migrates through tetrahedral sites that share faces with other Li sites, but not transition-metal sites.^[110] Experiments and simulations have shown that these diffusion channels are able to access appreciable amounts of Li from $\text{Li}_{1+\gamma}\text{M}_{1-y}\text{O}_2$ only when γ is larger than ≈ 0.1 .^[110,298,299]

Although numerous cation-disordered rocksalts have now been found to exhibit large reversible capacities,^[299,300] these systems remain impractical because of the large polarization. The difference in voltage between charge and discharge is often as large as 0.5 to 1 V, even at low rates.^[110,296,297,299,300]

5. Recommended Best Practices

Although comparisons between different data sets are crucial to understanding the behavior of Li-ion battery materials, the inherent complexity of any experimental setup or computational framework makes such comparisons challenging. However, during our survey of prior literature, we found that certain techniques and conventions facilitated the comparison of data. Based on this experience, below are several suggestions for best practices for studying and reporting results related to layered oxide cathodes and other battery materials:

Reporting of parameters: The reporting of all relevant experimental parameters is crucial for allowing meaningful comparisons between studies. This is especially important for assessing the impacts of modifications on electrochemical performance, as in Tables 1 and 2. For example, some studies present current densities in terms of C-rate without indicating what convention is being used to define 1C in terms of mA g^{-1} . We suggest that the following battery testing conditions should be specified in publications that report electrochemistry data:

1. Battery type (e.g., coin cell 2016/2032 or Swagelok)
2. Electrode composition (weight percentage of active materials, binder and carbon)
3. Active-material loading mass (in mg cm^{-2})
4. Electrolyte type (lithium-salt concentration and solvent

composition)

5. Current density (mA g^{-1} or mA cm^{-2})

Although this list encompasses the most important experimental design parameters, it is by no means exhaustive. For example, material properties such as cathode particle morphology and amount of Ni in the Li layer, while difficult to measure quantitatively, can vary widely and strongly affect performance.

Beam damage: Partially delithiated oxides are highly sensitive to high-energy electron beams and X-rays. Adverse effects of beam exposure on layered oxides include electrostatic charging, heating, atomic displacement, structural damage, mass loss, etc.^[301] Under strong beam exposure, neutral oxygen atoms are created on the surface of layered oxides via the Knotek–Feibelman mechanism and ejected into the vacuum, leaving oxygen vacancies. Transition-metal cations consequently migrate to the Li layer to stabilize the structure, resulting in a similar phase reconstruction (from layered to defect spinel or even rocksalt) as induced by electrochemical cycles.^[302] To minimize or exclude beam-damage influence, experimental conditions, such as electron dose rate, dwell time, and temperature have to be carefully examined and reported when studying structural phase transformations.

Fixed-voltage cycling: Cycling over a fixed voltage range does not necessarily provide an apples-to-apples comparison between materials because the equilibrium voltage for intercalation varies substantially depending on the choice of transition metals and presence of dopants (cf. Figure 19). In fixed-voltage comparisons, differences in capacity retention, thermal stability, etc. arising from differing degrees of Li intercalation x can easily be misinterpreted as an effect of doping/alloying. The comparison of materials at fixed state of charge, rather than fixed voltage, can be helpful when trying to disentangle the direct effects of substitutions from the effects of the degree of Li intercalation.

Orientation of voltage curves: The orientation of voltage curves obtained from galvanostatic cycling can strongly impact the viewer's perception of the data. In particular, arranging axes such that charge and discharge proceed in opposite directions makes the voltage gap between charge and discharge readily visible; in contrast, arranging the axes instead with discharge and charge proceeding in the same direction obscures the difference in voltage.

Density-functional theory methods: Accurately capturing the physics of layered oxides is a nontrivial challenge for electronic-structure theory. First, van der Waals dispersion interactions play a crucial role in the interlayer interactions at low Li contents, and must be accounted for in order to correctly predict the collapse of the interlayer spacing upon deintercalation.^[288,303] Second, although the inclusion of on-site Hubbard corrections (i.e., DFT+ U) is often seen as a necessity for transition-metal oxides, it can sometimes lead to qualitatively incorrect predictions in layered oxides. For example, DFT+ U corrections derived from self-consistent calculations or the fitting of various properties (e.g., band gap) lead to an O_3 (rather than O_1) stacking-sequence in CoO_2 ,^[303] and also qualitatively incorrect phase diagrams for Li_xCoO_2 ^[304] and Na_xCoO_2 .^[305]

6. Conclusion

Enabling the reversible complete lithiation and delithiation of layered oxides could significantly improve the performance of Li-ion batteries in terms of capacity, energy density, and cost. One key barrier to achieving this is understanding and controlling the surface reactions that lead to the dissolution of transition-metal ions, the formation of an SEI-like surface film, and the reconstruction of surface layers to spinel/rocksalt. A second major issue is preventing and mitigating the consequences of mechanical damage to the electrode material. Mechanical damage will likely be more severe at high states of charge (low Li concentrations) because the rapid collapse of the interlayer spacing can lead to large internal strains. Finally, Li transport limitations may also become especially pronounced at high states of charge where Li diffusion coefficients decrease rapidly due the collapse of the interlayer spacing and an increased electrostatic repulsion between Li ions and the oxidized transition-metal cations. The rich interplay between transition metals (and dopants) causes these processes to play out quite differently depending on the cathode composition, providing opportunities to further improve the performance of layer transition metal oxides.

The above challenges (surface reactivity, mechanical degradation, and Li transport) are in a sense interdependent because of their sensitivity to particle morphology. In particular, small particle sizes tend to mitigate the effects of Li diffusion and mechanical degradation, while large particle sizes mitigate surface reactivity by reducing the surface-area-to-volume ratio. One example of this interdependence is Li_xFePO_4 : the success of this material has been attributed to its high resistance to surface reactions, which allows the particle size to be reduced enough to overcome sluggish lithium and electron transport.^[130]

Although much of the effort toward increasing the utilization of layered lithium oxides is focused on the high voltage region, one area for future research is the large irreversible capacity loss routinely seen on the first cycle.^[152,306] The origins of this capacity loss are not fully understood, but there are several possible contributing factors:

1. Loss of electrical connectivity to some cathode particles during the first cycle.
2. Irreversible surface reactions (such as reconstruction to spinel or rocksalt) that render a portion of the material electrochemically inactive.
3. The irreversible oxidation of Ni^{2+} in the Li layer to Ni^{3+} .^[152,153] This process has been suggested to be irreversible because the smaller size of Ni^{3+} would result in a local contraction of the interlayer spacing, inhibiting lithium reintercalation.
4. Classical diffusion limitations, either in the electrolyte or within cathode particles (cf. Section 2.4.1).
5. The generation of dislocations or other extended defects during the first cycle.
6. Consumption of current by parasitic oxidative processes (e.g., electrolyte oxidation) during the first charge.

In closing, we reflect on the inherently unstable nature of Li-ion batteries. Considering the reactivity of liquid and solid electrolytes with the anode and cathode, as well as the

thermodynamic driving forces for cation migration and oxygen loss in layered oxides, it is remarkable that Li-ion batteries function as well as they do. The success of the Li-ion chemistry is a consequence of the self-limiting nature of these side reactions, and the excellent Li-ion transport properties of their products. These reaction products include the anodic SEI, surface films present on the cathode, and the spinel/rocksalt reconstruction layers at the cathode surface. Therefore the philosophy of materials design for Li-ion batteries is not to find stable materials; rather, it is to find materials whose instabilities are self-limiting and benign.

Appendix

A: Derivation of Nernst Equation

Consider a system comprised of a cathode, anode, and electrolyte. The relevant internal degrees of freedom are:

- Number of Li^+ ions in cathode, $N_{\text{Li}^+}^c$
- Number of Li^+ ions in anode, $N_{\text{Li}^+}^a$
- Number of Li^+ ions in electrolyte, $N_{\text{Li}^+}^{\text{el}}$
- Number of valence electrons in cathode, N_e^c
- Number of valence electrons in anode, N_e^a

At open-circuit conditions, constraints arise from the total amount of Li^+ being fixed and the number of electrons in each electrode being fixed

$$\begin{aligned} N_{\text{Li}^+}^c + N_{\text{Li}^+}^a + N_{\text{Li}^+}^{\text{el}} &= N_1 \\ N_e^c &= N_2 \\ N_e^a &= N_3 \end{aligned} \quad (\text{A1})$$

Equilibrium at fixed temperature and pressure is given by the minimum of the Gibbs free energy $G(N_{\text{Li}^+}^c, N_{\text{Li}^+}^a, N_{\text{Li}^+}^{\text{el}}, N_e^c, N_e^a)$, subject to the above constraints. These constraints confine the system to a two-dimensional subspace of a five-dimensional vector space. At equilibrium, the derivative of G along any line in that two-dimensional subspace must be zero. Consider first the line corresponding to Li^+ exchange between cathode and anode: $dN_{\text{Li}^+}^c = -dN_{\text{Li}^+}^a$ and $dN_{\text{Li}^+}^{\text{el}} = dN_e^c = dN_e^a = 0$. For this process, the change in free energy is

$$dG = \frac{\partial G}{\partial N_{\text{Li}^+}^c} dN_{\text{Li}^+}^c + \frac{\partial G}{\partial N_{\text{Li}^+}^a} dN_{\text{Li}^+}^a = \left(\frac{\partial G}{\partial N_{\text{Li}^+}^c} - \frac{\partial G}{\partial N_{\text{Li}^+}^a} \right) dN_{\text{Li}^+}^c \quad (\text{A2})$$

At equilibrium, $dG = 0$ and so

$$\frac{\partial G}{\partial N_{\text{Li}^+}^c} - \frac{\partial G}{\partial N_{\text{Li}^+}^a} = 0 \quad (\text{A3})$$

Defining the electrochemical potential of species i in phase X as $\eta_i^X = \frac{\partial G}{\partial N_i^X}$, the above equation implies that $\eta_{\text{Li}^+}^c = \eta_{\text{Li}^+}^a$. Similarly, by considering Li^+ exchange with the electrolyte, one can show that $\eta_{\text{Li}^+}^c = \eta_{\text{Li}^+}^{\text{el}}$.

The voltage is defined as

$$V = -\frac{\eta_e^c - \eta_e^a}{e} \quad (\text{A4})$$

We will express the voltage in terms of the chemical potential of Li. To define this, we consider the Gibbs free energy as a function of the number of lithium atoms in each electrode $N_{\text{Li}}^x = N_{\text{Li}^+}^x$, and the net charge on each electrode $q^x = N_{\text{Li}^+}^x - N_e^x$: $G(N_{\text{Li}}^c, N_{\text{Li}}^a, N_{\text{Li}^+}^{\text{el}}, q^c, q^a)$. The chemical potential of Li in the cathode is then defined as $\mu_{\text{Li}}^c = \frac{\partial G}{\partial N_{\text{Li}}^c}$, where the derivative is understood to be at fixed N_{Li}^a , $N_{\text{Li}^+}^{\text{el}}$, q^c , and q^a ; the chemical potential of Li in the anode is defined analogously. One can see that $\mu_{\text{Li}}^x = \eta_e^x + \eta_{\text{Li}^+}^x$ by applying the chain rule, which (omitting terms that vanish) yields

$$\frac{\partial G^x}{\partial N_{\text{Li}}^x} = \frac{\partial G^x}{\partial N_{\text{Li}^+}^x} \frac{\partial N_{\text{Li}^+}^x}{\partial N_{\text{Li}}^x} + \frac{\partial G^x}{\partial N_e^x} \frac{\partial N_e^x}{\partial N_{\text{Li}}^x} = \eta_e^x + \eta_{\text{Li}^+}^x \quad (\text{A5})$$

Inserting $\eta_e^x = \mu_{\text{Li}}^x - \eta_{\text{Li}^+}^x$ into Equation (A4) yields

$$V = -\frac{(\mu_{\text{Li}}^c - \mu_{\text{Li}}^a) - (\eta_{\text{Li}^+}^c - \eta_{\text{Li}^+}^a)}{e} \quad (\text{A6})$$

At equilibrium $\eta_{\text{Li}^+}^c = \eta_{\text{Li}^+}^a$, and Equation (A6) reduces to the Nernst equation for Li-ion batteries:

$$V = -\frac{\mu_{\text{Li}}^c - \mu_{\text{Li}}^a}{e} \quad (\text{A7})$$

Equation (A6) also shows how the voltage deviates from the Nernstian value when the system is away from equilibrium (e.g., during charge or discharge). **Figure A1** illustrates qualitatively the difference in the electrochemical potential of Li⁺ ions at open circuit conditions versus during discharge. At open-circuit equilibrium, the electrochemical potential of Li⁺ ions is equal in all cell components as indicated by the dotted line, and the voltage takes its equilibrium value. When the cell is discharging, the electrochemical potential of Li⁺ is not equal throughout the cell. Discontinuities in η_{Li^+} across the anode/electrolyte and cathode/electrode interfaces are required in

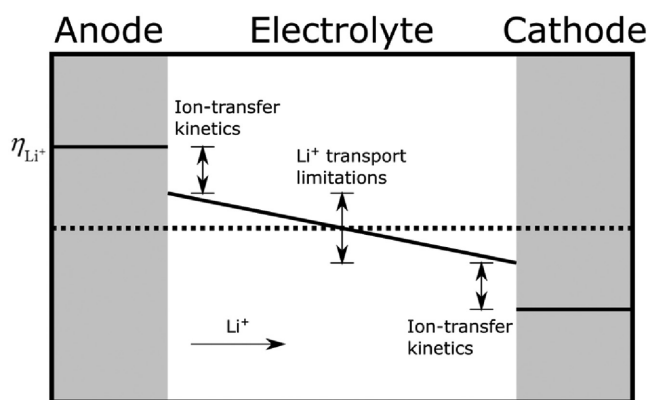


Figure A1. Schematic of lithium electrochemical at open-circuit conditions (dotted line) and during discharge (solid line).

order to drive ion-transfer, as discussed in Section 2.4.2. A gradient in η_{Li^+} across the electrolyte is similarly needed in order to drive Li⁺ transport, as discussed in Section 2.4.1. Although Figure A1 shows the electrochemical potential of Li⁺ as being constant within the electrodes, in practice transport limitations within the electrode materials will result in gradients in η_{Li^+} within the active material.

One can split electrochemical potential of species i in X into a chemical and electrostatic part: $\eta_i^x = \mu_i^x + q_i \phi^x$. Here μ_i^x is the chemical component, q_i is the charge of species i , and ϕ^x is the macroscopic electrostatic potential in X . The division of electrochemical potential into chemical and electrostatic components is arbitrary;^[92] one can add constants to ϕ^x and μ_i^x such that η_i^x remains unchanged. As a result, it is not strictly speaking meaningful to compare the macroscopic electrostatic potentials between regions with different compositions or structures. However, the difference in potential differences entering the Butler–Volmer equation (Equation (7)), $\Delta\phi - \Delta\phi^{\text{eq}}$, is uniquely defined. Furthermore, in the context of estimating relative equilibrium voltages of different materials (cf. Section 2.3), it is useful to choose $\phi^x = 0$ to correspond to some sensible reference state, e.g., having no net charge. With such a choice of references, one can make qualitative inferences about the relative values of μ_i^x in different materials using chemical intuition, as discussed in Section 2.3.

B: Transport Model

We consider the ideal diffusion of an ideal intercalant in a cylindrical particle of radius R with an intercalant site concentration of c_0 . Initially, the particle is fully deintercalated, and then subject to a current density of J_0 on its surface. Given the cylindrical symmetry of the problem, the concentration $c(r, t)$ at radius r and time t satisfies the governing equation

$$\frac{\partial c}{\partial t} = \frac{D}{r} \frac{\partial}{\partial r} \left[r \frac{\partial c}{\partial r} \right] \quad (\text{B1})$$

with boundary condition $J_0 = -D \left(\frac{\partial c}{\partial r} \right)_{r=R}$ and initial condition $c(r, 0) = 0$. Neglecting ion-transfer kinetics and diffusion limitation in the electrolyte, the electrochemical potential of Li⁺ at the particle surface is in equilibrium with the anode. Therefore, from the analysis in Appendix A, the voltage across the battery is determined by the difference in chemical potential between the surface of the cathode particle and the anode: $V(t) = -[\mu_{\text{Li}}^{\text{cat}}(c(R, t)) - \mu_{\text{Li}}^{\text{an}}] / e$. Assuming the cathode to have ideal intercalation thermodynamics, the chemical potential of lithium in the cathode can be expressed as

$$\mu_{\text{Li}}^{\text{cat}}(c) = k_B T \ln \frac{c/c_0}{1 - c/c_0} \quad (\text{B2})$$

This model can be expressed in a dimensionless form

$$\frac{\partial x}{\partial \tau} = \frac{1}{\rho} \frac{\partial}{\partial \rho} \left(\rho \frac{\partial x}{\partial \rho} \right) \quad (\text{B3})$$

where $x = c/c_0$, $\tau = Dt/R^2$, and $\rho = r/R$. The boundary condition is $j_0 = -\left(\frac{\partial x}{\partial \rho}\right)_{\rho=1}$ where $j_0 = J_0R/c_0D$ is the dimensionless current density, and the initial condition is $x(\rho,0) = 0$. The dimensionless voltage

$$\Phi(\tau) = \frac{eV(t) - \mu_{Li}^{an}}{k_B T} \quad (B4)$$

is given by $\Phi(\tau) = -\ln \frac{x(1,\tau)}{1-x(1,\tau)}$.

Acknowledgements

This material is based upon work supported as part of the Northeastern Center for Chemical Energy Storage (NECCES), an Energy Frontier Research Center funded by the U.S. Department of Energy, Office of Science, Office of Basic Energy Sciences under Award Number DE-SC0012583. M.D.R. gratefully acknowledges G. Amatucci and R. Kostecki for valuable discussion.

Conflict of Interest

The authors declare no conflict of interest.

Keywords

energy storage, layered oxides, Li-ion batteries, phase transformations

Received: December 23, 2016

Revised: March 18, 2017

Published online:

- [1] S. Chu, A. Majumdar, *Nature* **2012**, 488, 294.
- [2] *Quadrennial Technology Review: An Assessment of Energy Technologies and Research Opportunities* **2015**.
- [3] N. Imanishi, A. C. Luntz, P. Bruce, *The Lithium Air Battery: Fundamentals*, Springer, NY **2014**.
- [4] M. D. Radin, D. J. Siegel, in *Rechargeable Batteries: Materials, Technologies and New Trends* (Eds.: Z. Zhang, S. S. Zhang), Springer International Publishing **2015**, Cham, Switzerland.
- [5] L. F. Nazar, M. Cuisinier, Q. Pang, *MRS Bull.* **2014**, 39, 436.
- [6] A. Manthiram, Y. Fu, S. Chung, C. Zu, Y. Su, *Chem. Rev.* **2014**, 114, 11751.
- [7] M. H. Han, E. Gonzalo, G. Singh, T. Rojo, *Energy Environ. Sci.* **2015**, 8, 81.
- [8] N. Yabuuchi, K. Kubota, M. Dahbi, S. Komaba, *Chem. Rev.* **2014**, 114, 11636.
- [9] H. D. Yoo, I. Shterenberg, Y. Gofer, G. Gershinsky, N. Pour, D. Aurbach, *Energy Environ. Sci.* **2013**, 6, 2265.
- [10] M. S. Whittingham, *Chem. Rev.* **2014**, 114, 11414.
- [11] K. G. Gallagher, S. Goebel, T. Greszler, M. Mathias, W. Oelrich, D. Eroglu, V. Srinivasan, *Energy Environ. Sci.* **2014**, 7, 1555.
- [12] M. S. Whittingham, *Chem. Rev.* **2004**, 104, 4271.
- [13] N. Nitta, F. Wu, J. T. Lee, G. Yushin, *Mater. Today* **2015**, 18, 252.
- [14] V. Etacheri, R. Marom, R. Elazari, G. Salitra, D. Aurbach, *Energy Environ. Sci.* **2011**, 4, 3243.
- [15] T. Ohzuku, T. Yanagawa, M. Kouguchi, A. Ueda, *J. Power Sources* **1997**, 68, 131.
- [16] S. Madhavi, G. V. Subba Rao, B. V. R. Chowdari, S. F. Y. Li, *J. Power Sources* **2001**, 93, 156.
- [17] Z. Lu, D. D. MacNeil, J. R. Dahn, *Electrochem. Solid-State Lett.* **2001**, 4, A200.
- [18] M. Yoshio, H. Noguchi, J. ichi Itoh, M. Okada, T. Mouri, *J. Power Sources* **2000**, 90, 176.
- [19] T. Ohzuku, Y. Makimura, *Chem. Lett.* **2001**, 30, 642.
- [20] Z. Liu, A. Yu, J. Y. Lee, *J. Power Sources* **1999**, 81–82, 416.
- [21] G. Crabtree, E. Kócs, L. Trahey, *MRS Bull.* **2015**, 40, 1067.
- [22] E. M. Erickson, C. Ghanty, D. Aurbach, *J. Phys. Chem. Lett.* **2014**, 5, 3313.
- [23] J. B. Goodenough, Y. Kim, *Chem. Mater.* **2010**, 22, 587.
- [24] D. Andre, S.-J. Kim, P. Lamp, S. F. Lux, F. Maglia, O. Paschos, B. Stiaszny, *J. Mater. Chem. A* **2015**, 3, 6709.
- [25] M. M. Thackeray, C. Wolverton, E. D. Isaacs, *Energy Environ. Sci.* **2012**, 5, 7854.
- [26] B. L. Ellis, K. T. Lee, L. F. Nazar, *Chem. Mater.* **2010**, 22, 691.
- [27] R. Hausbrand, G. Cherkashinin, H. Ehrenberg, M. Gröting, K. Albe, C. Hess, W. Jaegermann, *Mater. Sci. Eng. B* **2015**, 192, 3.
- [28] N. A. Chernova, G. M. Nolis, F. O. Omenya, H. Zhou, Z. Li, M. S. Whittingham, *J. Mater. Chem.* **2011**, 21, 9865.
- [29] G. Ceder, G. Hautier, A. Jain, S. P. Ong, *MRS Bull.* **2011**, 36, 185.
- [30] M. S. Islam, C. A. J. Fisher, *Chem. Soc. Rev.* **2014**, 43, 185.
- [31] O. Borodin, in *Electrolytes for Lithium and Lithium-Ion Batteries*. (Eds.: T. R. Jow, K. Xu, O. Borodin, M. Ue), Springer, NY **2014**.
- [32] K. Xu, A. von Cresce, *J. Mater. Chem.* **2011**, 21, 9849.
- [33] K. Xu, *Chem. Rev.* **2014**, 114, 11503.
- [34] D. Aurbach, B. Markovsky, G. Salitra, E. Markevich, Y. Talyossef, M. Koltypin, L. Nazar, B. Ellis, D. Kovacheva, *J. Power Sources* **2007**, 165, 491.
- [35] V. Thangadurai, S. Narayanan, D. Pinzaru, *Chem. Soc. Rev.* **2014**, 43, 4714.
- [36] J. W. Fergus, *J. Power Sources* **2010**, 195, 4554.
- [37] Y. S. Jung, D. Y. Oh, Y. J. Nam, K. H. Park, *Isr. J. Chem.* **2015**, 55, 472.
- [38] P. Knauth, *Solid State Ionics* **2009**, 180, 911.
- [39] K. Okada, N. Machida, M. Naito, T. Shigematsu, S. Ito, S. Fujiki, M. Nakano, Y. Aihara, *Solid State Ionics* **2014**, 255, 120.
- [40] C. Delmas, M. Ménétrier, L. Croguennec, I. Saadoune, A. Rougier, C. Poullierie, G. Prado, M. Grune, L. Fournès, *Electrochim. Acta* **1999**, 45, 243.
- [41] S. Hy, H. Liu, D. Qian, M. Zhang, B. J. Hwang, Y. S. Meng, *Energy Environ. Sci.* **2016**, 9, 1931.
- [42] J. Hong, H. Gwon, S.-K. Jung, K. Ku, K. Kang, *J. Electrochem. Soc.* **2015**, 162, A2447.
- [43] P. Rozier, J. M. Tarascon, *J. Electrochem. Soc.* **2015**, 162, A2490.
- [44] R. Malik, A. Abdellahi, G. Ceder, *J. Electrochem. Soc.* **2013**, 160, A3179.
- [45] A. Manthiram, K. Chemelewski, E.-S. Lee, *Energy Environ. Sci.* **2014**, 7, 1339.
- [46] A. Kraysberg, Y. Ein-Eli, *Adv. Energy Mater.* **2012**, 2, 922.
- [47] W. Xu, J. Wang, F. Ding, X. Chen, E. Nasybulin, Y. Zhang, J.-G. Zhang, *Energy Environ. Sci.* **2014**, 7, 513.
- [48] J. B. Goodenough, *J. Power Sources* **2007**, 174, 996.
- [49] C. Delmas, C. Fouassier, P. Hagenmuller, *Phys. B+C* **1980**, 99, 81.
- [50] H. Ben Yahia, M. Shikano, H. Kobayashi, *Chem. Mater.* **2013**, 25, 3687.
- [51] C. Delmas, J.-J. Braconnier, P. Hagenmuller, *Mater. Res. Bull.* **1982**, 17, 117.
- [52] A. Van der Ven, M. K. Aydinol, G. Ceder, G. Kresse, J. Hafner, *Phys. Rev. B* **1998**, 58, 2975.
- [53] A. Van der Ven, M. K. Aydinol, G. Ceder, *J. Electrochem. Soc.* **1998**, 145, 2149.
- [54] Z. Chen, Z. Lu, J. R. Dahn, *J. Electrochem. Soc.* **2002**, 149, A1604.

- [55] A. Mendiboune, C. Delmas, P. Hagenmuller, *Mater. Res. Bull.* **1984**, 19, 1383.
- [56] D. Carlier, A. Van der Ven, C. Delmas, G. Ceder, *Chem. Mater.* **2003**, 15, 2651.
- [57] C. Delmas, J. Braconnier, C. Fouassier, P. Hagenmuller, *Solid State Ionics* **1981**, 3–4, 165.
- [58] C. Marianetti, D. Morgan, G. Ceder, *Phys. Rev. B* **2001**, 63, 1.
- [59] J. N. Reimers, J. R. Dahn, *J. Electrochem. Soc.* **1992**, 139, 2091.
- [60] M. M. Thackeray, *Prog. Solid State Chem.* **1997**, 25, 1.
- [61] A. Van der Ven, G. Ceder, *Phys. Rev. B* **1999**, 59, 742.
- [62] J. Bhattacharya, A. Van Der Ven, *Phys. Rev. B* **2010**, 81, 104304.
- [63] G. Ceder, A. Van der Ven, *Electrochim. Acta* **1999**, 45, 131.
- [64] C. Wolverton, A. Zunger, *J. Electrochem. Soc.* **1998**, 145, 2424.
- [65] L. Wang, T. Maxisch, G. Ceder, *Chem. Mater.* **2007**, 19, 543.
- [66] J. Reed, G. Ceder, *Chem. Rev.* **2004**, 104, 4513.
- [67] J. Reed, G. Ceder, A. Van der Ven, *Electrochem. Solid-State Lett.* **2001**, 4, A78.
- [68] M. Ménétrier, I. Saadoune, S. Levasseur, C. Delmas, *J. Mater. Chem.* **1999**, 9, 1135.
- [69] C. A. Marianetti, G. Kotliar, G. Ceder, *Nat. Mater.* **2004**, 3, 627.
- [70] A. Milewska, K. Swierczek, J. Tobola, F. Boudoire, Y. Hu, D. K. Bora, B. S. Mun, A. Braun, J. Molenda, *Solid State Ionics* **2014**, 263, 110.
- [71] M. Wagemaker, A. Van der Ven, D. Morgan, G. Ceder, F. M. Mulder, G. J. Kearley, *Chem. Phys.* **2005**, 317, 130.
- [72] M. Arroyo y de Dompablo, A. Van der Ven, G. Ceder, *Phys. Rev. B* **2002**, 66, 064112.
- [73] C. Delmas, M. Ménétrier, L. Croguennec, S. Levasseur, J. P. Pèrès, C. Pouillier, G. Prado, L. Fournès, F. Weill, *Int. J. Inorg. Mater.* **1999**, 1, 11.
- [74] A. Van der Ven, C. Marianetti, D. Morgan, G. Ceder, *Solid State Ionics* **2000**, 135, 21.
- [75] L. Croguennec, C. Pouillier, C. Delmas, *J. Electrochem. Soc.* **2000**, 147, 1314.
- [76] M. D. Radin, A. Van der Ven, *Chem. Mater.* **2016**, 28, 7898.
- [77] L. Croguennec, C. Pouillier, a. N. Mansour, C. Delmas, *J. Mater. Chem.* **2001**, 11, 131.
- [78] J. Hertz, Q. Huang, T. McQueen, T. Klimczuk, J. Bos, L. Viciu, R. Cava, *Phys. Rev. B* **2008**, 77, 75119.
- [79] B. J. Hwang, Y. W. Tsai, D. Carlier, G. Ceder, *Chem. Mater.* **2003**, 15, 3676.
- [80] I. Saadoune, M. Ménétrier, C. Delmas, *J. Mater. Chem.* **1997**, 7, 2505.
- [81] M. K. Aydinol, A. F. Kohan, G. Ceder, K. Cho, J. Joannopoulos, *Phys. Rev. B* **1997**, 56, 1354.
- [82] C. Wolverton, A. Zunger, *Phys. Rev. Lett.* **1998**, 81, 606.
- [83] G. Ceder, Y. M. Chiang, D. R. Sadoway, M. K. Aydinol, Y. I. Jang, B. Huang, *Nature* **1998**, 392, 694.
- [84] J. Molenda, J. Wilk, P. Marzec, *Solid State Ionics* **2002**, 146, 73.
- [85] I. Saadoune, C. Delmas, *J. Solid State Chem.* **1998**, 15, 8.
- [86] R. Amin, D. B. Ravnsbæk, Y.-M. Chiang, *J. Electrochem. Soc.* **2015**, 162, A1163.
- [87] J. B. Goodenough, *J. Solid State Electrochem.* **2012**, 16, 2019.
- [88] W. D. Richards, L. J. Miara, Y. Wang, J. C. Kim, G. Ceder, *Chem. Mater.* **2016**, 28, 266.
- [89] A. Yu, V. Chabot, J. Zhang, *Electrochemical Supercapacitors for Energy Storage and Delivery Fundamentals and Applications*, Taylor & Francis, Boca Raton, FL **2013**.
- [90] V. Augustyn, P. Simon, B. Dunn, *Energy Environ. Sci.* **2014**, 7, 1597.
- [91] A. Van der Ven, J. Bhattacharya, A. A. Belak, *Acc. Chem. Res.* **2013**, 46, 1216.
- [92] J. S. Newman, K. E. Thomas-Alyea, *Electrochemical Systems*, J. Wiley, Hoboken, NJ **2004**.
- [93] R. Gomer, *Rep. Prog. Phys.* **1990**, 53, 917.
- [94] R. Kutner, *Phys. Lett. A* **1981**, 81, 239.
- [95] A. Van der Ven, G. Ceder, *Electrochem. Solid-State Lett.* **2000**, 3, 301.
- [96] A. Van der Ven, G. Ceder, *J. Power Sources* **2001**, 97–98, 529.
- [97] A. Van der Ven, G. Ceder, M. Asta, P. Tepeesch, *Phys. Rev. B* **2001**, 64, 184307.
- [98] A. Van der Ven, J. C. Thomas, Q. Xu, B. Swoboda, D. Morgan, *Phys. Rev. B* **2008**, 78, 104306.
- [99] J. Bhattacharya, A. Van der Ven, *Phys. Rev. B* **2011**, 83, 144302.
- [100] Y.-I. Jang, B. J. Neudecker, N. J. Dudney, *Electrochem. Solid-State Lett.* **2001**, 4, A74.
- [101] H. Xia, Y. S. Meng, L. Lu, G. Ceder, <http://hdl.handle.net/1721.1/35827> (accessed: December 2016, Electrochemical Behavior and Li Diffusion Study of LiCoO₂ Thin Film Electrodes Prepared by PLD).
- [102] K. Kang, G. Ceder, *Phys. Rev. B* **2006**, 74, 94105.
- [103] K. Kang, Y. S. Meng, J. Bréger, C. P. Grey, G. Ceder, *Science* **2006**, 311, 977.
- [104] Y. M. Choi, S. Il Pyun, J. S. Bae, S. I. Moon, *J. Power Sources* **1995**, 56, 25.
- [105] K. Nakamura, H. Ohno, K. Okamura, Y. Michihiro, I. Nakabayashi, T. Kanashiro, *Solid State Ionics* **2000**, 135, 143.
- [106] P. G. Bruce, M. Y. Saidi, *Solid State Ionics* **1992**, 57, 353.
- [107] R. Amin, Y.-M. Chiang, *J. Electrochem. Soc.* **2016**, 163, A1512.
- [108] S.-L. Wu, W. Zhang, X. Song, A. K. Shukla, G. Liu, V. Battaglia, V. Srinivasan, *J. Electrochem. Soc.* **2012**, 159, A438.
- [109] B. Xu, S. Meng, *J. Power Sources* **2010**, 195, 4971.
- [110] J. Lee, A. Urban, X. Li, D. Su, G. Hautier, G. Ceder, *Science* **2014**, 343, 519.
- [111] H. Moriwake, A. Kuwabara, C. A. J. Fisher, R. Huang, T. Hitosugi, Y. H. Ikuhara, H. Oki, Y. Ikuhara, *Adv. Mater.* **2013**, 25, 618.
- [112] M. Doyle, T. F. Fuller, J. Newman, *J. Electrochem. Soc.* **1993**, 140, 1526.
- [113] K. Dokko, M. Mohamedi, Y. Fujita, T. Itoh, M. Nishizawa, M. Umeda, I. Uchida, *J. Electrochem. Soc.* **2001**, 148, A422.
- [114] B. Garcia, J. Farcy, J. P. Pereira-Ramos, *J. Electrochem. Soc.* **1997**, 144, 1179.
- [115] D. Kramer, G. Ceder, *Chem. Mater.* **2009**, 21, 3799.
- [116] P. J. Bouwman, B. A. Boukamp, H. J. M. Bouwmeester, P. H. L. Notten, *J. Electrochem. Soc.* **2002**, 149, A699.
- [117] K. Xu, A. Von Cresce, U. Lee, **2010**, 26, 11538.
- [118] A. Van der Ven, K. Garikipati, S. Kim, M. Wagemaker, *J. Electrochem. Soc.* **2009**, 156, A949.
- [119] R. Malik, F. Zhou, G. Ceder, *Nat. Mater.* **2011**, 10, 587.
- [120] D. Chang, H. Huo, K. E. Johnston, M. Ménétrier, L. Monconduit, C. P. Grey, A. Van der Ven, *J. Mater. Chem. A* **2015**, 3, 18928.
- [121] M. Wagemaker, F. M. Mulder, A. Van Der Ven, *Adv. Mater.* **2009**, 21, 2703.
- [122] J. W. Cahn, *Acta Metall.* **1962**, 10, 907.
- [123] J. W. Cahn, *Acta Metall.* **1961**, 9, 795.
- [124] L.-Q. Chen, *Annu. Rev. Mater. Res.* **2002**, 32, 113.
- [125] H. Gabrisch, R. Yazami, B. Fultz, *Electrochem. Solid-State Lett.* **2002**, 5, A111.
- [126] F. Lin, I. M. Markus, D. Nordlund, T.-C. Weng, M. D. Asta, H. L. Xin, M. M. Doeff, *Nat. Commun.* **2014**, 5, 3529.
- [127] Y. Shao-Horn, S. A. Hackney, A. R. Armstrong, P. G. Bruce, R. Gitzendanner, C. S. Johnson, M. M. Thackeray, *J. Electrochem. Soc.* **1999**, 146, 2404.
- [128] G. Vitins, K. West, *J. Electrochem. Soc.* **1997**, 144, 2587.
- [129] K. Karki, Y. Huang, S. Hwang, A. D. Gamalski, M. S. Whittingham, G. Zhou, E. A. Stach, *ACS Appl. Mater. Interfaces* **2016**, 8, 27762.
- [130] S. F. Amalraj, R. Sharabi, H. Sclar, D. Aurbach, in *Electrolytes for Lithium and Lithium-Ion Batteries*. (Eds.: M. U. T. Richard Jow, K. Xu, O. Borodin), Springer, NY, **2014**, pp. 283–321.
- [131] J. C. Hunter, *J. Solid State Chem.* **1981**, 39, 142.

- [132] A. Jarry, S. Gottis, Y. S. Yu, J. Roque-Rosell, C. Kim, J. Cabana, J. Kerr, R. Kostecki, *J. Am. Chem. Soc.* **2015**, *137*, 3533.
- [133] N. Kumar, K. Leung, D. J. Siegel, *J. Electrochem. Soc.* **2014**, *161*, E3059.
- [134] A. Mukhopadhyay, B. W. Sheldon, *Prog. Mater. Sci.* **2014**, *63*, 58.
- [135] D. J. Miller, C. Proff, J. G. Wen, D. P. Abraham, J. Bareño, *Adv. Energy Mater.* **2013**, *3*, 1098.
- [136] S. Zheng, R. Huang, Y. Makimura, Y. Ukyo, C. A. J. Fisher, T. Hirayama, Y. Ikuhara, *J. Electrochem. Soc.* **2011**, *158*, A357.
- [137] W. H. Woodford, Y.-M. Chiang, W. C. Carter, *J. Electrochem. Soc.* **2010**, *157*, A1052.
- [138] Z. Chen, J. R. Dahn, *Electrochim. Acta* **2004**, *49*, 1079.
- [139] G. G. Amatucci, J. M. Tarascon, L. C. Klein, *Electrochem. Soc.* **1996**, *143*, 1114.
- [140] W. Li, J. N. Reimers, J. R. Dahn, **1993**, *67*, 123.
- [141] K. Mizushima, P. C. Jones, P. J. Wiseman, J. B. Goodenough, *Solid State Ionics* **1981**, *3–4*, 171.
- [142] H. Wang, Y. Jang, B. Huang, D. R. Sadoway, Y. Chiang, *J. Electrochem. Soc.* **1999**, *146*, 473.
- [143] R. Yazami, Y. Ozawa, H. Gabrisch, B. Fultz, *Electrochim. Acta* **2004**, *50*, 385.
- [144] H. Wang, Y.-I. Jang, B. Huang, D. R. Sadoway, Y.-M. Chiang, *J. Power Sources* **1999**, *81–82*, 594.
- [145] A. Yano, M. Shikano, A. Ueda, H. Sakaebe, Z. Ogumi, *J. Electrochem. Soc.* **2017**, *164*, A6116.
- [146] W. H. Woodford, W. C. Carter, Y.-M. Chiang, *Energy Environ. Sci.* **2012**, *5*, 8014.
- [147] Z. Chen, Z. Lu, J. R. Dahn, *J. Electrochem. Soc.* **2002**, *149*, A1604.
- [148] T. Ohzuku, A. Ueda, M. Nagayama, **1993**, *140*, 1862.
- [149] T. Ohzuku, A. Ueda, *J. Electrochem. Soc.* **1994**, *141*, 2972.
- [150] K. Edström, T. Gustafsson, J. O. Thomas, *Electrochim. Acta* **2004**, *50*, 397.
- [151] J. Vetter, P. Novák, M. R. Wagner, C. Veit, K. C. Möller, J. O. Besenhard, M. Winter, M. Wohlfahrt-Mehrens, C. Vogler, A. Hammouche, *J. Power Sources* **2005**, *147*, 269.
- [152] C. Delmas, J. P. Pérès, A. Rougier, A. Demourgues, F. Weill, A. Chadwick, M. Broussely, F. Pertion, P. Biensan, P. Willmann, *J. Power Sources* **1997**, *68*, 120.
- [153] J. P. Pérès, C. Delmas, A. Rougier, M. Broussely, F. Pertion, P. Biensan, P. Willmann, *J. Phys. Chem. Solids* **1996**, *57*, 1057.
- [154] A. Rougier, C. Delmas, A. V. Chadwick, *Solid State Commun.* **1995**, *94*, 123.
- [155] J. H. Chung, T. Proffen, S. Shamoto, A. M. Ghorayeb, L. Croguennec, W. Tian, B. C. Sales, R. Jin, D. Mandrus, T. Egami, *Phys. Rev. B* **2005**, *71*, 064410.
- [156] Z. Chen, H. Zou, X. Zhu, J. Zou, J. Cao, *J. Solid State Chem.* **2011**, *184*, 1784.
- [157] H. Chen, C. L. Freeman, J. H. Harding, *Phys. Rev. B* **2011**, *84*, 085108.
- [158] F. Capitaine, P. Gravereau, C. Delmas, *Solid State Ionics* **1996**, *89*, 197.
- [159] A. R. Armstrong, P. G. Bruce, *Nature* **1996**, *381*, 499.
- [160] W. Choi, A. Manthiram, *J. Electrochem. Soc.* **2006**, *153*, A1760.
- [161] Y. Makimura, T. Sasaki, T. Nonaka, Y. F. Nishimura, T. Uyama, C. Okuda, Y. Itou, Y. Takeuchi, *J. Mater. Chem. A* **2016**, *4*, 8350.
- [162] Y.-Q. Lai, M. Xu, Z.-A. Zhang, C.-H. Gao, P. Wang, Z.-Y. Yu, *J. Power Sources* **2016**, *309*, 20.
- [163] K. Hoang, M. Johannes, *Chem. Mater.* **2016**, *28*, 1325.
- [164] T. Sasaki, T. Nonaka, H. Oka, C. Okuda, Y. Itou, Y. Kondo, Y. Takeuchi, Y. Ukyo, K. Tatsumi, S. Muto, *J. Electrochem. Soc.* **2009**, *156*, A289.
- [165] R. Robert, C. Bünzli, E. J. Berg, P. Novák, *Chem. Mater.* **2015**, *27*, 526.
- [166] A. Rougier, I. Saadoune, P. Gravereau, P. Willmann, C. Delmas, *Solid State Ionics* **1996**, *90*, 83.
- [167] C. H. Chen, J. Liu, M. E. Stoll, G. Henriksen, D. R. Vissers, K. Amine, *J. Power Sources* **2004**, *128*, 278.
- [168] T. Ohzuku, A. Ueda, M. Kouguchi, *J. Electrochem. Soc.* **1995**, *142*, 4033.
- [169] M. Guilnard, L. Croguennec, D. Denux, C. Delmas, *Chem. Mater.* **2003**, *15*, 4476.
- [170] M. Guilnard, L. Croguennec, C. Delmas, *Chem. Mater.* **2003**, *15*, 4484.
- [171] L. Croguennec, Y. Shao-Horn, A. Gloter, C. Colliex, M. Guilnard, F. Fauth, C. Delmas, *Chem. Mater.* **2009**, *21*, 1051.
- [172] N. M. Trease, I. D. Seymour, M. D. Radin, H. Liu, S. Hy, N. Chernova, P. Parikh, A. Devaraj, K. M. Wiaderek, P. J. Chupas, K. W. Chapman, M. S. Whittingham, Y. S. Meng, A. Van der Ven, C. P. Grey, *Chem. Mater.* **2016**, *28*, 8170.
- [173] S. Hwang, W. Chang, S. M. Kim, D. Su, D. H. Kim, J. Y. Lee, K. Y. Chung, E. A. Stach, *Chem. Mater.* **2014**, *26*, 1084.
- [174] S. Hwang, S. M. Kim, S.-M. Bak, B.-W. Cho, K. Y. Chung, J. Y. Lee, W. Chang, E. A. Stach, *ACS Appl. Mater. Interfaces* **2014**, *6*, 15140.
- [175] Y. Kojima, S. Muto, K. Tatsumi, H. Kondo, H. Oka, K. Horibuchi, Y. Ukyo, *J. Power Sources* **2011**, *196*, 7721.
- [176] T. Nonaka, C. Okuda, Y. Seno, K. Koumoto, Y. Ukyo, *Ceram. Int.* **2008**, *34*, 859.
- [177] D. Mori, H. Kobayashi, M. Shikano, H. Nitani, H. Kageyama, S. Koike, H. Sakaebe, K. Tatsumi, *J. Power Sources* **2009**, *189*, 676.
- [178] K. Kleiner, J. Melke, M. Merz, P. Jakes, P. Nagel, S. Schuppler, V. Liebau, H. Ehrenberg, *ACS Appl. Mater. Interfaces* **2015**, *7*, 19589.
- [179] S. C. Yin, Y. H. Rho, I. Swainson, L. F. Nazar, *Chem. Mater.* **2006**, *18*, 1901.
- [180] N. Yabuuchi, T. Ohzuku, *J. Power Sources* **2003**, *119*, 171.
- [181] D. Zeng, J. Cabana, J. Bréger, W.-S. Yoon, C. P. Grey, *Chem. Mater.* **2007**, *19*, 6277.
- [182] F. Lin, D. Nordlund, I. M. Markus, T.-C. Weng, H. L. Xin, M. M. Doeff, *Energy Environ. Sci.* **2014**, *7*, 3077.
- [183] F. Lin, I. M. Markus, M. M. Doeff, H. L. Xin, *Sci. Rep.* **2014**, *4*, 5694.
- [184] N. Andreu, D. Flahaut, R. Dedryvère, M. Minvielle, H. Martinez, D. Gonbeau, *ACS Appl. Mater. Interfaces* **2015**, *7*, 6629.
- [185] D. P. Abraham, T. Spila, M. M. Furczon, E. Sammann, *Electrochem. Solid-State Lett.* **2008**, *11*, A226.
- [186] E.-J. Lee, Z. Chen, H.-J. Noh, S. C. Nam, S. Kang, D. H. Kim, K. Amine, Y.-K. Sun, *Nano Lett.* **2014**, *14*, 4873.
- [187] D. Qian, B. Xu, H.-M. Cho, T. Hatsukade, K. J. Carroll, Y. S. Meng, *Chem. Mater.* **2012**, *24*, 2744.
- [188] Y. Huang, J. Chen, J. Ni, H. Zhou, X. Zhang, *J. Power Sources* **2009**, *188*, 538.
- [189] F. Wu, M. Wang, Y. Su, L. Bao, S. Chen, *Electrochim. Acta* **2009**, *54*, 6803.
- [190] L. A. Riley, S. Van Atta, A. S. Cavanagh, Y. Yan, S. M. George, P. Liu, A. C. Dillon, S.-H. Lee, *J. Power Sources* **2011**, *196*, 3317.
- [191] Y. Kim, H. Kim, S. Martin, *Electrochim. Acta* **2006**, *52*, 1316.
- [192] H.-S. Kim, *Met. Mater. Int.* **2008**, *14*, 105.
- [193] G. Ting-Kuo Fey, C.-S. Chang, T. P. Kumar, *J. Solid State Electrochem.* **2009**, *14*, 17.
- [194] Y. Huang, J. Chen, F. Cheng, W. Wan, W. Liu, H. Zhou, X. Zhang, *J. Power Sources* **2010**, *195*, 8267.
- [195] J. W. Kim, J. J. Travis, E. Y. Hu, K. W. Nam, S. C. Kim, C. S. Kang, J. H. Woo, X. Q. Yang, S. M. George, K. H. Oh, S. J. Cho, S. H. Lee, *J. Power Sources* **2014**, *254*, 190.
- [196] J. Z. Kong, C. Ren, G. A. Tai, X. Zhang, A. D. Li, D. Wu, H. Li, F. Zhou, *J. Power Sources* **2014**, *266*, 433.
- [197] T. Liu, S.-X. Zhao, K. Wang, C.-W. Nan, *Electrochim. Acta* **2012**, *85*, 605.
- [198] Z. Han, J. Yu, H. Zhan, X. Liu, Y. Zhou, *J. Power Sources* **2014**, *254*, 106.

- [199] Y. K. Sun, S. W. Cho, S. W. Lee, C. S. Yoon, K. Amine, *J. Electrochem. Soc.* **2007**, *154*, A168.
- [200] S. U. Woo, C. S. Yoon, K. Amine, I. Belharouak, Y. K. Sun, *J. Electrochem. Soc.* **2007**, *154*, A1005.
- [201] B. C. Park, H. B. Kim, S. T. Myung, K. Amine, I. Belharouak, S. M. Lee, Y. K. Sun, *J. Power Sources* **2008**, *178*, 826.
- [202] K.-S. Lee, S.-T. Myung, D.-W. Kim, Y.-K. Sun, *J. Power Sources* **2011**, *196*, 6974.
- [203] K. Yang, L.-Z. Fan, J. Guo, X. Qu, *Electrochim. Acta* **2012**, *63*, 363.
- [204] H. G. Song, S. B. Kim, Y. J. Park, *J. Electroceram.* **2012**, *29*, 163.
- [205] S. H. Yun, K.-S. Park, Y. J. Park, *J. Power Sources* **2010**, *195*, 6108.
- [206] Y. Bai, X. Wang, S. Yang, X. Zhang, X. Yang, H. Shu, Q. Wu, *J. Alloys Compd.* **2012**, *541*, 125.
- [207] J.-H. Wang, Y. Wang, Y.-Z. Guo, Z.-Y. Ren, C.-W. Liu, *J. Mater. Chem. A* **2013**, *1*, 4879.
- [208] M. L. Marcinek, J. W. Wilcox, M. M. Doeff, R. M. Kostecki, *J. Electrochem. Soc.* **2009**, *156*, A48.
- [209] B. Lin, Z. Wen, X. Wang, Y. Liu, *J. Solid State Electrochem.* **2010**, *14*, 1807.
- [210] A. M. A. Hashem, A. E. Abdel-Ghany, A. E. Eid, J. Trottier, K. Zaghbi, A. Mauger, C. M. Julien, *J. Power Sources* **2011**, *196*, 8632.
- [211] T. Mei, Y. Zhu, K. Tang, Y. Qian, *RSC Adv.* **2012**, *2*, 12886.
- [212] H.-J. Lee, Y.-J. Park, *Bull. Korean Chem. Soc.* **2010**, *31*, 3233.
- [213] H. J. Lee, K.-S. Park, Y. J. Park, *J. Power Sources* **2010**, *195*, 6122.
- [214] K. H. Jung, H.-G. Kim, K. M. Kim, Y. J. Park, *J. Appl. Electrochem.* **2011**, *41*, 551.
- [215] S. B. Kim, K. J. Lee, W. J. Choi, W. S. Kim, I. C. Jang, H. H. Lim, Y. S. Lee, *J. Solid State Electrochem.* **2009**, *14*, 919.
- [216] W. S. Kim, S. B. Kim, I. C. Jang, H. H. Lim, Y. S. Lee, *J. Alloys Compd.* **2010**, *492*, L87.
- [217] H. G. Song, J. Y. Kim, K. T. Kim, Y. J. Park, *J. Power Sources* **2011**, *196*, 6847.
- [218] Y. Huang, F.-M. Jin, F.-J. Chen, L. Chen, *J. Power Sources* **2014**, *256*, 1.
- [219] Y. Chen, Y. Zhang, B. Chen, Z. Wang, C. Lu, *J. Power Sources* **2014**, *256*, 20.
- [220] J.-Z. Kong, C. Ren, G.-A. Tai, X. Zhang, A.-D. Li, D. Wu, H. Li, F. Zhou, *J. Power Sources* **2014**, *266*, 433.
- [221] Y.-K. Sun, S.-T. Myung, C. S. Yoon, D.-W. Kim, *Electrochem. Solid State Lett.* **2009**, *12*, A163.
- [222] H. G. Song, S. B. Kim, Y. J. Park, *J. Electroceram.* **2012**, *29*, 163.
- [223] C. S. Kim, J. H. Cho, Y. J. Park, *Mater. Res. Bull.* **2014**, *58*, 49.
- [224] H.-S. Kim, Y. Kim, S.-I. Kim, S. W. Martin, *J. Power Sources* **2006**, *161*, 623.
- [225] X. Liu, H. Li, D. Li, M. Ishida, H. Zhou, *J. Power Sources* **2013**, *243*, 374.
- [226] H. Kim, M. G. Kim, H. Y. Jeong, H. Nam, J. Cho, *Nano Lett.* **2015**, *15*, 2111.
- [227] G.-H. Kim, S.-T. Myung, H.-S. Kim, Y.-K. Sun, *Electrochim. Acta* **2006**, *51*, 2447.
- [228] L. Liu, K. N. Sun, N. Q. Zhang, T. Y. Yang, *J. Solid State Electrochem.* **2009**, *13*, 1381.
- [229] T. Sasaki, V. Godbole, Y. Takeuchi, Y. Ukyo, P. Novak, *J. Electrochem. Soc.* **2011**, *158*, A1214.
- [230] D. Liu, Z. Wang, L. Chen, *Electrochim. Acta* **2006**, *51*, 4199.
- [231] F. Zhou, X. Zhao, Z. Lu, J. Jiang, J. R. Dahn, *Electrochem. Commun.* **2008**, *10*, 1168.
- [232] L. Q. Wang, L. F. Jiao, H. Yuan, J. Guo, M. Zhao, H. X. Li, Y. M. Wang, *J. Power Sources* **2006**, *162*, 1367.
- [233] H. Zhu, T. Xie, Z. Chen, L. Li, M. Xu, W. Wang, Y. Lai, J. Li, *Electrochim. Acta* **2014**, *135*, 77.
- [234] I. M. Markus, F. Lin, K. C. Kam, M. Asta, M. M. Doeff, *J. Phys. Chem. Lett.* **2014**, *5*, 3649.
- [235] Y.-S. He, L. Pei, X.-Z. Liao, Z.-F. Ma, *J. Fluorine Chem.* **2007**, *128*, 139.
- [236] L. L. W. XY, L. XF, W. XM, G. S, S. PJ, *J. Power Sources* **2006**, *160*, 657.
- [237] Y.-J. Huang, D.-S. Gao, G.-T. Lei, Z.-H. Li, G.-Y. Su, *Mater. Chem. Phys.* **2007**, *106*, 354.
- [238] H. S. Shin, D. Shin, Y. K. Sun, *Electrochim. Acta* **2006**, *52*, 1477.
- [239] Y. Ding, P. Zhang, D. Gao, *J. Alloys Compd.* **2008**, *456*, 344.
- [240] Y. Ding, P. Zhang, Y. Jiang, J. Yin, Q. Lu, D. Gao, *Mater. Res. Bull.* **2008**, *43*, 2005.
- [241] S.-H. Na, H.-S. Kim, S.-I. Moon, *Solid State Ionics* **2005**, *176*, 313.
- [242] S. HS, S. D, S. YK, *Electrochim. Acta* **2006**, *52*, 1477.
- [243] Y. Ding, P. Zhang, D. Gao, *J. Alloys Compd.* **2008**, *456*, 344.
- [244] W. Chen, J. Zhao, Y. Li, S. Li, C. Jin, C. Yang, X. Feng, J. Zhang, L. Mi, *ChemElectroChem* **2014**, *1*, 601.
- [245] M. Jo, Y.-S. Hong, J. Choo, J. Cho, *J. Electrochem. Soc.* **2009**, *156*, A430.
- [246] J. Ying, C. Jiang, C. Wan, *J. Power Sources* **2004**, *129*, 264.
- [247] S. J. Shi, J. P. Tu, Y. Y. Tang, Y. X. Yu, Y. Q. Zhang, X. L. Wang, *J. Power Sources* **2013**, *221*, 300.
- [248] F. Wu, M. Wang, Y. Su, L. Bao, S. Chen, *J. Power Sources* **2010**, *195*, 2362.
- [249] W.-H. Ryu, S.-J. Lim, W.-K. Kim, H. Kwon, *J. Power Sources* **2014**, *257*, 186.
- [250] J. Xu, S.-L. Chou, Q. Gu, H.-K. Liu, S.-X. Dou, *J. Power Sources* **2013**, *225*, 172.
- [251] Y. Chen, G. Xu, J. Li, Y. Zhang, Z. Chen, F. Kang, *Electrochim. Acta* **2013**, *87*, 686.
- [252] X. Yang, X. Wang, L. Hu, G. Zou, S. Su, Y. Bai, H. Shu, Q. Wei, B. Hu, L. Ge, D. Wang, L. Liu, *J. Power Sources* **2013**, *242*, 589.
- [253] C. Deng, S. Zhang, L. Ma, Y. H. Sun, S. Y. Yang, B. L. Fu, F. L. Liu, Q. Wu, *J. Alloys Compd.* **2011**, *509*, 1322.
- [254] Y. Cho, S. Lee, Y. Lee, T. Hong, J. Cho, *Adv. Energy Mater.* **2011**, *1*, 821.
- [255] Y.-K. Sun, Z. Chen, H.-J. Noh, D.-J. Lee, H.-G. Jung, Y. Ren, S. Wang, C. S. Yoon, S.-T. Myung, K. Amine, *Nat. Mater.* **2012**, *11*, 942.
- [256] H.-J. Noh, S.-T. Myung, Y. J. Lee, Y.-K. Sun, *Chem. Mater.* **2014**, *26*, 5973.
- [257] N. V. Kosova, E. T. Devyatkina, V. V. Kaichev, A. B. Slobodyuk, *Solid State Ionics* **2011**, *192*, 284.
- [258] Y. Li, Y. Makita, Z. Lin, S. Lin, N. Nagaoka, X. Yang, *Solid State Ionics* **2011**, *196*, 34.
- [259] G. M. Koenig, I. Belharouak, H. Deng, Y.-K. Sun, K. Amine, *Chem. Mater.* **2011**, *23*, 1954.
- [260] X. Yang, X. Wang, G. Zou, L. Hu, H. Shu, S. Yang, L. Liu, H. Hu, H. Yuan, B. Hu, Q. Wei, L. Yi, *J. Power Sources* **2013**, *232*, 338.
- [261] J.-S. Kim, C. S. Johnson, J. T. Vaughney, M. M. Thackeray, S. A. Hackney, W. Yoon, C. P. Grey, *Chem. Mater.* **2004**, *16*, 1996.
- [262] Z. Lu, L. Y. Beaulieu, R. A. Donaberger, C. L. Thomas, J. R. Dahn, *J. Electrochem. Soc.* **2002**, *149*, A778.
- [263] A. R. Armstrong, M. Holzapfel, P. Novák, C. S. Johnson, S. H. Kang, M. M. Thackeray, P. G. Bruce, *J. Am. Chem. Soc.* **2006**, *128*, 8694.
- [264] N. Tran, L. Croguennec, M. Ménétrier, F. Weill, P. Biensan, C. Jordy, C. Delmas, *Chem. Mater.* **2008**, *20*, 4815.
- [265] K. Luo, M. R. Roberts, R. Hao, N. Guerrini, D. M. Pickup, Y.-S. Liu, K. Edström, J. Guo, A. V. Chadwick, L. C. Duda, P. G. Bruce, *Nat. Chem.* **2016**, *8*, 1.
- [266] D. Seo, J. Lee, A. Urban, R. Malik, S. Kang, G. Ceder, *Nat. Chem.* **2016**, *8*, 692.
- [267] M. Sathiy, G. Rousse, K. Ramesha, C. P. Laisa, H. Vezin, M. T. Sougrati, M.-L. Doublet, D. Foix, D. Gonbeau, W. Walker, A. S. Prakash, M. Ben Hassine, L. Dupont, J.-M. Tarascon, *Nat. Mater.* **2013**, *12*, 827.

- [268] E. McCalla, A. M. Abakumov, M. Saubanère, D. Foix, E. J. Berg, G. Rousse, M.-L. Doublet, D. Gonbeau, P. Novák, G. Van Tendeloo, R. Dominko, J. M. Tarascon, *Science* **2015**, 350, 1516.
- [269] P. E. Pearce, A. J. Perez, G. Rousse, M. Saubanère, D. Batuk, D. Foix, E. McCalla, A. M. Abakumov, G. Van Tendeloo, M. L. Doublet, J. M. Tarascon, *Nat. Mater.* **2017**, 16, 580.
- [270] K. Leung, *J. Phys. Chem. C* **2013**, 117, 1539.
- [271] D. Y. Wang, J. Xia, L. Ma, K. J. Nelson, J. E. Harlow, D. J. Xiong, L. E. Downie, R. Petibon, J. C. Burns, A. Xiao, W. M. Lamanna, J. R. Dahn, *J. Electrochem. Soc.* **2014**, 161, A1818.
- [272] L. Ma, J. Xia, X. Xia, J. R. Dahn, *J. Electrochem. Soc.* **2014**, 161, A1495.
- [273] S. Tan, Y. J. Ji, Z. R. Zhang, Y. Yang, *Chemphyschem* **2014**, 15, 1956.
- [274] Y. Kato, S. Hori, T. Saito, K. Suzuki, M. Hirayama, A. Mitsui, M. Yonemura, H. Iba, R. Kanno, *Nat. Energy* **2016**, 1, 16030.
- [275] Y. Mo, S. P. Ong, G. Ceder, *Chem. Mater.* **2012**, 24, 15.
- [276] N. Kamaya, K. Homma, Y. Yamakawa, M. Hirayama, R. Kanno, M. Yonemura, T. Kamiyama, Y. Kato, S. Hama, K. Kawamoto, A. Mitsui, *Nat. Mater.* **2011**, 10, 682.
- [277] P. Novák, R. Imhof, O. Haas, *Electrochim. Acta* **1999**, 45, 351.
- [278] X. Sun, P. Bonnick, L. F. Nazar, *ACS Energy Lett.* **2016**, 1, 297.
- [279] H. Yoshida, N. Yabuuchi, S. Komaba, *Electrochem. Commun.* **2013**, 34, 60.
- [280] S. P. Ong, V. L. Chevrier, G. Hautier, A. Jain, C. Moore, S. Kim, X. Ma, G. Ceder, *Energy Environ. Sci.* **2011**, 4, 3680.
- [281] S. S. Zumdahl, S. A. Zumdahl, *Chemistry*, Brooks Cole, Belmont, CA **2014**.
- [282] J. Vinckeviciute, M. D. Radin, A. Van der Ven, *Chem. Mater.* **2016**, 28, 8640.
- [283] R. D. Shannon, *Acta Crystallogr. Sect. A: Found. Adv.* **1976**, 32, 751.
- [284] G. Crabtree, "Director's Message, 2016," can be found under <http://www.jcesr.org/directors-message-2016/> (accessed: December 2016).
- [285] J. Muldoon, C. B. Bucur, T. Gregory, *Chem. Rev.* **2014**, 114, 11683.
- [286] H. D. Yoo, I. Shterenberg, Y. Gofer, G. Gershinsky, N. Pour, D. Aurbach, *Energy Environ. Sci.* **2013**, 6, 2265.
- [287] E. Levi, M. D. Levi, O. Chasid, D. Aurbach, *J. Electroceram.* **2009**, 22, 13.
- [288] A. Emly, A. Van der Ven, *Inorg. Chem.* **2015**, 54, 4394.
- [289] M. Okoshi, Y. Yamada, A. Yamada, H. Nakai, *J. Electrochem. Soc.* **2013**, 160, A2160.
- [290] C. Vaalma, G. A. Giffin, D. Buchholz, S. Passerini, *J. Electrochem. Soc.* **2016**, 163, 1295.
- [291] A. Eftekhari, Z. Jian, X. Ji, *ACS Appl. Mater. Interfaces* **2017**, 9, 4404.
- [292] L. Geng, J. Guo, in *MRS Fall Meeting & Exhibition*, Boston, MA **2016**.
- [293] J. Rouxel, M. Danot, J. Bichon, *Bull. Soc. Chim. Fr.* **1971**, 3930.
- [294] V. M. Jansen, R. Hoppe, *Z. Anorg. Allg. Chem.* **1974**, 408, 97.
- [295] Y. Miyazaki, X. Huang, T. Kajiwara, H. Yamane, T. Kajitani, *J. Ceram. Soc. Jpn.* **2009**, 117, 42.
- [296] C. Delmas, S. Brèthes, M. Ménétrier, *J. Power Sources* **1991**, 34, 113.
- [297] C. Delmas, H. Cognac-Auradou, J. M. Cocciantelli, M. Ménétrier, J. P. Doumerc, *Solid State Ionics* **1994**, 69, 257.
- [298] A. Urban, J. Lee, G. Ceder, *Adv. Energy Mater.* **2014**, 4, 1.
- [299] S. L. Glazier, J. Li, J. Zhou, T. Bond, J. R. Dahn, *Chem. Mater.* **2015**, 27, 7751.
- [300] N. Yabuuchi, M. Takeuchi, M. Nakayama, H. Shiiba, M. Ogawa, K. Nakayama, T. Ohta, D. Endo, T. Ozaki, T. Inamasu, K. Sato, S. Komaba, *Proc. Natl. Acad. Sci. USA* **2015**, 112, 7650.
- [301] R. F. Egerton, P. Li, M. Malac, *Micron* **2004**, 35, 399.
- [302] P. Lu, P. Yan, E. Romero, E. D. Spoecker, J. Zhang, C. Wang, *Chem. Mater.* **2015**, 27, 1375.
- [303] M. Aykol, S. Kim, C. Wolverton, *J. Phys. Chem. C* **2015**, 119, 19053.
- [304] D. H. Seo, A. Urban, G. Ceder, *Phys. Rev. B: Condens. Matter Mater. Phys.* **2015**, 92, 1.
- [305] Y. Hinuma, Y. S. Meng, G. Ceder, *Phys. Rev. B* **2008**, 77, 224111.
- [306] J. Kasnatscheew, M. Evertz, B. Streipert, R. Wagner, R. Klöpsch, B. Vortmann, H. Hahn, S. Nowak, M. Amereller, A.-C. Gentschew, P. Lamp, M. Winter, *Phys. Chem. Chem. Phys.* **2016**, 18, 3956.